CONDENSATION AND PAIRING IN INHOMOGENEOUS COLD ATOMIC AND ELECTRONIC SYSTEMS

BY

KUEI SUN

DISSERTATION

Submitted in partial fulfillment of the requirements
for the degree of Doctor of Philosophy in Physics
in the Graduate College of the
University of Illinois at Urbana-Champaign, 2010

Urbana, Illinois

Doctoral Committee:

Professor Gordon A. Baym, Chair
Professor Brian L. DeMarco, Contingent Chair
Professor George D. Gollin
Professor Smitha Vishveshwara, Director of Dissertation Research

Abstract

This thesis presents a theoretical study of Bose-Einstein condensation (BEC) and Bardeen-Cooper-Schrieffer (BCS) pairing states in inhomogeneous systems of cold atoms and of electrons. Features of spatially separated phases are explored, with particular focus on the behavior of the condensed phase and its experimental measures. Three specific systems are addressed below.

First, we study bosonic atoms in three-dimensional optical lattices in the presence of an external spherical harmonic trapping potential. We investigate the critical value associated with the lattice depth and interaction strength below which the system undergoes a quantum phase transition from a global BEC phase to a coexistence of local BEC and Mott-insulating phases. We discuss the ground state properties, excitations, and experimental signatures of the condensate surrounded by the Mott-insulators.

BCS pairing in fermionic atoms of two spin species that are confined to spatially separated trapping potentials is investigated next. We investigate the one-dimensional limit and find that, with increasing separation between the spin-dependent traps, the fermions undergo a transition from a global fully-paired phase to a coexistence of a fully-paired phase, a spin-imbalanced phase with oscillatory pairing, the so-called Fulde-Ferrell-Larkin-Ovchinnikov (FFLO) state, and an unpaired completely spin-polarized phase. We present numerical profiles of key parameters of the phase diagram as well as observable signatures of the oscillatory pairing phase.

The third topic is that of transport physics in a superconductor-ferromagnetic-metal (S/F) hybrid in which superconducting phases and ferromagnetic normal phases are artificially combined. We model the interface between the S and F regions and discuss possible scattering processes at the interface. We apply the Blonder-Tinkham-Klapwijk treatment with the interfacial model to calculate resistance of the system. These results explain recent experimental observations.

To Father and Mother.

Acknowledgments

An old Chinese idiom says "be imperceptibly influenced by what you constantly see and hear." UIUC is such a great place for me to pursue my graduate study. It gave me opportunity to directly listen to, learn from, and work with an array of outstanding physicists. This thesis work represents my achievements in graduate study and research and would not have been possible without the support of many people.

I have been fortunate to have an amazing advisor, Smitha Vishveshwara, throughout my graduate life. She gave me both freedom and thoughtful choices to study various aspects of condensed matter physics to build broad and firm knowledge. Those efforts, with her guidance and encouragement, have not only resulted in further understanding of nature, but also have become exciting and rewarding projects that will be presented in this thesis. I really appreciate many instructive questions coming from her insights, which always guide me toward the solution without getting lost. Moreover, she has taught me how to communicate, share, and collaborate with others, and generously supported my participation in helpful academic activities. All she has done for me has helped develop my capability of being an independent researcher.

I would like to thank Tony Leggett and Gordon Baym. I have greatly benefitted by joining their group meetings. I have learned a lot there, from fundamental concepts to the latest advances in physics. I also thank Brian DeMarco for advice in cold atomic physics. His suggestions have kept me in the right direction doing theory by understanding experiments. Thanks to my committee members, Gordon Baym, Brian DeMarco, and George Gollin, who offered guidance and support in my preliminary exam and defense presentation. Also thanks to professors in UIUC who have taught me in class. I am grateful for the opportunity to interact with many people associated with my research. For the study on lattice bosons in Chapter 2, I thank Courtney Lannert for her collaboration. Her advice motivates me to develop more robust results. Thanks also go to Roman Barankov, Tony Leggett, Kaden Hazzard, Erich Mueller, Gordon Baym, Tzu-Chieh Wei, and Manhong Yung for helpful discussions of the theoretical aspects, and Brian DeMarco, Benjamin Lev, Hong Gao, Matthew Pasianski, Mathew White, and Mingwu Lu for helpful discussions from the experimental point of view. For the work on trapped fermions in Chapter 3, I thank Julia Meyer and Daniel Sheehy for their collaboration. Hundreds of discussions with them clarify a bunch of issues and highly strengthen the

conclusions of the work. Thanks also go to Roland Combescot, Brian DeMarco, Fabian Heidrich-Meisner, Tony Leggett, Chien-Hua Pao, Sungkit Yip, and Manhong Yung for helpful discussions. The superconductor project presented in Chapter 4 resulted from a collaboration with Nayana Shah and the experimental group of Madalina O'hara and Dale Van Harlingen. Thanks to Madalina and Dale for teaching me experimental details and providing exciting data. Thanks to all of them, especially Nayana, for physical insights that inspire me to develop a theoretical model.

Thanks to a bunch of friends in UIUC, studying and discussing physics together with me. Thanks to Manhong Yung and Ching-Kai Chiu for gathering the discussion groups, and the group members, Tzu-Chieh Wei, Zhenhua Yu, Mao-Chuang Yeh, Shu-Wei Chang, Jiansheng Wu, Weicheng Lu, Jitong Yu, and Quinlei Meng for sharing their physics with me. Thanks to Wade DeGottardi, my friend and groupmate, for kindly sharing the office with me and helping me edit my writings.

I am deeply indebted to my parents. They gave me a mind of reason and curiosity, the invaluable gift of being a scientist. I always remember that in my childhood, my father showed me the beauty of nature by holding my little hand to touch the bottom of a firefly, to shave the top of a burning candle, and to press the surface of mercury. My mother brought me the key of understanding nature - mathematics. I have never forgot the moment that with her help, I understood why one minus minus one equals two! I really appreciate their always encouraging me to pursue my own interests, always supporting me without question, and always being proud of my decision. Thanks to Chang-Fu Chen and all my good friends and relatives in Taiwan and US. Finally, thanks to Hao-Yi, for intellectual and emotional company of many years, always offering support and love.

Table of Contents

List of Symbols

A_{hf}	Hyperfine constant.
a_s	Scattering length.
$a_{1\mathrm{D}}$	Effective 1D scattering length.
$\bar{B}$	Feshbach resonance field.
B'	Magnetic field gradient.
B_0	Characteristic field of an alkali atom.
d	Separation of a spin-split trap.
d_c	Critical separation.
d_ℓ	Lattice spacing.
Δ	Superconducting energy gap.
δR	Normalized relative resistance.
E_R	Recoil energy.
f_c	Condensate fraction.
ϵ_F	Fermi energy.
g	1D coupling constant.
g_I	Nuclear g-factor.
g_J	Electronic g-factor.
$\hbar$	Planck constant.
h_{ex}	The exchange energy.
J	Tunneling energy.
k_B	Boltzmann constant.
M	Spin imbalance.
ℓ_r	Oscillator length in the transverse direction.
ℓ_z	Oscillator length in the z-direction.
μ	Chemical potential.

μ_B	Bohr magneton.
ω	Spherical harmonic trap frequency.
ω_ℓ	Effective trapping frequency of a lattice site.
ω_r	Transverse trap frequency.
ω_z	Axial trap frequency.
P	Spin polarization.
R_{ap}	Resistance of the anti-parallel configuration.
R_{p}	Resistance of the parallel configuration.
R_z	Classical radius in the z-direction.
T_c	Critical temperature.
U	Interaction energy.
U_σ	Hartree field for spin σ.
V_0	Lattice depth.
W_F	Width of a ferro-magnetic wire.
W_S	Width of a superconducting electrode.
Z	Coordination number.
Z_M	Interface parameter for major species.
Z_m	Interface parameter for minor species.

Chapter 1

Introduction

This thesis presents a theoretical study of three different many-body systems in following chapters: lattice bosonic atoms, trapped fermionic atoms, and electrons in superconducting-ferromagnetic-metal (S/F) hybrid. These studies are based on the author's graduate research on condensation and pairing physics associated with recent experiments. Although these systems correspond to different density and temperature regimes, they have two features in common: (1) an inhomogeneous spatial environment and (2) the capability of exhibiting multiple spatially separated phases with both normal and condensation or pairing phases. In the atomic systems, inhomogeneity arises from the trapping potentials and the phase separation results from energy-minimizing competitions in the trap. In the electronic system, both inhomogeneity and phase separation are imposed by justaposing two different materials. This study focuses on the physical properties and observables of the condensation and pairing phases as well as their (potential) experimental detection.

We are not only motivated by theoretical interests in condensation and pairing phases displayed in these systems, but also aim to explain their experimental signatures or to predict those that could be revealed by current probes. The investigation of condensation and pairing phases is of intrinsic theoretical interests of macroscopic quantum phenomena. Most of such realistic systems are confined in a finite, inhomogeneous geometry which can significantly alter their physical nature. Inhomogeneous systems, inherently different from their homogeneous counterparts, do not usually approach the thermodynamic limit and thus require specialized theoretical tools. Through the investigation of the three specific systems mentioned above, methods were developed applicable to a broad range of inhomogeneous condensed systems. Moreover, sensitivity of physical properties to the inhomogeneity provides a means of manipulating quantum states in experiments. Understanding the relevant properties helps us build a toolbox and constitutes toward realizing quantum simulation and quantum computation. In addition, recent experimental developments have provided effective probes of these systems; such studies have raised issues that require further theoretical investigation. For lattice bosons with coexisting phases, the layer region of the Bose-Einstein condensation (BEC) phase is predicted to be narrow and thus hard to be effectively detected. For population-imbalanced Fermi systems with coexisting phases, the Fulde-Ferrell-Larkin-Ovchinnikov (FFLO) phase with oscillatory

pairing has not been directly seen. Two experimental studies of the hybrid system of superconducting electrodes (S) and ferro-magnetic metal (F) wires, two experimental groups have yielded opposite trends in the relative resistance between parallel and anti-parallel alignments of magnetization of the F wires. In this thesis, we discuss a plausible way for detecting narrow BEC regions of the lattice bosons, suggest experimental signatures for elusive FFLO phases in the separately trapped fermions and propose a theoretical model that explains the conflicting data in the S/F hybrid experiments.

This thesis is organized as follows. In Chapter 2, we study the BEC and the coexistence of phases in bosonic atoms in deep optical lattices. First we briefly review the background in several aspects, including a theory of condensation in dilute bosonic gases and their properties that share similarities with BECs in lattices, the experimental realization of optical lattices, as well as a theoretical treatment of such lattice system, known as the Bose-Hubbard model. The well-known mean-field solutions predict a phase transition between the Mott-insulating phase and the BEC phase as a function of lattice parameters as well as the coexistence of both phases due to the inhomogeneous trapping potential. We then turn to our main contributions: the deep lattice regime. We introduce a known pseudo-spin model and our proposed fixed-number model to calculate the condensate properties in the deep lattice regime. We demonstrate the consistency of these results and compare them to those in a continuum system. We suggest two experimental signatures that can confirm the existence of the BEC phase in a coexisting system: one is a multi-peak structure in the radio frequency spectrum and the other a relatively high interference peak in the time-of-flight expansion. Our studies are also presented in Ref. [1].

In Chapter 3, we study BCS pairing between two hyperfine species of fermionic atoms confined to spatially separated trapping potentials (which we call a spin-split trap). We focus on the one-dimensional system, discussing possible realizations of this system in cold atomic experiments by applying a magnetic field gradient or other means. We use various analyses, such as Bethe ansatz, the local density approximation, and the Cooper problem to argue that such a system can exhibit coexistence of three phases: a fully-paired superfluid phase, a fully-polarized normal phase, and a spin-imbalanced superfluid phase with oscillatory pairing, known as the FFLO state. We present numerical methods and results based on the Bogoliubov-de Gennes treatment to identify these three phases and delineate the phase diagram. Moreover, we discuss the observable signatures for the FFLO state, exhibited in the measurement of the local density of states and pair momentum distribution function. This work is also presented in Ref. [2].

In Chapter 4, we switch gears and discuss the physics of electronic transport in the S/F hybrid system. In order to explain the conflicting resistance measurement, we modify the Blonder-Tinkham-Klapwijk model to incorporate a spin-dependent S/F interface parameter. We compute from this modified model the amplitudes

of various quantum scattering processes responsible for current flow through the system, including the normal and Andreev reflections as well as the quasi-particle and quasi-hole transmissions. The resistance obtained shows dependences on the magnetization of the F wires, the superconducting gap of the S electrode, the proposed interface properties, the geometry of the system, and temperature. We specify the parameter regimes that distinguish the trend of relative resistance between the systems having two F wires with parallel and anti-parallel magnetization. Finally we illustrate the numerical results, which well describe the experimental measurements.

We begin by briefly reviewing basic condensation and pairing physics, following the author's learning path. At the atomic scale, physics is qualitatively different from that of the the classical world. The motion of electrons and atoms is well-described by quantum mechanics. Particles in the quantum mechanical regime exhibit wave-like behavior such as superposition and interference. The de Broglie equation relates the momentum p of a particle and the wavelength λ of the associated wave through the equation

$$\lambda = h/p, \tag{1.1}$$

where h is the Planck's constant. For a many-body system, the quantum mechanical effects dominate in a low temperature regime in which a particle see the wave-like behavior of the other particles. This condition is $\lambda \sim \ell$, where ℓ is the average inter-particle spacing. The wavelength is related to the momentum due to the thermal motion, while ℓ can be expressed in terms of the particle density n. In three dimensional space, we obtain

$$k_B T \sim \frac{h^2 n^{2/3}}{m}. \tag{1.2}$$

In addition, the quantum behavior of a many-body system is governed not only by quantum mechanics, but also by quantum statistics. A system of N identical particles obeys Bose or Fermi statistics, which are characterized by the symmetry of anti-symmetry of the wave function under the exchange of two particles. In symbols,

$$\Psi(\mathbf{r}_1\sigma_1, \cdots, \mathbf{r}_i\sigma_i, \cdots, \mathbf{r}_j\sigma_j, \cdots, \mathbf{r}_N\sigma_N) = \pm\Psi(\mathbf{r}_1\sigma_1, \cdots, \mathbf{r}_j\sigma_j, \cdots, \mathbf{r}_i\sigma_i, \cdots, \mathbf{r}_N\sigma_N). \tag{1.3}$$

Here $\mathbf{r}_i$ and σ_i are the spatial and spin degrees of freedom of the ith particle, respectively. The $\pm$ sign corresponds to the system of Bose (Fermi) statistics, with the particles in the system called bosons (fermions).

Bose-Einstein condensation is a quantum state of a bosonic system that has a macroscopic number of

particles occupying a single one-particle state. Eighty five years ago Einstein predicted that in a system of non-interacting massive bosons, the lowest-energy one-particle state is macroscopically occupied below a critical temperature [3]. In an interacting system, a BEC is still expected below a finite critical temperature [4]. For example, superfluid liquid ^{4}He, discovered more than seventy years ago, is a BEC with strong interactions between atoms.

In a system of fermions, macroscopic occupation can not occur because the Pauli exclusion principle prohibits more than one fermion occupying the same state. However, if two fermions can form a pair such that the wavefunction of the system is well represented by the pair's degrees of freedom, exchange of pairs can be regarded as two exchanges of fermions, which thus generates the minus sign of Eq. (1.3) twice. Therefore such pairs behave as bosons. The system can have a condensed phase with a macroscopic occupation of a one-pair state. If the size of a pair is small compared to the inter-particle spacing, two fermions of a pair tightly bound and can be considered as a diatomic molecule in which a fermion is only affected by its pairing partner. In such cases, Fermi statistics does not play a role and the "molecular" condensed phase has similar properties to a BEC of bosonic particles. In the regime in which the size of a pair is large compared to the inter-particle spacing, such as superconducting electrons in a classical superconductor, the effects of Fermi statistics can no longer be ignored. Such a condensed pairing state is treated by the Bardeen-Cooper-Schrieffer (BCS) theory that successfully describes classical superconductivity [5].

The above discussions provide a general overview of the basic physics. Let us stand upon the shoulders of giants and move to specific studies of cold atomic and superconducting systems.

Chapter 2

Condensation of bosonic atoms in optical lattices

We begin our study of condensation with the case of bosonic atoms in an optical lattice. We review the basic physics of a generic BEC of trapped dilute gases as well the technology used to create optical lattice potentials. We then turn to the Bose-Hubbard model, which well describes the many-body behavior of lattice bosons. The uniform Bose-Hubbard system exhibits a quantum phase transition between a BEC and a Mott-insulator, while the inhomogeneous case can exhibit coexistence of BEC and Mott-insulating phases. Our study focuses on BEC in the deep lattice regime. We provide a comprehensive characterization of the BEC state in a homogeneous system as well as in the coexisting case and propose settings and measurements which would pinpoint direct experimental signatures of the presence of the condensate. Below we give a general overview of this study.

Status review

In the 1990s, improvements in the techniques of trapping and cooling atoms made BEC and condensed pairing states realizable in dilute atomic gases [6, 7, 8, 9], opening a new window to quantum many-body phenomena. Following early striking discoveries, focus was turned to laser-generated lattice systems in which a periodic potential is created through electric dipole coupling between atoms and a standing laser wave. Optical lattice systems provide a highly controllable environment in which the tunneling and interaction energy can be precisely tuned within a large range, thus allowing extensive studies of quantum phases of condensed matter systems [10, 11, 12]. Such controllable lattice sites are also good candidates for realizing quantum qubits in quantum computing realization [13]. In the case of bosons in optical lattices, when the tunneling energy divided by the interaction energy decreases below a critical value, the system undergoes a transition from the BEC phase to the Mott-insulating phase [14], which is characterized by zero compressibility and zero condensate fraction. This transition is detectable through various methods such as matter wave interference [15], Bragg spectroscopy [16], and radio-frequency (RF) spectroscopy [17] and has been experimentally observed in one dimensional [18], two dimensional [19], and, our focus in this thesis, three dimensional optical lattices [20]. In addition, recent experimental developments allow direct high resolution imaging number density profiles of the system. These techniques can resolve individual sites as well as single

atoms [21, 22, 23, 24, 25] and thus determine number distribution as well as associated number fluctuation; these are key signatures of BEC that follow from our calculations presented in the following sections. Therefore, physical properties such as compressibility, condensate fraction, and long range coherence, (which are a function of density and fluctuations), can be directly measured to verify our theoretical conclusions.

In realistic 3D systems, a confining trap renders the boson density non-uniform. Below a critical temperature (which is now a function of the lattice depth, the trap frequency, and total number of particles [26]), the whole system is a BEC in a weak lattice potential, while in a sufficiently deep optical lattice this inhomogeneous system is predicted to have a BEC or Mott-insulating core surrounded by a multiple-layer structure in which Mott-insulating layers with different occupation number are separated by relatively thin condensate layers [27, 28, 29]. The study of such inter-layer structures is of interest as a model realization of spatially coexisting quantum phases separated by critical crossover regimes. A pure BEC in the deep lattice regime is of intrinsic interest; its ground-state properties and excitation spectrum have been studied in various ways [30, 31, 32, 33, 34, 35, 36, 37] and show vast differences from more commonly encountered condensates in free space or in the strong-tunneling limit (shallow optical lattices). Recent experiments using hyperfine transitions driven by an external RF field have conclusively shown the existence [38, 39] and formation [40] of a Mott-insulating shell structure in systems in which the condensate inter-layers are predicted to be much thinner than the Mott-insulating shells. Theoretical studies have also discussed signatures of the BEC layers between the Mott-insulator layers in the RF spectrum [41] and matter-wave interferences [42] of the system. Currently, however, the existence or properties of the narrow condensates are as yet to be unequivocally verified in experiments. Based on this work, our study follows a systematic way to explore the properties of such a BEC state. Our main contributions are (1) to propose a ground state of the BEC that conserves particle number and displays quantum entanglement (while the extensively used mean-field state does not) and (2) to propose two measurable signatures that would verify the existence of the thin BEC layers, both of which will be presented in the following sections.

These studies address two key questions: (1) how do we understand a realistic system beyond the mean-field method with the local density approximation (LDA) and (2) how well do the experimental measures reveal the physical nature of the system? For question (1), more precise methods incorporating quantum fluctuation and inhomogeneity such as quantum Monte Carlo and density matrix renormalization group have been performed as a comparison with the mean-field plus LDA [43, 44, 45]. Regimes in which the mean-field plus LDA is qualitatively incorrect have also been identified [44, 46, 47, 48, 49]. For question (2), other studies have focused on the matter wave interference experiments. They have addressed how realistic effects such as quantum and thermal fluctuations, interactions, finite size, and short time duration

alter the interference pattern from an ideal model [50, 51, 52, 53]. Many studies have challenged the interference peaks as evidence of the BEC state and found that a normal system ($T > T_c$) can also display such peaks [54, 55, 56, 57]. In addition, studies on experimental processes have found that the BEC state in deep lattices would be heated and destroyed during the preparation process in experiments, but that may nevertheless be preserved [58, 59, 60]. In this chapter, we will discuss these open issues and how they are related to our study.

Organization

This chapter is organized as follows. The first two sections are preparations for investigating the lattice boson system. In Section 2.1, we briefly review the physics of BEC and its mathematically definition, as well as physical behaviors of a condensate in a continuum system of dilute gases. We derive the equation for the ground state wave function of the condensate and study the elementary excitations of a BEC.

In Section 2.2, we discuss means of realizing optical lattice in cold atomic experiments. We model the physics of bosonic atoms in such optical lattices with a microscopic many-body Hamiltonian, the Bose-Hubbard Hamiltonian, which describes particle tunneling and the interactions between particles. The correspondence between the lattice parameters and the Bose-Hubbard parameters are also presented.

In Section 2.3, we study the phenomenon of the condensate-Mott-insulator transition by solving the Bose-Hubbard model in the uniform case in a mean-field approach. We plot the phase diagram as a function of the chemical potential and the tunneling energy relative to the interaction. The condensate properties such as number density, number fluctuations, condensate fraction, and compressibility are expressed in terms of the mean-field variable. The local density approximation (LDA) analysis is performed for the inhomogeneous lattice, in which we show that a spherically trapped system has a concentric shell structure with the Mott-insulator shells and the condensate shells appearing alternatively. This wedding-cake-like density profile is illustrated.

Sections 2.1- 2.3 are based on previous work. In Section 2.4, we present our main work about the physics in the deep-lattice regime, in which the ratio of the tunneling energy to the interaction energy is small compared to one. Ignoring this small quantity allows us to truncate the Hamiltonian matrix and map the Bose-Hubbard Hamiltonian into a quantum spin Hamiltonian. Following the mean-field treatment, we write down the condensate properties as a function of the azimuthal angle of the pseudo-spin. We study elementary excitations of a uniform BEC and collective motions of a BEC shell in the inhomogeneous system by studying the excitation of the corresponding pseudo-spin system. We find a high degree of similarity between excitations in the BEC in lattice bosons and those in the dilute gases. Considering that the number-conserving property of the Bose-Hubbard Hamiltonian is broken in the mean-field description,

we describe the condensate ground state with a fixed-number wave function which displays entanglement and off-diagonal long-range order and conserves the total number of particles as any exact eigenstate of the Bose-Hubbard Hamiltonian should do. We compare this fixed-number entangled wave function with a commonly-used mean-field wave function. By calculating the condensate properties in each description, we identify the conditions under which the mean-field approximation is valid. These studies shed light on the range of validity of mean-field descriptions of the condensate in the deep-lattice regime.

In Section 2.5, we propose a specific set of parameters for an RF experiment in which the system is prepared and resolved as in Ref. [38]. We find that the presence of the condensate interlayer can lead to a two peak structure, in contrast to a single peak structure associated with each adjoining Mott-insulator phase. We discuss how this RF spectrum profile ought to be robust against Goldstone-mode perturbations associated with spontaneous symmetry breaking in the condensate and against low-temperature effects and would be sensitive to the destruction of condensate order. This sensitivity to condensate order should allow experiments to distinguish whether the incommensurate-density layers between Mott-insulator shells are in the BEC or normal fluid phase. Another commonly used probe which has provided a wealth of valuable information on the Mott-insulator-BEC transition is matter wave interference [20].

In Section 2.6, we analyze the matter-wave interference for the specific case of the interlayer setting. We make transparent the contribution of various terms in the fixed-number entangled wave function to interference patterns that do not occur in the Mott-insulator state. While distinguishing the condensate from the Mott-insulator phases through interference experiments can be a challenging task, our analysis provides methods to do so.

Finally, in Section 2.7, we discuss several issues between theoretical models and experimental measurements and propose several aspects for further study on the Bose-Hubbard system.

2.1 Bose-Einstein condensation in dilute gases

Before we present the study on BECs in optical lattice system, let us briefly give a warm-up review on the physics of BEC and its behaviors in dilute gases. Although we deal with the continuum system in this section, the treatment works well for the BEC in the lattice system. Later we will show the similarity between the two systems.

This Section is organized as follows. In Subsection 2.1.1, a mathematical definition of BEC suggested by Penrose and Onsager [61] is discussed. The definition provides a systematic way to compute the condensate fraction and identify the macroscopically occupied one-particle state by diagonalizing the one-particle density

matrix of the system in the thermodynamic limit. In the following sections, we use this treatment to obtain the condensate properties in optical lattices.

In Subsection 2.1.2, we consider a BEC of trapped dilute gases at zero temperature and show derivation of the ground state wave function of the condensate. When the kinetic energy is less competitive with the interaction and potential energies (that is the case in experiments), the wave function has a simple form in ThomaS/Fermi approximation. In Subsection 2.1.3, we study the elementary excitations of a BEC in two aspects: the microscopic model and the hydrodynamic model. In the microscopic model, we obtain the spectrum by diagonalizing the microscopic Hamiltonian with a Bogoliubov transformation. An analytic form of the spectrum of a uniform system is given and discussed. In the hydrodynamic model, we consider equations of motion of macroscopic quantities, such as number density and current, and discuss the collective motions of them. Finally we obtain a differential equation that yields the spectrum of collective excitations in an inhomogeneous system.

This section provides concepts and techniques that are used to study the optical lattice systems in the following sections. More details about BEC in dilute gases can be found in Ref. [62, 63].

2.1.1 Definition of BEC

In this section we give a mathematical description for Bose-Einstein condensation associated with the one-particle density matrix of the system. We derive the condensate fraction, the key quantity of a BEC, as a function of the elements of the one-particle density matrix.

BEC is a low-temperature phenomenon in a bosonic many-body system which has a macroscopic number of particles occupying a single one-particle state. Such macroscopic occupations imply many particles share the same one-particle wave function. Given a simple picture in which wave functions of particles are represented by Gaussian wave packets with width of the de Broglie thermal wave length $\sqrt{2\pi\hbar^2/mk_BT}$, when the temperature goes down, the wave packets broaden, overlap, and become indistinguishable, and hence the condensate appears. The critical temperature T_c is estimated by equating the thermal wave length and the inter-particle spacing $n^{1/3}$ (n is the number density),

$$T_c = C\frac{\hbar^2 n^{2/3}}{mk_B}, \tag{2.1}$$

up to a numerical factor C. For a uniform ideal gas, $C = 3.31$. Eq. (2.1) well estimates $T_c = 3.13$ K for liquid ^{4}He, compared to the real value 2.17 K.

A generalized definition of BEC is suggested by Penrose and Onsager [61]. Considering a many-body

wave function of a system with N identical bosons, $\Psi_B(\mathbf{r}_1, \mathbf{r}_2, \cdots, \mathbf{r}_N)$, the single-particle density matrix $\hat{\rho}$ with elements defined in spatial basis can be written as

$$\langle \mathbf{r} | \, \hat{\rho} \, | \mathbf{r}' \rangle \equiv \int d\mathbf{r}_2 \cdots d\mathbf{r}_N \Psi_B^*(\mathbf{r}, \mathbf{r}_2, \cdots, \mathbf{r}_N) \Psi_B(\mathbf{r}', \mathbf{r}_2, \cdots, \mathbf{r}_N) = \left\langle \hat{\psi}^\dagger(\mathbf{r}) \hat{\psi}(\mathbf{r}') \right\rangle, \tag{2.2}$$

where $\hat{\psi}^\dagger$ ($\hat{\psi}$) are bosonic creation (annihilation) operators. From Eq. (2.2) $\hat{\rho}$ is Hermitian and hence has real eigenvalues. Given N_0 the maximum eigenvalue of $\hat{\rho}$ and the condensate fraction $f_c \equiv N_0/N$, the definition of BEC is $f_c \sim \mathcal{O}(1)$ in the thermodynamic limit. If $f_c \sim 0$, we say the system is in the normal phase. The eigenstate which corresponds to the eigenvalue N_0 is the macroscopically occupied one-particle state. If the system has translational invariance, the condensate fraction is expressed by the elements of the density matrix as

$$f_c = \lim_{|\mathbf{r}-\mathbf{r}'| \to \infty} \frac{\langle \hat{\psi}^\dagger(\mathbf{r}) \hat{\psi}(\mathbf{r}') \rangle}{\langle \hat{\psi}^\dagger(\mathbf{r}) \hat{\psi}(\mathbf{r}) \rangle}. \tag{2.3}$$

2.1.2 Ground state of trapped bosons

In this subsection, we write down the Hamiltonian of bosons in a trap. We apply the Hartree approximation and get a differential equation, the Gross-Pitaevskii (GP) equation [64, 65], for the ground state wave function by a variational method. The approximate solution is obtained by the ThomaS/Fermi approximation.

The Hamiltonian of a 3D trapped Bose gas with point-contact interaction is given by

$$H = \int d^3 r \hat{\psi}^\dagger(\mathbf{r}) [-\frac{\hbar^2}{2m} \nabla^2 + V(\mathbf{r}) - \mu] \hat{\psi}(\mathbf{r}) + \frac{U_0}{2} \hat{\psi}^\dagger(\mathbf{r}) \hat{\psi}^\dagger(\mathbf{r}) \hat{\psi}(\mathbf{r}) \hat{\psi}(\mathbf{r}), \tag{2.4}$$

where V is the trapping potential, μ the chemical potential , and $U_0 = 4\pi\hbar^2 a_s/m$ the interaction strength [63, 62]. In the dilute limit $n a_s^3 \ll 1$, the ground state energy is obtained by applying the Hartree approximation $\hat{\psi} = \psi_0$ into Eq.(2.4),

$$E_0 \quad = \quad \int d^3 r \frac{\hbar^2}{2m} |\nabla \psi_0(\mathbf{r})|^2 + [V(\mathbf{r}) - \mu] |\psi_0(\mathbf{r})|^2 + \frac{U_0}{2} |\psi_0(\mathbf{r})|^4 \tag{2.5}$$

ψ_0 is interpreted as the wave function of the condensate. The particle density is given by $n(\mathbf{r}) = |\psi_0(\mathbf{r})|^2$ with a constraint $\int d^3 r n(\mathbf{r}) = N$. The variation of $\delta E_0/\delta\psi_0 = 0$ yields the GP equation for the ground state wave function,

$$\left[-\frac{\hbar^2}{2m} \nabla^2 + V(\mathbf{r}) - \mu + U_0 |\psi_0|^2 \right] \psi_0 = 0. \tag{2.6}$$

If the trap is a harmonic-like potential with trapping frequency ω, in the ThomaS/Fermi limit $Na_s/a_{\rm osc} \gg 1$, where $a_{\rm osc} = \sqrt{\hbar/m\omega}$ is the oscillator length, the ratio of the kinetic energy to the total energy is of order $(Na_{\rm s}/a_{\rm osc})^{-4/5}$) and hence the kinetic energy is negligible. In this approximation, the solution of the GP equation is

$$n_0(\mathbf{r}) = |\psi_0(\mathbf{r})|^2 = \frac{\mu - V(\mathbf{r})}{U_0} \tag{2.7}$$

2.1.3 Elementary excitations

In this subsection, we discuss elementary excitations of homogeneous and inhomogeneous BECs. We discuss two models, a microscopic model and a hydrodynamic model, any of which can be chosen to obtain the excitation spectrum for convenience. We use the microscopic model to obtain an analytic spectrum of a uniform system which exhibits wave-like behavior in the low energy limit and particle-like behavior in the high energy limit. We use the hydrodynamic model for elementary excitations in an inhomogeneous system, which describes collective motions in particle density and current.

We begin with the microscopic model, considering small quantum fluctuations on the ground state wave function,

$$\hat{\psi}(\mathbf{r}) = \psi_0(\mathbf{r}) + \delta\hat{\psi}(\mathbf{r}) \tag{2.8}$$

into Eq.(2.4),

$$\begin{aligned} H &= \int d^3r(\psi_0^* + \delta\hat{\psi}^\dagger)[-\frac{\hbar^2}{2m}\nabla^2 + V(\mathbf{r}) - \mu](\psi_0 + \delta\hat{\psi}) + \frac{U_0}{2}(\psi_0^* + \delta\hat{\psi}^\dagger)^2(\psi_0 + \delta\hat{\psi})^2 \\ &= E_0 + \int d^3r - \frac{\hbar^2}{2m}\delta\hat{\psi}^\dagger\nabla^2\delta\hat{\psi} + \frac{U_0}{2}[{\psi_0^*}^2\delta\hat{\psi}^2 + {\psi_0}^2\delta\hat{\psi}^{\dagger 2}] + [V(\mathbf{r}) - \mu + 2U_0|\psi_0|^2]\delta\hat{\psi}^\dagger\delta\hat{\psi} + O(\delta\hat{\psi}^3) \\ &= E_0 + \int d^3r - \frac{\hbar^2}{2m}\delta\hat{\psi}^\dagger\nabla^2\delta\hat{\psi} + \frac{\tilde{U}(\mathbf{r})}{2}[\delta\hat{\psi}^2 + \delta\hat{\psi}^{\dagger 2}] + [2\tilde{U}(\mathbf{r}) - \tilde{\mu}(\mathbf{r})]\delta\hat{\psi}^\dagger\delta\hat{\psi}. \end{aligned} \tag{2.9}$$

In the last line we assume ψ_0 real without loss of generality and define the Hartree potential $\tilde{U}(\mathbf{r}) \equiv U_0 n_0(\mathbf{r}) = U_0\psi_0^2$ and the local chemical potential $\tilde{\mu}(\mathbf{r}) \equiv \mu - V(\mathbf{r})$. Eq. (2.9) is diagonalized in a quasi-particle basis as

$$H = E_0 + \sum_n \epsilon_n \alpha_n^\dagger \alpha_n, \tag{2.10}$$

by a Bogoliubov transformation

$$\begin{aligned} \delta\hat{\psi}(\mathbf{r}) &= \sum_n u_n(\mathbf{r})\alpha_n - v_n^*(\mathbf{r})\alpha_n^\dagger \\ \delta\hat{\psi}^\dagger(\mathbf{r}) &= \sum_n u_n^*(\mathbf{r})\alpha_n^\dagger - v_n(\mathbf{r})\alpha_n, \end{aligned} \tag{2.11}$$

where the quasi-particle energy and wave functions satisfy the equation

$$\sigma_z \begin{pmatrix} -\frac{\hbar^2}{2m}\nabla^2 + 2\tilde{U} - \tilde{\mu} & \tilde{U} \\ \tilde{U} & -\frac{\hbar^2}{2m}\nabla^2 + 2\tilde{U} - \tilde{\mu} \end{pmatrix} \begin{pmatrix} u_n \\ -v_n \end{pmatrix} = \epsilon_n \begin{pmatrix} u_n \\ -v_n \end{pmatrix}, \tag{2.12}$$

where σ_z is the z-component Pauli matrix. The wave functions have the properties

$$\begin{aligned} &\int d^3r[u_m(\mathbf{r})u_n^*(\mathbf{r}) - v_m^*(\mathbf{r})v_n(\mathbf{r})] = \delta_{mn} \\ &\sum_n [|u_n(\mathbf{r})|^2 - |v_n(\mathbf{r}')|^2] = \delta(\mathbf{r}-\mathbf{r}') \end{aligned} \tag{2.13}$$

In an uniform system ($V = 0$), the translational invariance implies that ψ_0 and n_0 are spatially independent, and we have $\mu = U_0 n_0$ from Eq. (2.6). The quasi-particles are labeled by momentum coordinate. Therefore, Eq. (2.12) becomes

$$\begin{aligned} (\frac{p^2}{2m} + U_0 n_0 - \epsilon_p)u_p - U_0 n_0 v_p &= 0 \\ -U_0 n_0 v_p + (\frac{p^2}{2m} + U_0 n_0 + \epsilon_p)u_p &= 0. \end{aligned} \tag{2.14}$$

The condition for non-trivial solution of Eq. (2.14) yields the spectrum

$$\epsilon_p = \sqrt{2U_0 n_0 \epsilon_p^0 + (\epsilon_p^0)^2}, \tag{2.15}$$

where $\epsilon_p^0 = p/2m$ is the spectrum of a free particle. In the high energy regime ($\epsilon_p^0 \gg 2U_0 n_0$), the excitation behaves like a free particle, while in the low energy regime ($\epsilon_p^0 \ll 2U_0 n_0$), it behaves like a sound wave with the sound velocity $\sqrt{U_0 n_0/m}$.

In a trapped system, a useful approach to explore the elementary excitations is to consider the dynamics of density and velocity of the condensate, which is defined as

$$\mathbf{v} \equiv \frac{\hbar^2}{2mi}\frac{(\psi^*\nabla\psi - \psi\nabla\psi^2)}{|\psi|^2} = \frac{\hbar}{m}\nabla\phi, \tag{2.16}$$

where ϕ is the phase of the wave function.

To find the dynamics, we treat Eq. (2.6) as a non-linear Schrödinger equation with the chemical potential replacing the eigen energy and write down the time-dependent GP equation

$$\left[-\frac{\hbar^2}{2m}\nabla^2 + V(\mathbf{r}) - \mu + U_0|\psi|^2\right]\psi = i\hbar\frac{\partial\psi}{\partial t}. \tag{2.17}$$

Substituting $\psi = \sqrt{n}e^{i\phi}$ into Eq. (2.17) and applying the relation of Eq. (2.16), we obtain the equation of motion of n and $\mathbf{v}$,

$$\frac{\partial n}{\partial t} = -\frac{\hbar}{m}\nabla\cdot(n\mathbf{v}) \tag{2.18}$$

$$m\frac{\partial \mathbf{v}}{\partial t} = -\nabla(-\frac{\hbar^2}{2m\sqrt{n}}\nabla^2\sqrt{n} + V + U_0 n + \frac{1}{2}mv^2). \tag{2.19}$$

Eq. (2.18) is a continuity equation and Eq. (2.19) is analogous to the Euler equation for the non-rotational fluid. Now we consider a small oscillation of density from equilibrium, $n = n_0 + \delta n e^{i\omega t}$, apply the ThomaS/Fermi approximation (ignore the kinetic energy effect), cancel the velocity term in Eq. (2.18) and (2.19), and finally write down an equation for the collective modes

$$\omega^2\delta n = -\frac{U_0}{m}\nabla\cdot(n_0\nabla\delta n). \tag{2.20}$$

Eq. (2.20) is an eigenvalue problem, yielding a set of oscillation frequencies. If the n_0 has spherical symmetry, we can let $\delta n(\mathbf{r}) = \delta n(r)Y_{lm}(\theta,\phi)$, where $Y_l^m(\theta,\phi)$ is the spherical harmonics. And the eigen equation becomes

$$\frac{m\omega^2}{U_0}\delta n = -(\partial_r n_0)(\partial_r\delta n) - n_0[\partial_r^2\delta n + \frac{2}{r}\partial_r\delta n - \frac{l(l+1)}{r^2}\delta n]. \tag{2.21}$$

For a spherical harmonic trap, $V(\mathbf{r}) = m\omega^2 r^2/2$, Eq. (2.20) with the equilibrium density profile n_0 obtained from Eq. (2.7) yields the spectrum $\omega^2 = \omega_0^2(l + 3n + 2nl + 2n^2)$ [66]. The low excitation modes have been observed in experiments [67, 68] and confirmed by various theoretical approaches [69, 70, 71]. We see that in Eq. (2.20), the equilibrium density profile (or the geometry) of the condensate, n_0, is the only effect on the spectrum of excitations. The statement is also valid for the condensate in optical lattices, even if the condensate properties quite differ in the lattice system. We will discuss it in the following sections.

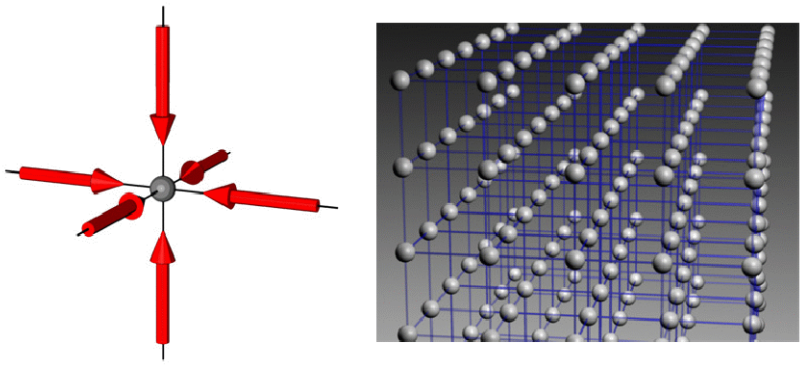

Figure 2.1: (Reproduced from Ref. [12]) Left: six laser beams form a three dimensional optical lattice. Right: spatial distribution of lattice sites.

2.2 Optical lattices

We have discussed the properties of a general BEC in the last section. To fulfill the preparation for studying the condensation in lattice bosons, we turn to another fundamental part of the system, the optical lattice. In this section, we discuss the physics of the optical lattice potential and relevant lattice parameters by considering the interaction between atoms and imposed lasers. We model the behavior of bosonic particles in such a lattice system associated with the Wannier wave functions and lattice parameters. Finally, we present the Bose-Hubbard Hamiltonian, which is used as a basic Hamiltonian describing all physical phenomena in the rest of this chapter.

Consider an atom with the ground state $|g\rangle$ and an excited state $|e\rangle$ placed in an oscillatory electric field $\mathbf{E}(\mathbf{r})\exp(i\omega t)$. The transition in electronic states between $|g\rangle$ and $|e\rangle$ may induce electric dipole moment of the atom, which is coupled to the external field; this effect is called AC-Stark effect. In a semi-classical picture, if ω is far away from the transition frequency, ω_0, the AC-Stark effect leads to an effective potential given by

$$V(\mathbf{r}) = \frac{|\mathbf{E}(\mathbf{r})\langle e|\hat{\mu}|g\rangle|^2}{\omega - \omega_0}, \tag{2.22}$$

where $\hat{\mu}$ is the dipole operator.

To generate an optical lattice potential, we consider two identical laser beams (with the same intensity and wave length λ) prorogating in opposite directions to form a sinusoidal standing wave. From Eq. (2.22), the potential is periodic and of the form

$$V(x) = V_0 \cos^2 kx, , \tag{2.23}$$

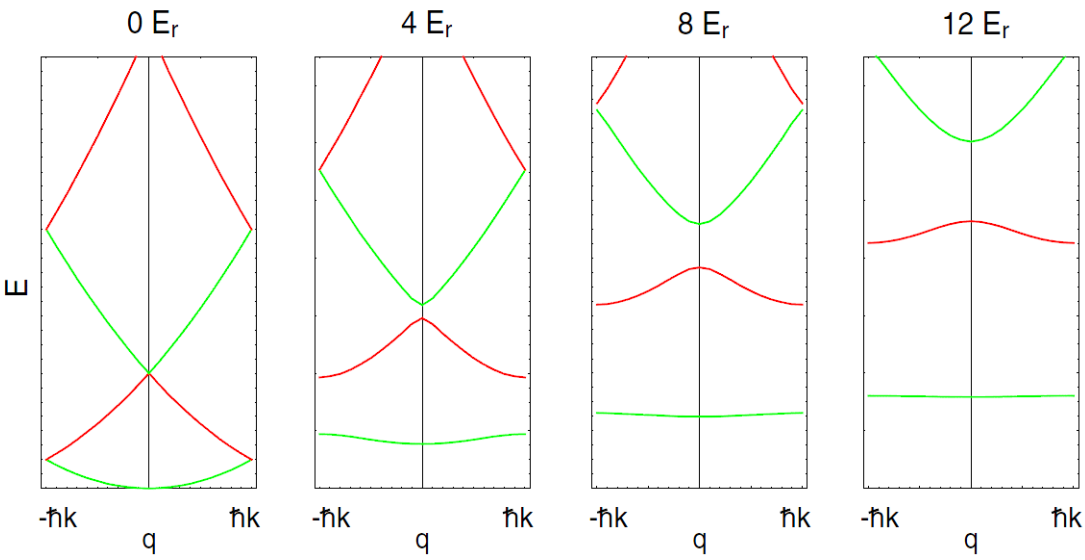

Figure 2.2: (Reproduced from [10]) The spectrum of the first Brillouin zone in a 3D optical lattice with the lattice depth being 0, 4, 8, and 12 recoil energy from the left to right panels.

where the magnitude V_0 is proportional to the intensity and $k = 2\pi/\lambda$ is the wave vector. Potentials in higher dimensions are generated by creating more standing waves in different directions, as shown in Figure 2.1 for the 3D case. The actual 3D lattice potential that we consider in the following sections looks like

$$V_\ell(\mathbf{r}) = V_0(\cos^2 kx + \cos^2 ky + \cos^2 kz) + \frac{1}{2}m\omega^2 r^2. \tag{2.24}$$

The last term of Eq. (2.24) is the external spherical harmonic confinement, assumed to slowly vary over the length scale comparable to the lattice spacing $d_\ell = \lambda/2$. The potential at one lattice site is approximated by a harmonic potential with trapping frequency

$$\omega_\ell = \sqrt{\frac{V_0}{2E_R}} \times \frac{\hbar k^2}{m}, \tag{2.25}$$

where $E_R \equiv \hbar^2 k^2/2m$ is the recoil energy, a typical energy scale in the optical lattice system. The condition for a deep lattice is given by $V_0/\hbar\omega_\ell \gg 1$, or equivalently, $V_0/E_R \gg 1$.

If the external confinement vanishes ($\omega = 0$), the lattice becomes uniform and possesses translational invariance. Figure 2.2 shows the energy spectrum of the Bloch state vs quasi-momentum in the first Brillouin zone in uniform lattices with depth $V_0 = 0$, 4, 8, and $12E_R$. The first band gap increases with increase in the lattice depth, and approaches to $\hbar\omega_\ell$ in deep lattices. Figure 2.3 shows the Wannier wave function in the first energy band with the lattice depth $V_0 = 3$ and $10E_R$. We see that in deep optical lattices, the Wannier

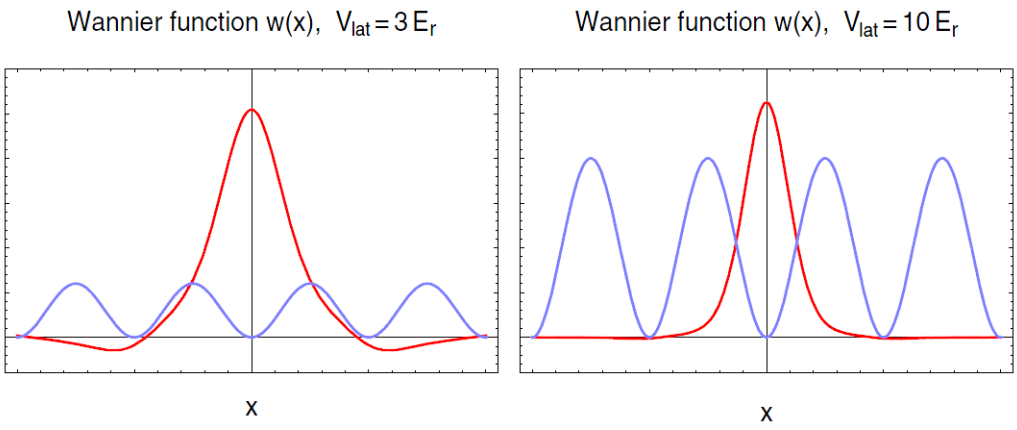

Figure 2.3: (Reproduced from [10]) The Wannier wave function centered at one site in the lattice with the lattice depth being 3 (left panel) and 10 (right panel) recoil energy. .

wave function is well localized on a single site with a small tail extending to its neighbor sites. For such a case, the tight-binding model will describe the system with the tunneling energy given by

$$J = -\int d^3\mathbf{r} w^*(\mathbf{r}-\mathbf{r}_i)\left[-\hbar^2\nabla^2/2m + V_\ell(\mathbf{r})\right] w(\mathbf{r}-\mathbf{r}_j), \tag{2.26}$$

where $w(\mathbf{r}-\mathbf{r}_i)$ and $w(\mathbf{r}-\mathbf{r}_j)$ are the Wannier wave functions localized to the nearest neighbor sites i and j respectively.

Now we consider the system of n interacting bosons on each site. If the particles are dilute enough ($na_s^3/d^3 \ll 1$) and the interaction energy is small compared to the band gap, we can assume that every particle stays in the lowest energy band with the wave function the same as the one-particle Wannier wave function. Therefore, the tight-binding model still works and is modified by adding on-site interaction terms. Combining the tunneling, interaction, and potential energies, we write down the Hamiltonian,

$$\hat{H}_{\mathrm{BH}} = \quad - \quad J\sum_{\langle ij\rangle}\left(\hat{a}_i^\dagger\hat{a}_j + \hat{a}_j^\dagger\hat{a}_i\right) + \sum_i\left[\frac{U}{2}\hat{n}_i(\hat{n}_i-1) - (\mu - V_i)\hat{n}_i\right]. \tag{2.27}$$

Similar to the Hubbard Hamiltonian for the fermion system, $\hat{H}_{\mathrm{BH}}$ is called the Bose-Hubbard Hamiltonian. Here $\hat{a}_i$ and $\hat{a}_i^\dagger$ are the bosonic annihilation and creation operators on the ith lattice site respectively, and $\hat{n}_i = \hat{a}_i^\dagger\hat{a}_i$ is the number operator on the ith lattice site. $\sum_i$ denotes the sum over all single sites, and $\sum_{\langle ij\rangle}$ denotes the sum over all nearest-neighbor pairs of sites. the chemical potential is denoted by μ, which is determined by the condition that the quantity $\sum_i\langle\hat{n}_i\rangle$ is equal to the total number of bosons, N. V_i is the value of the external confining potential on site i. For a homogeneous is set to zero for convenience. J is the one-particle tunneling energy given in Eq. (2.26). U represents the interaction between two bosons on

a single site and is given by

$$U = \frac{4\pi\hbar^2 a_s}{m} \int d^3\mathbf{r}\, |w(\mathbf{r})|^4 \,. \tag{2.28}$$

In experiments, the controllable parameters are the lattice depth, V_0, and the lattice spacing, $d_\ell = \lambda/2$, which in a deep lattice are related to J and U by [72]

$$\begin{aligned} J &= \frac{4}{\sqrt{\pi}} E_R \left(\frac{V_0}{E_R}\right)^{3/4} \exp\left[-2\sqrt{\frac{V_0}{E_R}}\right] \\ U &= 4\sqrt{2\pi}\frac{a_s}{\lambda} E_R \left(\frac{V_0}{E_R}\right)^{3/4}. \end{aligned} \tag{2.29}$$

The Bose-Hubbard Hamiltonian has $U(1)$ symmetry, or equivalently, it commutes with the total number operator $\hat{N} \equiv \sum_{i=1}^{M} \hat{n}_i$. Therefore, it is block-diagonalized with each block spanned by states corresponding to the same eigenvalue of $\hat{N}$. The chemical potential determines the total number of particles of the system by identifying the block on which the ground state of $\hat{H}_{\rm BH}$ is located. We can study a closed system by staying on this block to conserve the total number of particles.

2.3 Condensate-Mott-insulator transition

In the last two sections, we discussed related physics of a general case of BEC and the optical lattice system, separately. Starting from this section, we enter the key features of the lattice boson system. We begin with two specific exact solutions of the Bose-Hubbard Hamiltonian, and we apply the mean-field theory to a uniform Bose-Hubbard model in a general parameter regime in Subsection 2.3.1. We express the physical quantities, such as number density, number fluctuations, condensate fraction and compressibility, in an expansion of the mean-field order parameter. We illustrate the phase diagram as a function of tunneling energy and chemical potential of the system, relative to the interaction energy. The phase diagram displays the Mott-insulating phase, corresponding to the parameter regions where the condensate fraction is zero but the compressibility is non-zero, and the BEC phases, corresponding those with zero compressibility but finite condensate fraction. In Subsection 2.3.2, we discuss the coexistence of BEC and Mott-insulating phases in a 3D spherically trapped system with the local density approximation (LDA) analysis. We show the existence of a wedding-cake-like density profile in the deep lattice regime, which indicates the system has a concentric shell structure with the Mott-insulator shells and the condensate shells appearing alternatively.

For the uniform case of the Bose-Hubbard Hamiltonian ($V_i = 0$), the eigen states have exact solutions in

the zero tunneling or zero interaction regime. At $U = 0$, the Hamiltonian is diagonalized in the momentum space. The ground state is given by

$$|\psi_g\rangle = \mathcal{A}\left(\hat{a}_{k=0}^{\dagger}\right)^N |\text{vac.}\rangle = A\left(\sum_{i=1}^{M} \hat{a}_i^{\dagger}\right)^N |\text{vac.}\rangle\,, \tag{2.30}$$

where $\hat{a}_k$ is the Fourier transformation of $\hat{a}_i$, and M are the total numbers of particles and sites respectively, $|\text{vac.}\rangle$ is the vacuum state, and $\mathcal{A}$ is the normalization constant. The ground state of Eq. (2.30) shows that all the particles stay in the lowest momentum state, so the system is a 100% BEC. At $J = 0$, the Hamiltonian is site-decoupled as a sum of single-site Hamiltonians. The ground states is thus a product of the single-site states each of which is the ground state of the single-site Hamiltonian,

$$|\Psi_g\rangle = \prod_{i=1}^{M} |n\rangle_i \equiv ||n\rangle\rangle\,, \tag{2.31}$$

where the integer n satisfies

$$\frac{\mu}{U} < n < \frac{\mu}{U} + 1, \tag{2.32}$$

and $|n\rangle_i \equiv \mathcal{A}(\hat{a}_i^{\dagger})^n |\text{vac.}\rangle$ represents the state of n particles localized on site i. The ground state of Eq. (2.30) shows that every particle is localized to a certain site, and no single-particle state is macroscopically occupied, which means no BEC. If μ/U is not an integer, Eq. (2.32) indicates that the system is incompressible because

$$\frac{\partial\langle N\rangle}{\partial\mu} = M\frac{\partial\langle n\rangle}{\partial\mu} = 0. \tag{2.33}$$

A quantized value of the density at each site implies an energy gap between the ground state and excitations. Such a non-condensed phase with zero compressibility and energy gap to excitations is known as a Mott insulator. The ground state of Eq. (2.31) can be generalized to the inhomogeneous system by replacing μ with the local chemical potential $\tilde{\mu}_i \equiv \mu = V_i$, and n with a site dependent number n_i satisfying $\tilde{\mu}_i/U < n < \tilde{\mu}_i/U + 1$.

The BEC phase at $U = 0$ and the Mott-insulating phase at $J = 0$ implies a critical value of the ratio $(J/U)_c$, at which a quantum phase transition happens. At a general value of J/U, the Bose-Hubbard Hamiltonian does not have a simple solution. In the following subsections, we use a mean-field approach to determine the critical value for a uniform system and apply the result on the inhomogeneous system.

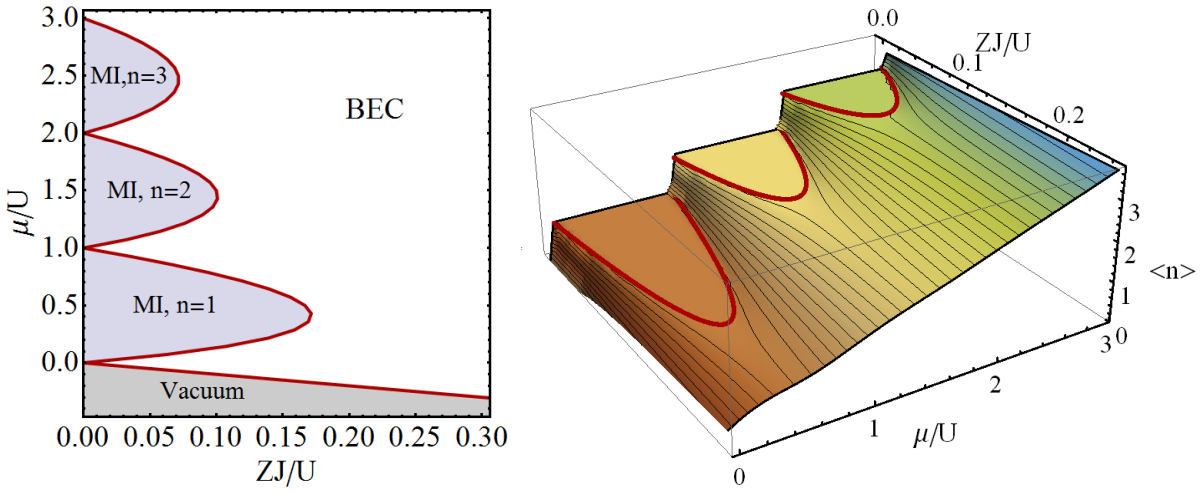

Figure 2.4: Left: the mean-field phase diagram of the Bose-Hubbard model showing the Mott-insulating (MI) phases with commensurate occupation n, the BEC phase, and vacuum, as a function of μ/U and J/U. Right: a three dimensional profile of the phase diagram with the z axis being the number density. The thick red curves, corresponding to those in the left panel, show the phase boundary between MI and BEC phases, while the thin black curves in the BEC region represent equal contours of the number density. The flat plateaus (wherein no contours) in the MI regions imply zero compressibility.

2.3.1 Mean-field approach

In this subsection, we follow a simple idea to apply the mean-field approach, trying to capture main physical properties of the Bose-Hubbard model. Although in the mean-field treatment we ignore effects of quantum fluctuations from neighboring sites, the mean-field results are well compared to other theoretical approaches such as quantum Monte Carlo simulations [43, 44] and the density matrix renormalization group method [45]. The strategy of the mean-field approach is to approximate the uniform Bose-Hubbard Hamiltonian (Eq. (2.27) with $V_i = 0$) with the sum of single-site Hamiltonians. The mean-field Hamiltonian is

$$H_{\mathrm{MF}} = \sum_i -\psi_i \hat{a}_i^\dagger - \psi_i^* \hat{a}_i + \frac{U}{2}\hat{n}_i(\hat{n}_i - 1) - \mu \hat{n}_i, \tag{2.34}$$

with a complex variational parameter ψ, or a mean-field, which is physically interpreted the influence from neighbor sites. If $\psi = 0$, H_{MF} reduces to the Bose-Hubbard Hamiltonian with $J = 0$ and hence describes the Mott insulators. If $\psi \neq 0$, the mean-field terms break the $U(1)$ symmetry and the conservation of total number of particles. The $U(1)$ symmetry breaking will lead to (1) non-zero off-diagonal long range order in the single-particle density matrix, which leads to a condensed state [61]; (2) non-zero stiffness to rotations of the order parameter, which implies the superfluidity of the system [73]. In experiments, superfluid currents have been directly observed in a full BEC regime in a moving optical lattice [74, 75]. However, in the shell

BEC region in the deep optical lattice, the superfluid current is set to be discovered.

The general solution to the mean-field Hamiltonian is the Gutzwiller wave function [76], given by

$$|\Psi_{\mathrm{MF}}\rangle = \prod_{i=1}^{M} \left(\sum_{n=0}^{\infty} f_n^{(i)} |n\rangle_i \right), \tag{2.35}$$

where the amplitude $f_n^{(i)}$ is a functional of the mean-field ψ, and so is $|\Psi_{\mathrm{MF}}\rangle$. To self-consistently determine the value of the mean-field, we require that the lowest energy state of the mean-field Hamiltonian, $|\Psi_{\mathrm{MF,g}}\rangle$, also minimizes the Bose-Hubbard Hamiltonian. The condition is

$$\frac{\delta \langle \hat{H}_{\mathrm{BH}} \rangle}{\delta \psi} \equiv \frac{\delta \langle \Psi_{\mathrm{MF,g}} | \hat{H}_{\mathrm{BH}} | \Psi_{\mathrm{MF,g}} \rangle}{\delta \psi} = 0. \tag{2.36}$$

Once ψ is determined by Eq. (2.36), the corresponding wave function is the best approximated wave function to the Bose-Hubbard model.

$\langle \hat{H}_{\mathrm{BH}} \rangle$ as a functional of ψ can be numerically obtained by solving for the Gutzwiller wave function with an appropriate truncation. An analytic form of the energy and the ground state can be derived when ψ is small, or equivalently, when $(J/U) \to (J/U)_c$. In this regime, we treat the mean-field terms as a small quantity and perturbatively solve the mean-field Hamiltonian with the unperturbed basis being the Mott-insulating state. Following the standard procedure of the perturbation theory, we get the ground state energy and the corresponding wave function for a single site in series of ψ,

$$\langle \hat{H}_{\mathrm{BH}} \rangle = E_{\mathrm{Mott}} + \chi(1 - ZJ\chi)|\psi|^2 + \mathcal{O}(\psi^4), \tag{2.37}$$

$$|\varphi\rangle = |n\rangle + \sqrt{n}\gamma\psi^* |n-1\rangle + \sqrt{n+1}\bar{\gamma}\psi |n+1\rangle + \mathcal{O}(\psi^2). \tag{2.38}$$

Here $\gamma \equiv [\mu - U(n-1)]^{-1}$, $\bar{\gamma} \equiv [Un - \mu]^{-1}$, and $\chi \equiv n\gamma + (n+1)\bar{\gamma}$ are known from Eq. (2.32) to be positive. Z is the coordination number and equal to 6 in 3D lattices. E_{Mott} and $|n\rangle$ are the ground state energy and the corresponding single-site state of the unperturbed terms, respectively. Once the ground state is given, we compute the number density, number fluctuation, condensate fraction, and compressibility as

$$\langle \hat{n} \rangle = n + [(n+1)\bar{\gamma}^2 - n\gamma^2]|\psi|^2 + O(\psi^4), \tag{2.39}$$

$$\Delta n^2 = \langle \hat{n}^2 \rangle - \langle \hat{n} \rangle^2 = [(n+1)\bar{\gamma}^2 + n\gamma^2]|\psi|^2, \tag{2.40}$$

$$f_c = \frac{\langle \hat{a}^\dagger \rangle \langle \hat{a} \rangle}{\langle \hat{a}^\dagger \hat{a} \rangle} = \frac{|\langle \hat{a} \rangle|^2}{\langle \hat{n} \rangle} = \frac{\chi^2}{n}|\psi|^2 + O(\psi^4), \tag{2.41}$$

$$\frac{\partial \langle \hat{n} \rangle}{\partial \mu} = 2[(n+1)\bar{\gamma}^3 + n\gamma^3]|\psi|^2 + O(\psi^4). \tag{2.42}$$

The condensate fraction f_c is given by Eq. (2.3). Inserting Eq. (2.37) into Eq. (2.36), we see that if $\chi(1 - ZJ\chi) > 0$, $\psi = 0$, and the system is a Mott-insulator with integer density and number fluctuation, condensate fraction, and compressibility. If $\chi(1 - ZJ\chi) < 0$, $\psi \neq 0$. The system is a condensate which has non-integer density. The number fluctuation, condensate fraction, and compressibility are all proportional to $|\psi|^2$.

Figure 2.4a shows the phase diagram in the plane of J/U and μ/U. The phase boundary is given by $\chi(1-ZJ\chi) = 0$. The shaded region is the Mott insulator (MI) with each lobe accommodating integer bosons, starting from zero with rise in the chemical potential. The white region is the BEC phase, which has non-zero compressibility and non-zero condensate fraction. Figure 2.4b shows the profile of the density in a 3D view, with the contours denoting the number density. The slope of the tangent along the μ direction represents the compressibility $\partial\langle\hat{n}\rangle/\partial\mu$. It is clear to see that in the Mott "plateau", the system is incompressible.

In a uniform system, if we lower J/U by changing lattice depth and interaction between particles but keep the total number of particles fixed, the system will go along a contour path in Figure 2.4b. The the number density in that contour is non-commensurate, the system never undergoes a phase transition from a BEC to a Mott-insulator. However, in an inhomogeneous system, when J/U decreases, the density profile will redistribute and the condensate-Mott-insulator transition happens in local regions. As a result, condensates and Mott-insulators co-exist but spatially separate in the system. We will discuss this phenomenon in the next subsection.

2.3.2 Coexistence of condensate and Mott-insulator

In experiments, the optical lattice is inhomogeneous due to an applied confining potential to trap the atoms. Although the confining potential breaks the translational invariance, the result of the uniform system is still useful to describe the inhomogeneous system under certain conditions. If the potential variance over a group of sites centering on site i is small compared to the band gap, these sites can be treated as a uniform system with the chemical potential $\tilde{\mu}_i = \mu - V_i$, where V_i is the confining potential on site i and $\tilde{\mu}_i$ is called local chemical potential, distinguished from the chemical potential of the global system, μ. In this approximation, called local density approximation (LDA), once the local chemical potential is known, the local properties are identified as those at the corresponding point in the phase diagram of the uniform system.

If the confinement is the spherical harmonic potential, as the last term in Eq. (2.24), the local chemical potential is monotonically decreasing from the center of the sphere to the edge. Given that the center local chemical potential corresponds to the $n = 2$ Mott-insulator, the local state from the center to the edge will vary between different phases, following the arrow shown in Figure 2.5a. As a result, the system has Mott-

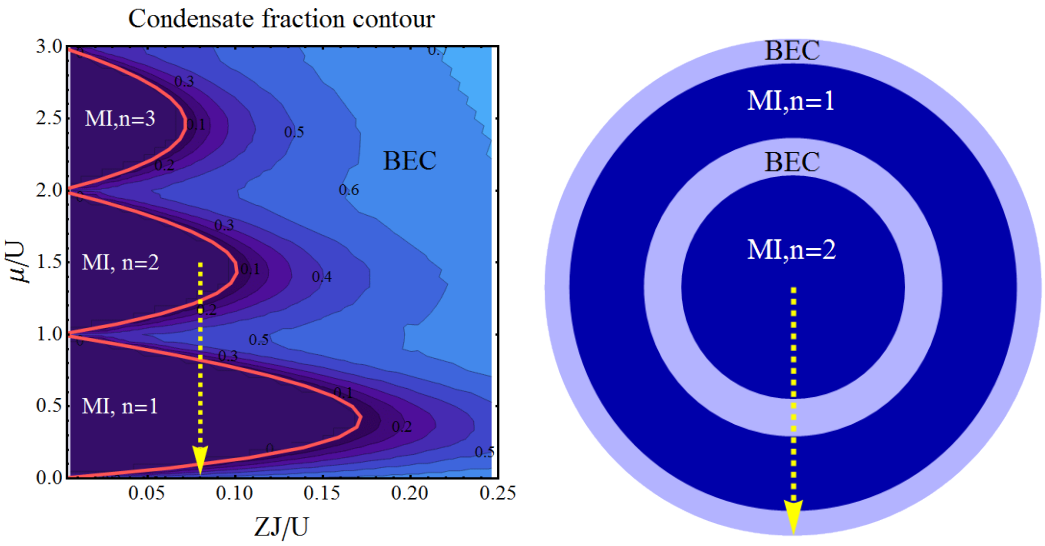

(a) (b)

Figure 2.5: (a) the phase diagram with contours illustrating the condensate fraction. (b) Section cut of the wedding-cake structure, with the local chemical potential along the dotted arrow corresponding to that in panel (a).

insulator phases and condensate phases spatially separated. Figure 2.5b shows a concentric shell structure of the system, with shells of the Mott-insulator and condensate appearing alternatively. The density profile of this system looks like a sectional view of a wedding cake. In the large J/U region, the trace of the local chemical potential will not pass through the Mott-insulator lobes. Thus the density profile goes smoothly and the whole system is a condensate. Figure 2.6 shows several the density and order parameter profiles with increasing ZJ/U (decreasing lattice depths). We see how the wedding-cake structure emerges with increasing depths (decreasing ZJ/U).

In experiments, the atoms are trapped and cooled down below the critical temperature, and then the lattice potential is adiabatically turned on. According to the discussion above, we expect that during this process, (1) the system is a BEC in the shallow lattice regime, (2) the condensate fraction suddenly drops when the lattice depth touch a critical value, and (3) the wedding-cake density profile develops in the deep lattice regime. (1) and (2) have been observed in the experiment of matter wave interference [20]. The existence and formation of the Mott-insulating shells on (3) have been shown in the experiment of radio-frequency (RF) spectroscopy [38, 40]. Even in the deep lattice regime where the Mott-insulating plateaus are well developed, the LDA shows that the system still has a thin condensate shell between two adjacent Mott-insulators. Currently, however, no strong experimental evidence unequivocally verifies the existence or properties of such putative condensate layers. In the following sections, we investigate the equilibrium and dynamical properties of the condensates in the vicinity of Mott insulators in deep lattice regime, and

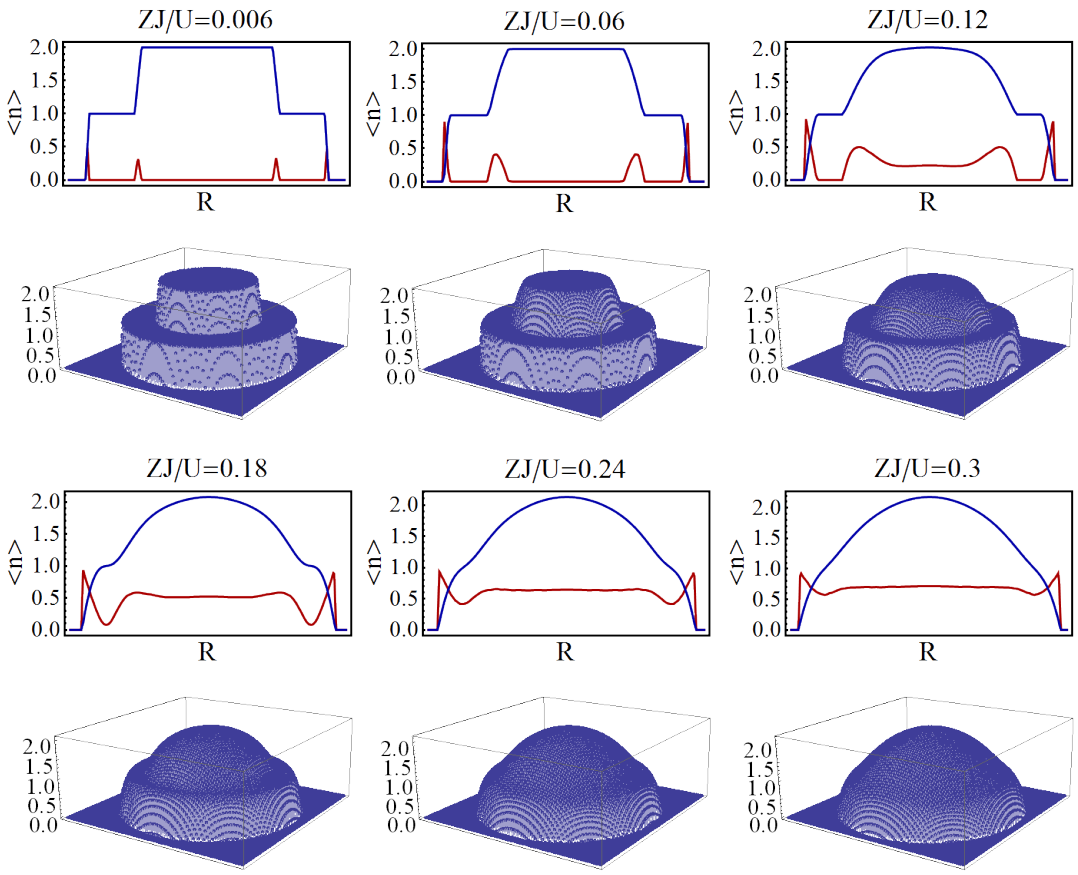

Figure 2.6: The first and third rows: Number density (blue) and condensate fraction (red) profiles at $ZJ/U = 0.006$, 0.06, 0.12, 0.18, 0.24, and 0.3. The second and forth rows: the corresponding density profiles in a 3D view.

discuss two experimental signatures of the condensate.

2.4 Condensate in deep lattice regime

In the last section, we indicated that in the deep lattice regime the system exhibits the wedding-cake-like structure in which between two Mott-insulating regions are a thin shell of condensate. This condensate shell has not been experimentally identified yet. In order to have more understanding about the condensate shell, in this section, we investigate a general BEC in the deep lattice region.

In a sufficiently deep lattice ($J/U \ll 1$), the condensate exists in a quite narrow region between two Mott-insulating lobes in the phase diagram. In this region, the Hamiltonian and low energy states of the system are well represented in a highly truncated basis composed of only two states of each site. Effects contributed from the other states are smaller than those from the two states by at least an order of J/U,

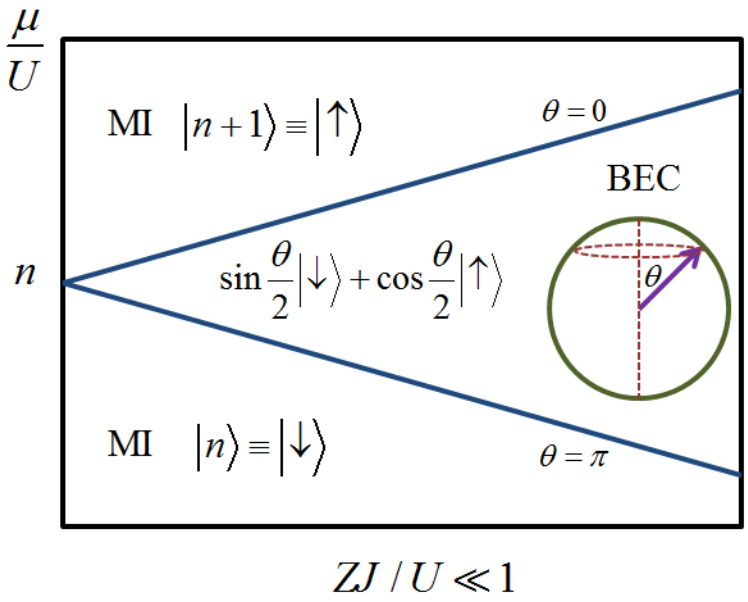

Figure 2.7: The phase diagram in deep lattice regime ($ZJ/U \ll 1$) around $\mu/U = n$, and the corresponding pseudo-spin states.

which can be ignored. If we relate the two states to the eigen states of the spin-1/2 system, the Bose-Hubbard Hamiltonian is mapped onto the quantum XXZ model for spins [77, 78, 73, 79, 35]. This mapping guarantees a one-to-one correspondence between the ground state and excitations of the condensate and those of the spin system, which helps us understand the dynamics of the condensate by making analogy to the physics of magnetism.

The advantage of the truncation allows us to construct a fixed-number ground state that keeps the $U(1)$ symmetry and use it to compute the condensate properties. The fixed-number ground state shows the same one-particle density matrix as the mean-field ground state but exhibits quantum entanglement between sites that the mean-field solutions do not have.

This section is organized as follows. In Subsection 2.4.1, we introduce the pseudo-spin model and use it to study the ground state and excitations of the condensate, based on the mean-field approach. We also calculate the condensate properties with a fixed-number basis (Subsection 2.4.2) and compare them with the mean-field solutions.

2.4.1 Pseudo-spin model

In this subsection, we introduce the pseudo-spin Hamiltonian and show the mapping between it and the Bose-hubbard Hamiltonian in a truncated representation. We give the mean-field solution of the pseudo-spin Hamiltonian and express the number density, number fluctuation, condensate fraction and compressibility

in terms of the pseudo-spin parameters. We discuss the excitations of the uniform deep lattice system by considering Goldstone modes in the pseudo-spin system. Finally we use the pseudo-spin language to estimate the critical temperature T_c, above which the condensate order becomes zero.

Considering the region between the n and $n+1$ Mott-insulating lobes, we choose the two number states $|n+1\rangle$ and $|n\rangle$ to form the truncated basis and map them onto the spin states as $|n+1\rangle \rightarrow |\uparrow\rangle$ and $|n\rangle \rightarrow |\downarrow\rangle$. The operators thus have the correspondence,

$$\hat{a} \rightarrow \sqrt{n+1}\hat{S}^- \tag{2.43}$$

$$\hat{a}^\dagger \rightarrow \sqrt{n+1}\hat{S}^+ \tag{2.44}$$

$$\hat{n} \rightarrow n + \frac{1}{2} + \hat{S}^z. \tag{2.45}$$

We replace the operators in the Bose-Hubbard Hamiltonian with the corresponding spin operators and obtain the pseudo-spin Hamiltonian

$$\hat{H}_{\mathrm{PS}} = -J(n+1)\sum_{\langle ij\rangle}\left(\hat{S}_i^x\hat{S}_j^x + \hat{S}_i^y\hat{S}_j^y\right) + \sum_i (Un - \tilde{\mu}_i)\hat{S}_i^z. \tag{2.46}$$

For the uniform case, the mean-field approach site-decouples $\hat{H}_{\mathrm{PS}}$ and yields the single-site state as

$$|\varphi\rangle = e^{i\phi/2}\sin\frac{\theta}{2}|\downarrow\rangle + e^{-i\phi/2}\cos\frac{\theta}{2}|\uparrow\rangle, \tag{2.47}$$

where the parameters θ and ϕ represent the spherical angles of the expectation value of the spin, as shown in Figure 2.7. In the pseudo-spin model, the Mott-insulator state is represented by a state where all the pseudo-spins of the system are either all up or all down along the z direction ($\theta = 0$ or π). The condensate state is represented by a state in which the pseudo-spins point in a direction θ determined by the chemical potential and a direction ϕ determined by spontaneous symmetry breaking. For the ground state, we set $\phi = 0$ for convenience and find

$$\cos\theta = \frac{\mu - nU}{(n+1)ZJ}. \tag{2.48}$$

The number density and fluctuation on a single site, the condensate fraction, and the compressibility are found to be:

$$\langle\hat{n}\rangle = n + \cos^2(\theta/2), \tag{2.49}$$

$$\Delta n^2 = \cos^2(\theta/2)\sin^2(\theta/2), \tag{2.50}$$

$$f_c = \frac{(n+1)\cos^2(\theta/2)\sin^2(\theta/2)^2}{n+\cos^2(\theta/2)} = \frac{(n+1)\Delta n^2}{\langle\hat{n}\rangle}, \tag{2.51}$$

$$\frac{\partial\langle\hat{n}\rangle}{\partial\mu} = \frac{1}{2(n+1)ZJ}. \tag{2.52}$$

The physical quantities are consistent with the Mott-insulating state when $\theta = 0$ or π, except the compressibility is supposed to suddenly drop to zero at the phase boundary. The compressibility of the condensate is large in the deep lattice and independent of density and interaction, and the condensate fraction is less than 35% for all $n > 0$, quite different from the large J/U regime or the dilute gas which is an almost 100% BEC.

The elementary excitation of the condensate is understood by studying the corresponding excitation of the pseudo-spin system. Low energy excitations of a system such as this with spontaneous symmetry breaking are Goldstone modes. In the pseudo-spin system, the Goldstone modes are long range spin waves, which describes the picture that all spins slightly deviate from and collectively precess around their equilibrium direction. These excitations can be described using Holstein-Primakoff bosons, denoted as $\hat{A}$ and $\hat{A}^\dagger$. We substitute the transformation

$$\begin{aligned}
\hat{S}^x &= \frac{\cos\theta}{2}(\hat{A}+\hat{A}^\dagger) + \sin\theta(\frac{1}{2} - \hat{A}^\dagger\hat{A}), \\
\hat{S}^y &= \frac{i}{2}(\hat{A}+\hat{A}^\dagger), \\
\hat{S}^z &= -\frac{\sin\theta}{2}(\hat{A}+\hat{A}^\dagger) + \cos\theta(\frac{1}{2} - \hat{A}^\dagger\hat{A}),
\end{aligned} \tag{2.53}$$

into the pseudo-spin Hamiltonian of Eq. (2.46), keep terms up to quadratic order, Fourier transform them in the momentum space,

$$\begin{aligned}
\hat{H}_{\rm PS} &= J(n+1)\{\frac{1}{4}\sum_{\langle ij\rangle}[(1-\cos\theta_i\cos\theta_j)(A_i^\dagger A_j^\dagger + A_i A_j) - (1+\cos\theta_i\cos\theta_j)(A_i^\dagger A_j + A_j^\dagger A_i)] \\
&\quad + \sum_i A_i^\dagger A_i\} \qquad (2.54) \\
&= ZJ(n+1)\sum_{\mathbf{p}}\{\frac{I_{\mathbf{p}}}{4}\sin^2\theta(A_{\mathbf{p}}^\dagger A_{-\mathbf{p}}^\dagger + A_{-\mathbf{p}}A_{\mathbf{p}}) + [1 - \frac{I_{\mathbf{p}}}{2}(1+\cos^2\theta)]A_{\mathbf{p}}^\dagger A_{\mathbf{p}}\}, \qquad (2.55)
\end{aligned}$$

where $\hat{A}_{\mathbf{p}} = M^{-1/2}\sum_{\mathbf{p}} e^{-i\mathbf{p}\cdot\mathbf{r}_i}\hat{A}_i$, $I_{\mathbf{p}} = D^{-1}\sum_{x=1}^{D}\cos d_\ell p_x$ for D dimension, and $\theta_i = \theta_j = \theta$ in the uniform system. Eq. (2.55) is diagonalized by a Bogoliubov transformation $\alpha_{\mathbf{p}} = u_{\mathbf{p}}A_{\mathbf{p}} - v_{\mathbf{p}}A_{-\mathbf{p}}^\dagger$, where the quasi-

particle amplitudes u and v satisfy

$$\begin{aligned} u_{\mathbf{p}}^2 - v_{\mathbf{p}}^2 &= 1 \\ u_{\mathbf{p}} v_{\mathbf{p}} &= \frac{-I_{\mathbf{p}} \sin^2\theta}{4\sqrt{(1 - I_{\mathbf{p}}\cos^2\theta)(1 - I_{\mathbf{p}})}}. \end{aligned} \tag{2.56}$$

Finally we obtain $\hat{H}_{\rm PS} = \sum_{\mathbf{p}} \epsilon_{\mathbf{p}} \alpha_{\mathbf{p}}^\dagger \alpha_{\mathbf{p}}$ with the spectrum

$$\epsilon_{\mathbf{p}} = ZJ(n+1)\sqrt{(1 - I_{\mathbf{p}}\cos^2\theta)(1 - I_{\mathbf{p}})}. \tag{2.57}$$

In the low momentum limit ($d_\ell p \ll 1$), $\epsilon_p = J(n+1)\sqrt{Z\sin^2\theta (d_\ell p)^2 + \cos^2\theta (d_\ell p)^4}$, which is of the same form as the spectrum of dilute BEC in continuum space, given by Eq. (2.15). In the deep condensate regime ($\sin\theta \gg d_\ell p$) the low-energy excitations are wave-like (energy $\propto p$), while near the Mott boundary ($\sin\theta \ll d_\ell p$) they are particle-like (energy $\propto p^2$).

In an inhomogeneous system, the elementary excitation is the collective motion of particles in the bulk or on the surface of the condensate. In the next subsection, we apply the pseudo-spin model on the trapped system. We derive the spectrum of the collective modes and show how it is related to the geometry of the condensate.

At the end of this subsection, we derive the critical temperature for the uniform condensate. In equilibrium, a pseudo-spin is aligned with the local magnetic field, with the z component due to an external field and the transverse component coming from the neighbor spins. At the mean-field level, the one-site Hamiltonian is given by

$$\hat{H}_1 = -ZJ(n+1)(\langle \hat{S}^x \rangle_T \hat{S}^x + \langle \hat{S}^y \rangle_T \hat{S}^y + \cos\theta \hat{S}^z). \tag{2.58}$$

Here we use the identity of Eq. (2.48) to replace the interaction and the chemical potential terms. The thermal average are denoted as $\langle \cdots \rangle_T$. To find the critical temperature, we look at the transverse field, defined as $S_\perp = \sqrt{\langle \hat{S}^x \rangle_T^2 + \langle \hat{S}^y \rangle_T^2}$, which corresponds to the condensate magnitude in the Bose-Hubbard system. $S_\perp$ is self-consistently determined. The density matrix is

$$\hat{\rho} = \frac{e^{-\beta \hat{H}_1}}{\mathrm{Tr}[\mathrm{e}^{-\beta \hat{\mathrm{H}}_1}]} = \frac{1}{2} + \frac{\tanh[ZJ(n+1)\sqrt{S_\perp^2 + \cos^2\theta}/2k_BT]}{\sqrt{S_\perp^2 + \cos^2\theta}} (\langle \hat{S}^x \rangle_T \hat{S}^x + \langle \hat{S}^y \rangle_T \hat{S}^y + \cos\theta \hat{S}^z), \tag{2.59}$$

and obtain the transverse field

$$S_\perp = \sqrt{\mathrm{Tr}[\hat{\mathrm{S}}^{\mathrm{x}}\hat{\rho}]^2 + \mathrm{Tr}[\hat{\mathrm{S}}^{\mathrm{y}}\hat{\rho}]^2} = \frac{\tanh[ZJ(n+1)\sqrt{S_\perp^2+\cos^2\theta}/2k_BT]}{\sqrt{S_\perp^2+\cos^2\theta}} S_\perp. \tag{2.60}$$

Eq. (2.60) has a trivial solution $S_\perp = 0$, which corresponds to the state in the Mott-insulating region and is temperature independent. The critical temperature is given by letting the non-trivial solution approach zero.

$$k_B T_c = \frac{ZJ(n+1)\,|\cos\theta|}{2\tanh^{-1}|\cos\theta|} \tag{2.61}$$

As expected, the critical temperature goes to zero when the state approaches to the Mott insulator ($|\cos\theta| \to 1$). The maximum critical temperature is $ZJ(n+1)/2$ at $|\cos\theta| = 0$, the same point at which the transverse field reaches its maximum.

2.4.2 Collective motion of the condensate

For the inhomogeneous system, as we discussed in the previous section, the density profile exhibits a wedding-cake shape in the deep lattice regime. The condensate is confined either in a spherical core surrounded by a Mott-insulating shell or in a thin shell between two Mott-insulating shells. Because the condensate is compressible and long-range ordered, we expect the elementary excitation to be a collective fluctuation in density and current, similar to the collective motion in a dilute BEC gases described in Subsection 2.1.3. In this subsection, we study the dynamics of pseudo-spins in an inhomogeneous field. We take the continuum limit and derive a differential equation for the collective modes and the corresponding frequencies. Finally we compare the results with dilute BEC gases.

We begin with the Heisenberg equation of a pseudo-spin on site i, $\partial_t \hat{\mathbf{S}}_i = i[\hat{H}_{\mathrm{PS}}, \hat{\mathbf{S}}_i]$, where $\hat{H}_{\mathrm{PS}}$ is given by Eq. (2.46). The result takes the form of the Bloch equations $\partial_t \hat{\mathbf{S}}_i = \hat{\mathbf{S}}_i \times \hat{\mathbf{B}}_i$, where the effective magnetic field is given by

$$\hat{\mathbf{B}}_i = J(n+1)\left(\sum_{j\ \text{near}\ i} \hat{S}_j^x, \sum_{j\ \text{near}\ i} \hat{S}_j^y, \frac{\tilde{\mu}_i - Un}{J(n+1)}\hat{S}_i^z\right). \tag{2.62}$$

In the mean-field approximation and the continuum limit, we define the field $\mathbf{S}(\mathbf{r}_i) \equiv \left\langle \hat{\mathbf{S}}_i \right\rangle$ and rewrite the magnetic field as

$$\mathbf{B}(\mathbf{r}) = ZJ(n+1)\left((1+Z^{-1}d_\ell^2\nabla^2)S^x(\mathbf{r}), (1+Z^{-1}d_\ell^2\nabla^2)S^y(\mathbf{r}), \cos\theta(\mathbf{r})S^z(\mathbf{r})\right), \tag{2.63}$$

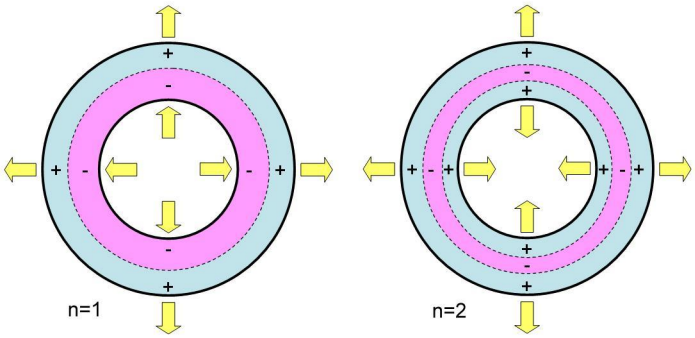

Figure 2.8: The sign of the radial part of δn is marked in the shell. The arrows show the direction of the collective motion.

where d_ℓ is the lattice spacing, $\cos\theta(\mathbf{r}) = [\tilde{\mu}(\mathbf{r}) - Un]/ZJ(n+1)$, and the relation

$$\sum_{j \text{ near } i} \left\langle \hat{S}_j^{x,y} \right\rangle = ZS^{x,y}(\mathbf{r}_i) + d_l^2 \nabla^2 S^{x,y}(\mathbf{r}_i) \tag{2.64}$$

is applied. Individual components of the Bloch equation read

$$\begin{aligned} \partial_t S^x &= ZJ(n+1)[S^z(1 + Z^{-1}d_l^2\nabla^2) - \cos\theta]S^y \\ \partial_t S^y &= ZJ(n+1)[\cos\theta - S^z(1 + Z^{-1}d_l^2\nabla^2)]S^x \\ \partial_t S^z &= J(n+1)d_l^2\nabla(S^y\nabla S^x - S^x\nabla S^y). \end{aligned} \tag{2.65}$$

In the ThomaS/Fermi limit, we ignore the second order derivatives and obtain the equilibrium state $\mathbf{S}_0$ by letting $\partial_t \mathbf{S}_0 = 0$ in Eq. (2.65), which yields $\mathbf{S}_0 = (\sin\theta, 0, \cos\theta)$. Here we take advantage of the spontaneously broken symmetry and choose $S_0^y = 0$.

Now we consider a small oscillation of the spin field around the equilibrium value, $\mathbf{S} = \mathbf{S}_0 + \delta\mathbf{S}e^{i\omega t}$, apply the ThomaS/Fermi approximation, replace δS^x and δS^y by δS^z, and finally write down an eigen equation for δS^z

$$\omega^2 \delta S^z = -Z[J(n+1)d_\ell]^2[\nabla(\sin^2\theta)\cdot\nabla\delta S^z + (\sin^2\theta)\nabla^2\delta S^z]. \tag{2.66}$$

Eq. (2.66) is of the same form as Eq. (2.20). If we look at the correspondence to the Bose-Hubbard model, $\delta S^z \propto \delta\langle\hat{n}\rangle$ is the particle density fluctuation, and $\sin^2\theta \propto \langle\hat{n}\rangle f_c$ is the condensate density. Therefore, the condensate of dilute BEC gases and that of bosons in deep lattices have the same collective excitations. The spectrum is determined by the density profile (or the geometry) of the condensate.

We use Eq.(2.21) to compute the collective modes for a 3D thin condensate shell of radius r_0 and

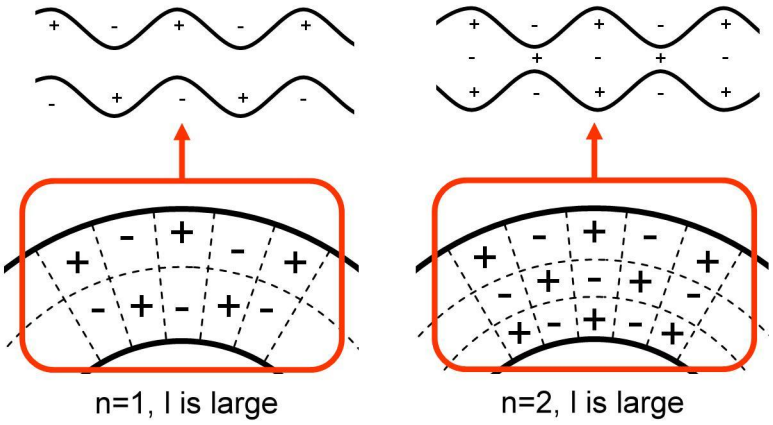

Figure 2.9: Part of the thin shell oscillation with large l. The $n = 1$ mode corresponds to the in-phase oscillation of two boundaries of the thin shell. The $n = 2$ modes corresponds to the out-of-phase oscillation.

thickness $2a_0$ between two Mott-insulators. From Eq.(2.48), we know that the chemical potential range for the condensate is $2ZJ(n+1)$, so we estimate $a_0 = ZJ(n+1)/V'(r_0) = 6J(n+1)/(m\omega^2 r_0)$, where $V(r) = m\omega^2 r^2/2$ is the spherical harmonic trap and $J = 6$ in 3D. The condensate density is approximated as

$$n_0 = \frac{(n+1)}{4}\sin^2\theta = \frac{(n+1)}{4}\left[1 - \frac{(r-r_0)^2}{a_0^2}\right]. \tag{2.67}$$

We substitute Eq. (2.67) into Eq.(2.21) and make it dimensionless by letting $x = (r - r_0)/a_0$, $c = r_0/a_0$, $\lambda = (\omega a_0)^2/3[J(n+1)d_\ell]^2$, and $y(x)/(x+c) = \delta n(r)$. The eigen equation becomes

$$(1-x^2)y'' - 2xy' + [\lambda + \frac{2x}{x+c} - l(l+1)\frac{1-x^2}{(x+c)^2}]y = 0, \quad -1 \le x \le 1. \tag{2.68}$$

In the limit of $c \to \infty$, the last two terms of Eq. (2.68) is ignored. The solutions are the Legendre polynomials $y_n(x) = \sqrt{n+1/2}P_n(x)$, with eigenvalues $\lambda = n(n+1)$. At the regime of $c \gg 1$, we use perturbation theory to obtain the spectrum as

$$\lambda_{n,l} = n(n+1)\left[1 + \frac{4c^{-2}}{(2n-1)(2n+3)}\right] + \frac{l(l+1)c^{-2}}{2}\left[1 - \frac{1}{(2n-1)(2n+3)}\right] + O(c^{-3}). \tag{2.69}$$

The integer index n denotes the excitation with n nodes in the radial direction, while the index l denotes that with l nodes in the angular direction. The first excitation $\lambda_{0,1}$ is a dipole oscillation and has a small energy gap of $2J(n+1)d_\ell/r_0 \ll J$. Figure 2.8 shows the $(n,l) = (1,0)$ and $(2,0)$ modes, corresponding to the oscillations in the radius r_0 and the thickness a_0, respectively. Figure 2.9 shows high l modes at $n = 1$

and $n = 2$. Those modes have oscillations on the surfaces of the shell, with the two surfaces oscillating in phase ($n = 1$) or out of phase ($n = 2$).

2.4.3 Number-conserved basis

As we discussed in previous subsections, eigen states of the Bose-Hubbard Hamiltonian are also eigen states of the total number operator. Although the mean-field states well describe the condensate properties, they are not the true eigen states of the Bose-Hubbard Hamiltonian because they do not conserve the total number of particles. In general, the true ground state is hard to obtain analytically. In the deep lattice regime($J/U \ll 1$), however, tunneling terms can be treated perturbatively and hence the physical quantities of interest, such as the single-site number fluctuation and the condensate fraction, can be calculated in orders of J/U.

In this subsection, we begin by constructing the ground state for a homogeneous condensate in a fixed-number truncated basis, composed of superpositions of number states associated with the two neighboring Mott insulating states. Using this ground state, we find expressions for the boson density and the number fluctuations on each site, calculate the single-particle density matrix, and hence obtain the condensate fraction. These properties are identical to those of the pseudo-spin mean-field state. The correspondence justifies the mean-field approach. Our calculations also show that in describing the weak-tunneling condensate, using a truncated basis of occupation number is valid, i.e. that the error induced by truncation is of $\mathrm{O}(J/U)$.

Given a system of M sites, if N is a multiple of M ($N = nM$, where n is an integer), the ground state of the system is $A\,||n\rangle\rangle + \mathrm{O}(J/U)$, where $||n\rangle\rangle$ defined in Eq. (2.31) denotes the commensurate state, and the normalization constant A is equal to 1 up to order J/U. For this state, Δn_i^2 and f_c are both zero.

If $N = nM + M_1$, where n and M_1 are integers and $0 < M_1 < M$, the ground state of the system is

$$|\Psi\rangle = \sum_{\{\eta\}} \frac{C_{\{\eta\}}}{(n+1)^{M_1/2}} \hat{a}_{\eta_1}^\dagger \hat{a}_{\eta_2}^\dagger \cdots \hat{a}_{\eta_{M_1}}^\dagger \, ||n\rangle\rangle + \mathrm{O}(J/U), \tag{2.70}$$

where $\{\eta\} = \{\eta_1, \eta_2, \ldots, \eta_{M_1}\}$ is a set of distinct integers chosen from $\{1, 2, \ldots, M\}$, and $\sum_{\{\eta\}}$ denotes the sum over all combinatorial configurations. The leading term shown in $|\Psi\rangle$ lies in a sub-space spanned by all possible product states of M_1 single-site states with occupation number $n+1$ and $M - M_1$ single-site states with occupation number n; in the small tunneling regime, this truncation proves to be a sufficient approximation. The coefficients $C_{\{\eta\}}$ can be obtained by solving the Bose-Hubbard Hamiltonian, or equivalently obtained by minimizing the total energy under the normalization constraint $\sum_{\{\eta\}} \left|C_{\{\eta\}}\right|^2 = 1$.

Now we compute the elements of the density matrix from Eq.(2.70). For diagonal terms,

$$\begin{aligned}
\langle \hat{a}_i^\dagger \hat{a}_i \rangle &= \sum_{\{\eta\},\{\eta'\}} \frac{C^*_{\{\eta'\}} C_{\{\eta\}}}{(n+1)^{M_1}} \langle\langle n || (\prod_{j=1}^{M_1} \hat{a}_{\eta'_j}) \hat{a}_i^\dagger \hat{a}_i (\prod_{j=1}^{M_1} \hat{a}_{\eta_j}^\dagger) \, || n \rangle\rangle \\
&= \sum_{i \notin \{\eta\}} \left| C_{\{\eta\}} \right|^2 \langle \hat{a}_i^\dagger \hat{a}_i \rangle_i + \sum_{i \in \{\eta\}} \frac{\left| C_{\{\eta\}} \right|^2}{n+1} \langle \hat{a}_i \hat{a}_i^\dagger \hat{a}_i \hat{a}_i^\dagger \rangle_i \\
&= n \sum_{i \notin \{\eta\}} \left| C_{\{\eta\}} \right|^2 + (n+1) \sum_{i \in \{\eta\}} \left| C_{\{\eta\}} \right|^2 = n + \sum_{i \in \{\eta\}} \left| C_{\{\eta\}} \right|^2,
\end{aligned}$$

where $\langle \hat{a}_i^\dagger \hat{a}_i \rangle_i \equiv {}_i \langle n | \, \hat{a}_i^\dagger \hat{a}_i \, | n \rangle_i$. From symmetry, $\sum_{i \in \{\eta\}} \left| C_{\{\eta\}} \right|^2$ is independent of i but depends only on the number of terms in the sum. Considering the normalization condition, we find

$$\begin{aligned}
\sum_{i \in \{\eta\}} \left| C_{\{\eta\}} \right|^2 &= \frac{\#\text{ of terms in the sum } \sum_{i \in \{\eta\}}}{\#\text{ of terms in the sum } \sum \{\eta\}} = \begin{pmatrix} M-1 \\ M_1 - 1 \end{pmatrix} \Big/ \begin{pmatrix} M \\ M_1 \end{pmatrix} = \frac{M_1}{M} \\
\Rightarrow \langle \hat{a}_i^\dagger \hat{a}_i \rangle &= n + \frac{M_1}{M}.
\end{aligned}$$

To evaluate the number fluctuation of a single site, we need to calculate $\langle \hat{a}_i^\dagger \hat{a}_i \hat{a}_i^\dagger \hat{a}_i \rangle$. Similarly,

$$\begin{aligned}
\langle \hat{a}_i^\dagger \hat{a}_i \hat{a}_i^\dagger \hat{a}_i \rangle &= n^2 + (2n+1) \sum_{i \in \{\eta\}} \left| C_{\{\eta\}} \right|^2 = n^2 + (2n+1) \frac{M_1}{M} \\
\Rightarrow \quad \Delta n^2 &= \langle \hat{a}_i^\dagger \hat{a}_i \hat{a}_i^\dagger \hat{a}_i \rangle_i - \langle \hat{a}_i^\dagger \hat{a}_i \rangle_i^2 = \frac{M_1}{M} (1 - \frac{M_1}{M}).
\end{aligned}$$

For the off-diagonal terms,

$$\begin{aligned}
\langle \hat{a}_i^\dagger \hat{a}_j \rangle &= \sum_{\{\eta_2 \ldots \eta_{M_1}\}} \frac{C^*_{\{i,\eta_2 \ldots \eta_{M_1}\}} C_{\{j,\eta_2 \ldots \eta_{M_1}\}}}{(n+1)} \langle \hat{a}_i \hat{a}_i^\dagger \rangle_i \langle \hat{a}_j \hat{a}_j^\dagger \rangle_j \\
&= (n+1) \sum_{\{\eta_2 \ldots \eta_{M_1}\}} C^*_{\{i,\eta_2 \ldots \eta_{M_1}\}} C_{\{j,\eta_2 \ldots \eta_{M_1}\}},
\end{aligned}$$

where $\{\eta_2 \ldots \eta_{M_1}\}$ is a set of distinct integers chosen from $\{1, 2, \ldots, M\}$ excluding i and j, and $\sum_{\{\eta_2 \ldots \eta_{M_1}\}}$ denotes the sum over all combinatorial configurations. Because $C_{\{\eta\}}$ is determined by the energy cost of the corresponding state, the difference between $C_{\{i,\eta_2 \ldots \eta_{M_1}\}}$ and $C_{\{j,\eta_2 \ldots \eta_{M_1}\}}$ is estimated to be of order $1/M_1$, and hence vanishes in the thermodynamic limit. By considering symmetry and the normalization condition, we find

$$\langle \hat{a}_i^\dagger \hat{a}_j \rangle = (n+1) \sum_{\{\eta_2 \ldots \eta_{M_1}\}} \left| C_{\{i,\eta_2 \ldots \eta_{M_1}\}} \right|^2$$

$$
\begin{aligned}
&= (n+1)\frac{\#\text{ of terms in the sum } \sum_{\{\eta_2 \ldots \eta_{M_1}\}}}{\#\text{ of terms in the sum } \sum_{\{\eta\}}} \\
&= (n+1)\left(\begin{array}{c} M-2 \\ M_1-1 \end{array} \right) \Big/ \left(\begin{array}{c} M \\ M_1 \end{array} \right) = (n+1)\Delta n^2.
\end{aligned}
$$

Collecting the results as

$$
\begin{aligned}
\langle \hat{n} \rangle &= n + \frac{M_1}{M}, && (2.71) \\
\Delta n^2 &= \frac{M_1}{M}(1 - \frac{M_1}{M}), && (2.72) \\
f_c &= \frac{(n+1)(M_1/M)(1-M_1/M)}{n+M_1/M} = \frac{(n+1)\Delta n^2}{\langle \hat{n} \rangle}. && (2.73)
\end{aligned}
$$

At $M_1 = 0$ or $M_1 = M$, Δn^2 and f_c both vanish and the system is in the commensurate-filling Mott state $||n\rangle\rangle$ or $||n+1\rangle\rangle$. If $0 < M_1/M < 1$, Δn^2 and f_c are both non-zero and the system is hence a condensate with a one-particle state macroscopically occupied. By diagonalizing the one-particle density matrix, we show this state is the zero quasi-momentum state. In the position representation, the density matrix has all diagonal elements $x = n + M_1/M$ and all off-diagonal ones $y = (n+1)\Delta n^2$ and can be diagonalized by Fourier transformation:

$$
\begin{aligned}
\hat{\rho} &= (x-y)I + y\sum_{i,j} |i\rangle \langle j| \\
&= (x-y)\sum_k |k\rangle \langle k| + yM\,|k=0\rangle \langle k=0| \\
&= [x+(M-1)y]\,|k=0\rangle \langle k=0| + (x-y)\sum_{k\neq 0} |k\rangle \langle k| \qquad (2.74)
\end{aligned}
$$

Because M is much larger than 1, the $k = 0$ state has much larger occupation than all the other states, which are uniformly occupied in a small fraction. The condensate fraction of the system is given by $[x+(M-1)y]/N$.

We compare Eq. (2.71-2.73) with (2.49-2.51). By setting the chemical potential to the value which renders the expectation value of the total number of particles of the mean-field ground state equal to the total number of particles of the fixed-number ground state, we find the relation $\cos^2(\theta/2) = M_1/M$. This relationship equates the one-particle density matrix of the two states, thus showing that these two states exhibit the same one-particle properties of the condensate and justifying the usage of the mean-field state for calculational purposes. In the next two sections, we therefore use whichever representation of the condensate phase is most convenient. In addition, for either state, the condensate fraction is the ratio of the off-diagonal elements of the density matrix to the diagonal one; the former is proportional to the number fluctuations and

the latter is just the boson density. The off-diagonal elements are constant, reflecting a complete correlation within the entire system.

Finally, in the fixed-number state, the condensate fraction has its maximum value $(n+1)/(\sqrt{n+1}+\sqrt{n})^2$ when $M_1/M = \sqrt{n(n+1)}-n$ (the difference between n and the geometric mean of n and $n+1$). Compared to 100% BEC state in the shallow lattice limit, represented by Eq. (2.30), the condensate fraction in the deep lattice regime is less than 35% for all $n > 0$, the same as the mean-field result.

2.5 Radio-frequency (RF) spectroscopy

One effective probe of the structure of lattice bosons is the high-resolution microwave spectroscopy. In recent experiments, an external radio-frequency (RF) is applied to induce ^{87}Rb atoms to make hyperfine transitions from $|F = 1, m_F = -1\rangle$ state to $|F = 2, m_F = 1\rangle$ state [80, 38] or to $|F = 2, m_F = 0\rangle$ state [40]. In this section, we propose variants of the experiment of Ref. [38] in which the Mott-insulating shells with different occupation numbers have been resolved by analyzing the density-dependent clock shifts of the system. The resolution hinges on the energy differences of interaction among two atoms in the same hyperfine state versus in different hyperfine states.

In order to probe the condensate in the deep-lattice regime, we propose specific values of lattice parameters that would distinguish the spectrum of the Mott state and that of the condensate state in two ways. The first is that the former would have one resonant peak, but the latter would have two. The second is that the two peaks of the latter would be blue-shifted with respect to that of the former. The scales for the separation between the two peaks and the shift are of an order of a few Hz and we anticipate that they will be within experimental reach in the near future, providing an effective means to verify the existence of the condensed interlayers. By considering the effect of Goldstone modes and finite-temperature, we show that this signal is a signature of condensate order, and would be absent if the interlayers were a normal boson fluid of the same density.

Below, we begin with a discussion of our RF set-up applied to a homogeneous system and then use these results to derive the spectrum of the inhomogeneous system in the local-density approximation. We use numerical simulations where appropriate and also invoke Fermi's golden rule to analyze the RF spectra for a range of phase space. To summarize our findings: at zero-temperature, the Mott and condensate states can be clearly distinguished via their single- versus double-peak structures. For the set of proposed parameters, RF transitions into states containing Goldstone mode excitations (which are the low-energy excitations associate with the condensate) do not obscure the double-peak structure at zero temperature.

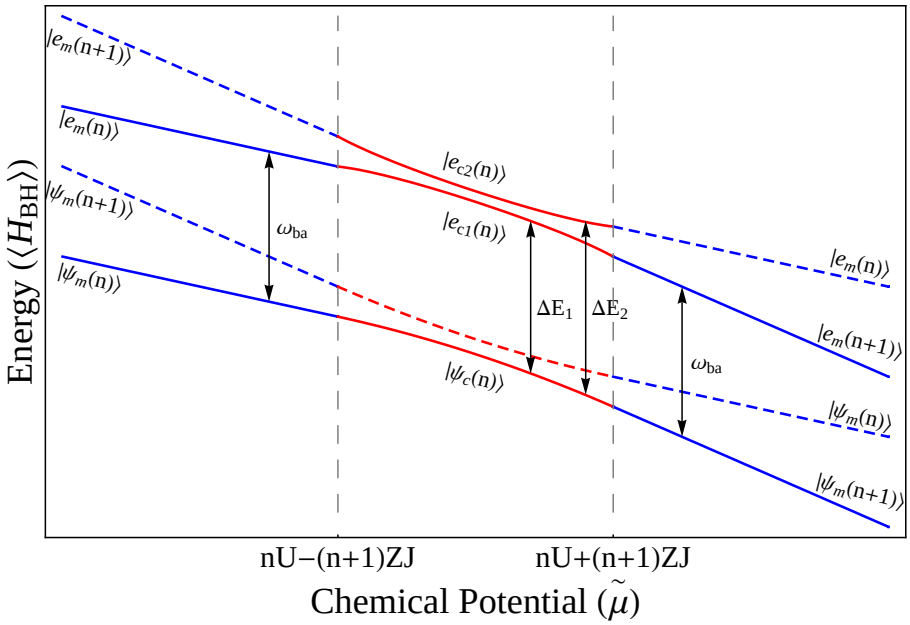

Figure 2.10: Energies of the lowest four single-site states of the 2-species Bose-Hubbard Hamiltonian. The corresponding states, which are defined in Eq. (2.76) and (2.78-2.80), are marked for each curve. Regions where the ground state of the system is a condensate (Mott-insulator) are marked red (blue). In each region, the ground state can make transitions to those higher energy states denoted with solid lines (with corresponding energy gaps marked by the black arrows), but is forbidden from transitions to those states marked with dashed lines.

However, at finite temperature, thermal excitations affect the two-peak structure. At very low temperatures ($k_BT \ll ZJ$), Goldstone modes lead to a temperature-dependent broadening of the peaks in the condensate signal. At higher temperatures ($k_BT \sim ZJ \ll U$), thermal fluctuations destroy the condensate order to yield a normal fluid; k_BT_c is of order ZJ [35, 81]. In this temperature regime, Goldstone modes completely obliterate the peaks, and extra structure develops at other characteristic frequencies corresponding to new allowed hyperfine transitions. At temperatures $k_BT > U$, the system displays large density fluctuations, even in the regions that are Mott-insulating at zero temperature, and the system loses signs of its quantum phases. Our analysis is thus limited to temperatures much less than the interparticle interaction, $U \sim k_B \times 10$ nK wherein, as a function of temperature, the resolution of the peaks in the RF spectrum tracks the condensate order and its ultimate destruction at T_c.

2.5.1 Zero-temperature RF spectrum

For a uniform system of two-state ($|a\rangle$ and $|b\rangle$) bosons, the Bose-Hubbard Hamiltonian contains two tunneling strengths (J_a and J_b), three interaction strengths (U_a, U_b, and U_{ab}), the chemical potential, and the single-particle energy difference between a and b particles (ω_{ba}). In the following, we consider a particular case:

$J_b = 0$, $U_b \gg U_a$, $U_{ab} = U_a$, and $\omega_{ba} \gg U_a$. This setting has two advantages. (1) Because $\omega_{ba} > 0$, the ground state of the system has all particles in the a hyperfine state but no particles in the b state. (2) Because $U_b \gg U_{ab} = U_a$, the energy gap between having two b particles on a site and having one b particle is much larger than that between having one b particle on a site and having no b particles. Therefore when the frequency of the RF field is of the order of the gap in the latter case, we can safely limit consideration to transitions to states with one b particle.

For the situation described above, the Bose-Hubbard Hamiltonian, including the upper hyperfine state, becomes

$$\begin{aligned}\hat{H}_{\mathrm{BH}} &= -J\sum_{<ij>}(\hat{a}_i^\dagger\hat{a}_j + \hat{a}_j^\dagger\hat{a}_i) \\ &\quad + \sum_i[\frac{U}{2}(\hat{n}_{ai}+\hat{n}_{bi})(\hat{n}_{ai}+\hat{n}_{bi}-1) - \mu(\hat{n}_{ai}+\hat{n}_{bi}) + \frac{U_b - U}{2}\hat{n}_{bi}(\hat{n}_{bi}-1) + \omega_{ba}\hat{n}_{bi}], \quad (2.75)\end{aligned}$$

where we drop the subscript a of J_a and U_a. In the deep lattice regime, we use the mean field approximation to analyze the RF spectrum of the system. The single-site Mott state with $\langle\hat{n}\rangle = n$ and the single-site condensate state with $n < \langle\hat{n}\rangle < n+1$ can be represented by

$$\begin{aligned}|\psi_m(n)\rangle &= |n\rangle \otimes |0\rangle \\ |\psi_c(n)\rangle &= \sin\frac{\theta}{2}|n\rangle\otimes|0\rangle + \cos\frac{\theta}{2}|n+1\rangle\otimes|0\rangle, \quad (2.76)\end{aligned}$$

where $|n_a\rangle \otimes |n_b\rangle$ represents a single-site state with n_a particles of hyperfine state a and n_b particles of hyperfine state b. As in Eq. (2.48) of Subsection 2.4.1, we have $\cos\theta = (\mu - nU)/[(n+1)ZJ]$ determining the angle between the pseudo-spin and the z-axis. Compared to Eq. (2.47), the symmetry-breaking phase ϕ has been set to zero for the decoupled-site analysis; the subsequent Goldstone mode analysis implicitly assumes that this phase has gradual variations from site to site.

The Hamiltonian describing the interaction between the bosons and an applied RF field is [28]

$$\mathcal{H}_{RF} = \sum_i \gamma(\hat{a}_i^\dagger\hat{b}_i + \hat{b}_i^\dagger\hat{a}_i)\cos\omega t, \quad (2.77)$$

where γ is proportional to the amplitude of the RF field and ω is its frequency; this Hamiltonian can be derived from the second-quantized form of the interaction $\int d\mathbf{r}\psi^\dagger\hat{\mu}\cdot\mathbf{B}\psi$.

We analyze the allowed transitions in different ranges of the chemical potential. We evaluate the transition amplitudes $A_t = \langle F|\sum_i\gamma(\hat{a}_i^\dagger\hat{b}_i + \hat{b}_i^\dagger\hat{a}_i)|I\rangle$ between allowed initial and final states $|I\rangle$ and $|F\rangle$, respectively,

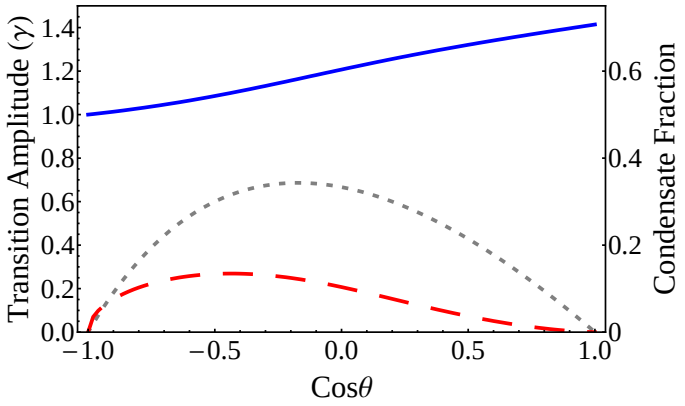

Figure 2.11: Absolute value of transition amplitude A_{1t} and A_{2t} (solid and dashed lines, respectively; axis on left-hand side of graph) and condensate fraction (dotted line; axis on right-hand side of graph) as a function of the value of the cosine of the pseudo-spin angle (corresponding to the density of bosons). The system is a uniform condensate whose number density satisfies $1 < \langle n \rangle < 2$.

and the energy gaps ΔE, given by the difference in the expectation values of the Bose-Hubbard Hamiltonian of Eq. (2.75) in the corresponding excited state and ground state. We plot the energy levels in Figure 2.10, which shows how the system at zero temperature undergoes quantum phase transitions through the n Mott state ($|\psi_m(n)\rangle$), the condensed state ($|\psi_c(n)\rangle$), and the $n+1$ Mott state ($|\psi_m(n+1)\rangle$) as the chemical potential is increased. The figure also shows possible excited states to which the ground state can make a transition in the presence of the RF field, and shows the energy gap between them. Details of the transitions for each range of the chemical potential in Figure 2.10 are discussed below.

When $[(n-1)U + nZJ] < \mu < [nU - (n+1)ZJ]$, the ground state is the n Mott state ($|\psi_m(n)\rangle$). We have only one possible excited state (denoted by $|e_m(n)\rangle$) to which the ground state can make a transition. The excited state, the transition amplitude A_t, and the energy gap ΔE are correspondingly

$$\begin{aligned} |e_m(n)\rangle &= |n-1\rangle \otimes |1\rangle \\ A_t &= \gamma\sqrt{n} \\ \Delta E &= \omega_{ba}. \end{aligned} \tag{2.78}$$

Because ΔE is independent of n, all the Mott states with different n have the same energy gap between the ground state and the excited state.

When $[nU - (n+1)ZJ] < \mu < [nU + (n+1)ZJ]$, the ground state is the condensate state $|\psi_c(n)\rangle$. We find two orthogonal excited states (denoted by $|e_{c1}(n)\rangle$ and $|e_{c2}(n)\rangle$) with non-zero transition amplitudes.

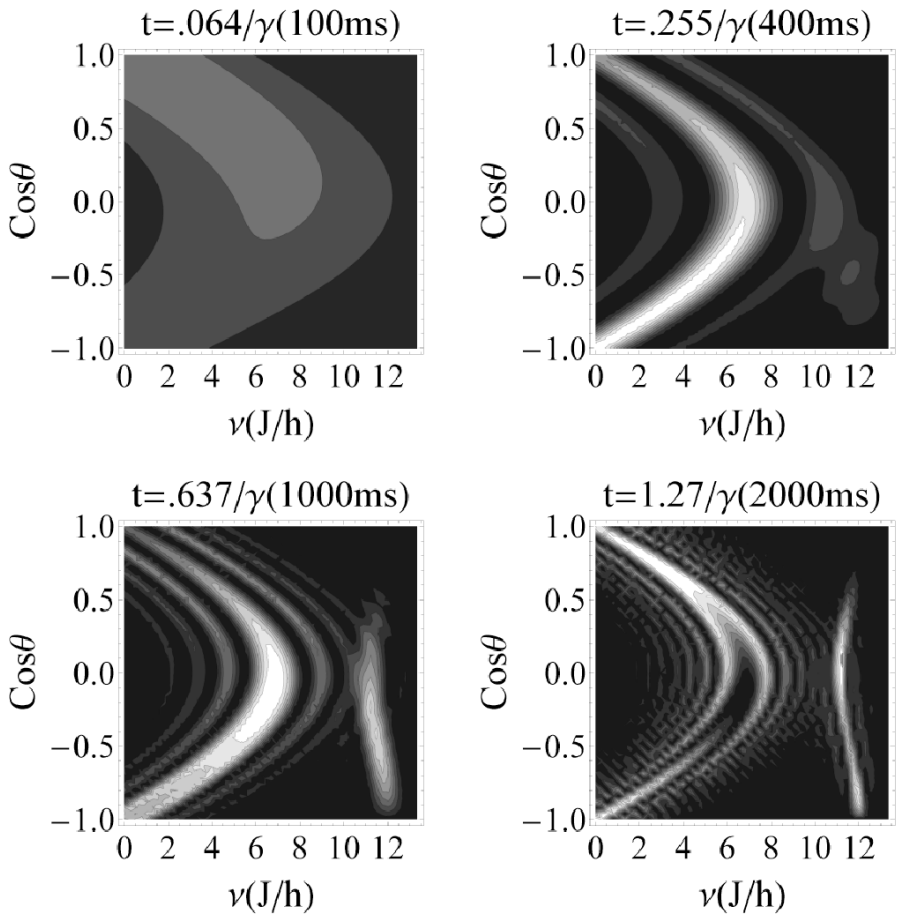

Figure 2.12: Fraction of bosons transferred to the higher hyperfine state for a uniform condensate with $1 < \langle n \rangle < 2$ at $t = 100$, 400, 1000, and 2000 ms. The horizontal axis is the detuning of the RF field with respect to the resonant frequency of the Mott-insulating state, while the vertical axis is $\cos\theta$. The color scale is bounded by 0 (black) and 1 (white) with contours separated by 0.1.

The first state, its corresponding transition amplitude A_{t1}, and energy gap ΔE_1 are

$$\begin{aligned} |e_{c1}(n)\rangle &= \sin\frac{\theta_1}{2}\,|n-1\rangle\otimes|1\rangle + \cos\frac{\theta_1}{2}\,|n\rangle\otimes|1\rangle\,, \\ A_{1t} &= \gamma(\sqrt{n}\sin\frac{\theta}{2}\sin\frac{\theta_1}{2} + \sqrt{n+1}\cos\frac{\theta}{2}\cos\frac{\theta_1}{2}), \\ \Delta E_1 &= \omega_{ba} + \frac{ZJ\sqrt{n+1}}{4}[\sqrt{n+1}(\sin^2\theta+2) - (\sqrt{n}\sin\theta\sin\theta_1 + 2\sqrt{n+1}\cos\theta\cos\theta_1)], \end{aligned} \quad (2.79)$$

where $|e_{c1}\rangle$ is taken to be the equilibrium state (the lowest energy state) of the Hamiltonian with the constraint $n_b = 1$ (*i.e.* in the $n_b = 1$ block). We calculate the parameter θ_1 by minimizing the energy of the system with site i in an excited state ($|e_{c1}(n)\rangle$) and all the other sites still in the ground state ($|\psi_c(n)\rangle$). As a result, we obtain a relation between θ_1 and θ, which is $\tan\theta_1 = \sqrt{n/(n+1)}\tan\theta$. The second excited

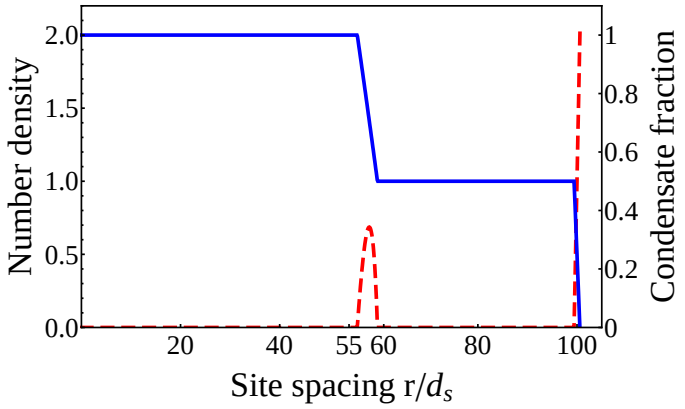

Figure 2.13: Number density profile (solid line; scale on left axis of graph) and condensate fraction (dashed line; scale on right axis of graph) of an inhomogeneous lattice boson system. From inner to outer of the system, the phases (thickness in lattice spacing d_ℓ) are the Mott-insulator (55), condensate (5), the Mott-insulator (38), and condensate (2).

state, corresponding transition amplitude A_{t2}, and energy gap ΔE_2 are

$$\begin{aligned} |e_{c2}(n)\rangle &= \cos\frac{\theta_1}{2}\,|n-1\rangle\otimes|1\rangle - \sin\frac{\theta_1}{2}\,|n\rangle\otimes|1\rangle\,, \\ A_{2t} &= \gamma(\sqrt{n}\sin\frac{\theta}{2}\cos\frac{\theta_1}{2} - \sqrt{n+1}\cos\frac{\theta}{2}\sin\frac{\theta_1}{2}), \\ \Delta E_2 &= \omega_{ba} + \frac{ZJ\sqrt{n+1}}{4}[\sqrt{n+1}(\sin^2\theta+2) + (\sqrt{n}\sin\theta\sin\theta_1 + 2\sqrt{n+1}\cos\theta\cos\theta_1)]. \end{aligned} \quad (2.80)$$

When the chemical potential in the condensed phase reaches its upper or lower bound ($\theta = 0$ or $\theta = \pi$), Eq.(2.79) becomes Eq.(2.78) with n or $n+1$ Mott states correspondingly, but the transition amplitude of Eq.(2.80) vanishes (Figure 2.12). However, the $n = 0$ condensate state is an exception since it can only make a transition to one excited state $|0\rangle\otimes|1\rangle$ with a transition amplitude $\gamma\cos\frac{\theta}{2}$ and an energy gap $(\omega_{ba} + JZ\sin^4\frac{\theta}{2})$. Thus, while the Mott state can only make a transition to one excited state, the condensate state can make transitions to two excited states.

As a consequence of these allowed transitions, the Mott state ought to have a single peak in the associated RF spectrum while the condensate ought to have two. This can be seen to first order (in number of particles transferred) by employing Fermi's golden rule (FGR), where the transition rate is given by [82]

$$I(\omega) = \frac{2\pi}{\hbar}\sum_{F,I}(\rho_I - \rho_F)\,|A_t|^2\,\delta\,(\omega - E_F + E_I)\,, \quad (2.81)$$

where $|I\rangle$ ($|F\rangle$) is the initial (final) state with energy E_I (E_F) and probability for occurrence ρ_I (ρ_F). Hence, FGR would predict a single delta function peak for the Mott state RF spectrum and two delta function peaks for the condensate.

We now confirm that the presence of the condensate does yield a two-peak RF spectrum by numerically time-evolving the equations of motion in the presence of the RF field. Taking into account both experimental feasibility and optimal conditions for observing the RF signatures of the condensate, we consider an experimentally feasible system containing $N = 5.11 \times 10^6$ ^{87}Rb atoms with $a_s = 5.32$ nm in a sphere whose radius is 53.2 μm, or 100 sites, long. The parameters of the optical lattice are $\lambda = 1.064$ μm and $V_0 = 20E_R$ and the frequency of the external harmonic trap is $\omega = 2\pi \times 6.13$ Hz. The system has an $n = 2$ Mott-insulating sphere, an $n = 1$ Mott-insulating shell, a condensate shell between the two Mott insulators, and a condensate shell on the outer boundary. The thickness of the condensate inter-layer is 2.66μm or 5 sites long, approximately 10 times thinner than the Mott-insulating regime. Figure 2.13 shows density profile and condensate fraction of the system. This setting corresponds to the values $U = 2\pi \times 306$ Hz, $J = 2\pi \times 0.898$ Hz (then $ZJ/U = 1.76 \times 10^{-2}$ is small compared to 1), and $\mu = 1.5U$. The intensity of the RF field is set such that $\gamma = 0.118ZJ = 2\pi \times 0.637$ Hz, which is of the same order as that in the experiment of Ref. [38]. If the RF field is turned on at $t = 0$, within the rotating-wave approximation, in which the largely detuned oscillating components of the RF field are ignored, we find that the fraction of transferred particles at the frequency of the second peak of the condensate's spectrum begins to rise at $t = 0.225/\gamma$ (400 ms), and that at any given time, the spectrum shows oscillatory behavior with respect to the detuning (Figure 2.12). In order to see a distinct second peak, we calculate the average fraction transferred between $t = 0.637/\gamma$ (1000 ms) and $t = 1.27/\gamma$ (2000 ms). Figure 2.14 shows the average fraction transferred for a uniform condensate. We can see two peaks whose positions agree with the energy gap in Eq. (2.79) and Eq. (2.80). Figure 2.15 shows the average fraction transferred for the entire inhomogeneous system. Because the fraction transferred in the Mott insulator is an even function of the detuning, we subtract the negative detuning part from the corresponding positive detuning part to eliminate the contribution of the Mott insulator. The result shows that there are two peaks of magnitude 1% (5×10^5 atoms transferred), and their positions agree with our theoretical analysis.

All calculations above rely on a mean-field approximation. As a minor check that number conservation and entanglement do not alter the proposed signatures, we performed the numerical toy simulation on time-evolving the entangled, fixed-number condensate state of 6 bosons in 4 sites in the presence of an RF field. For periodic boundary conditions, the ground state of the system is given by

$$\frac{\sqrt{2}}{4}(|1\rangle|1\rangle|2\rangle|2\rangle + |1\rangle|2\rangle|2\rangle|1\rangle + |2\rangle|2\rangle|1\rangle|1\rangle + |2\rangle|1\rangle|1\rangle|2\rangle) + \frac{1}{2}(|1\rangle|2\rangle|1\rangle|2\rangle + |2\rangle|1\rangle|2\rangle|1\rangle) + \mathcal{O}(\frac{J}{U}), \tag{2.82}$$

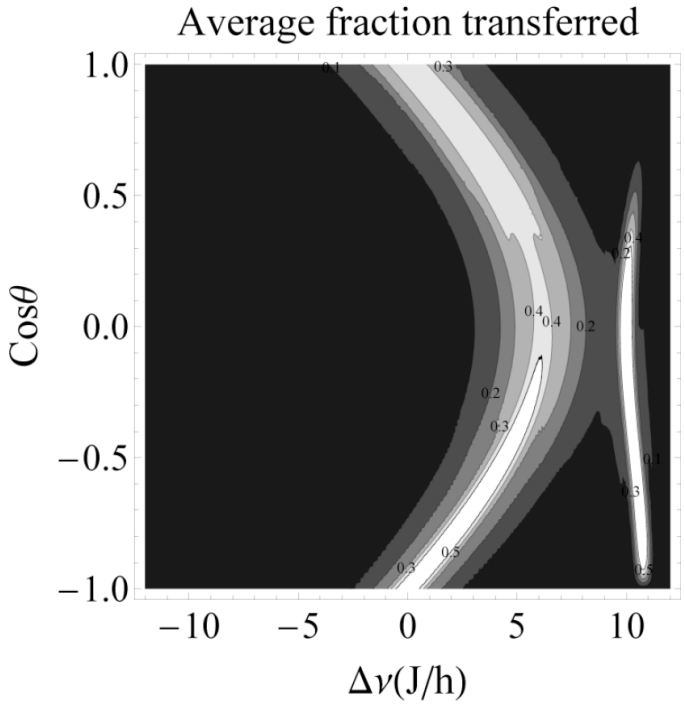

Figure 2.14: Average fraction of bosons transferred between $t = 1000$ and 2000 ms. Contour interval is 0.1. The first peak appears in the range of 0 to $7J$ (6.29 Hz), and the second peak appears at about $11.5J$ (10.3 Hz). When $\cos\theta = \pm 1$, we recover the Mott signature.

where $|n_1\rangle\,|n_2\rangle\,|n_3\rangle\,|n_4\rangle$ means the state with the ith site occupied by n_i bosons. The ground state has non-zero single-site number fluctuations, which differentiate the condensate from the Mott insulator. Thus the system is expected to have an RF spectrum similar to that of a many-particle condensate. We use the Bose-Hubbard Hamiltonian, plus time-dependent terms which represent the interaction with the RF field, to numerically time-evolve the ground state, and compute the average number of bosons transferred from the a state to the b state(Figure 2.16). The results show the same signatures as those of the mean-field approach: 2 peaks with positive shifts of order J, thus providing some confidence that our result is not an artifact of the mean-field approximation.

To ensure that no spurious effects emerge from truncating the Hilbert space, we have analyzed the effect of the leading subdominant states $|n-1\rangle \otimes |0\rangle$ and $|n+2\rangle \otimes |0\rangle$. Within the resultant four-state truncated space, we obtain four possible final states. Two of them have the same energy shifts (of order J) and transition amplitudes (of order γ) as those obtained in the two-state truncated space, plus small corrections of order J/U; these corrections contribute a fraction $(J/U)^2$ to the number transferred. The other two final states have energy shifts of order U ($\gg J$) and transition amplitudes of order $\gamma J/U$ ($\ll \gamma$), which also contributes a fraction $(J/U)^2$ to the number transferred. The minimal change coming from taking into account these additional states justifies our usage of the two-state truncation in the deep lattice regime.

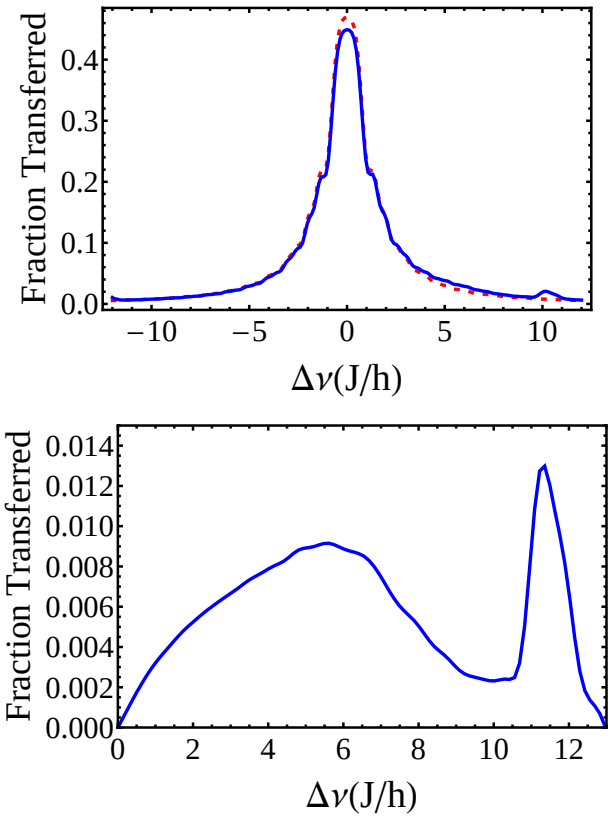

Figure 2.15: Average fraction of bosons transferred between $t = 1000$ ms and 2000 ms for the inhomogeneous system defined in Figure 2.13. Top: the system with both Mott-insulator and condensate regions (solid) compared with that having only Mott-insulator regions (dotted). Bottom: spectrum of the condensate shells after eliminating the contribution from the Mott -insulator shells. The results show that two peaks with positive shifts are signatures of condensate order in a deep optical lattice.

2.5.2 Goldstone modes and finite-temperature effects

At finite temperature, the thermally-occupied excited states of the system will affect the RF spectrum. When the temperature is much smaller than the interaction energy ($k_B T \ll U$), the Mott state has negligible thermal effects because it has an excitation gap of order U [28, 85, 84]. However, we should be concerned that the two-peak signature of the condensate may be destroyed at low temperatures by Goldstone modes associated with the continuous symmetry-breaking in the phase ϕ of the condensate ground state wave function. Each Goldstone mode/boson corresponds to a long-wavelength distortion of the density and phase between neighboring sites and the modes form the gapless low-energy excitation spectrum for the condensate. The structure of these modes for one-species system has been derived from the pseudo-spin formulation and analyzed for homogeneous and inhomogeneous systems in Section 2.4. In order to be self-contained, we present the Goldstone mode description here for the homogeneous generalized case of the two-species system

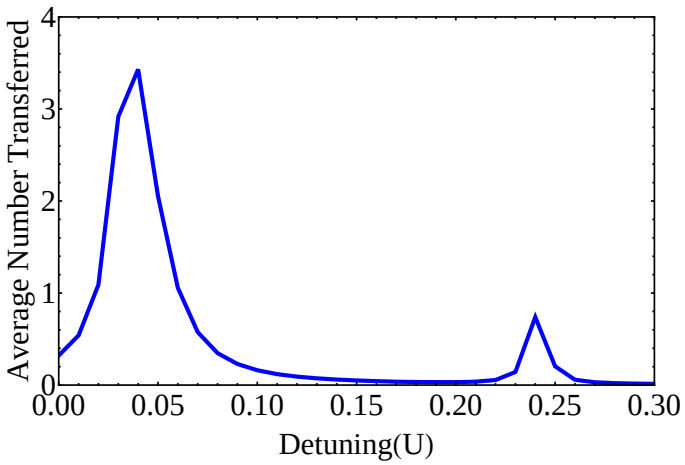

Figure 2.16: Average fraction transferred of a 6-boson 4-site entangled state driven by the external RF field. The parameters are $U_a = U_{ab} = 1$, $ZJ = 0.05$, $\mu = 1.5$, and $U_b = \omega_{ba} = 5$. We can see the spectrum has 2 peaks with positive shifts of order J.

of interest.

We describe the system by the mean-field site-decoupled state in the RF transition process. Up to leading order in J/U, each single-site state is represented within a truncated basis of 4 vectors, $|n\rangle \otimes |0\rangle$, $|n+1\rangle \otimes |0\rangle$, $|n\rangle \otimes |1\rangle$, and $|n+1\rangle \otimes |1\rangle$, where we use the notation $|n_a + n_b, n_b\rangle$. As each number has only two possible values in the truncated bases, we use the pseudo-spin language and map these states onto the states of 2 spin-1/2 pseudo-spins as $|\downarrow\rangle \otimes |\downarrow_b\rangle$, $|\uparrow\rangle \otimes |\downarrow_b\rangle$, $|\downarrow\rangle \otimes |\uparrow_b\rangle$, and $|\uparrow\rangle \otimes |\uparrow_b\rangle$ respectively. Consistent with this mapping of the basis, any operator in the Bose-Hubbard Hamiltonian of Eq.(2.75) can be replaced by its corresponding spin operator as long as they have the same matrix representation in the truncated space. Therefore we have the correspondence

$$\begin{aligned} \hat{n}_a + \hat{n}_b &\rightarrow n + \frac{1}{2} + \hat{S}^z \\ \hat{n}_b &\rightarrow \frac{1}{2} + \hat{S}^z_b \\ \hat{a} &\rightarrow \sqrt{n + 1/2 - \hat{S}^z_b}\,\hat{S}^- \\ \hat{b}^\dagger \hat{a} &\rightarrow \sqrt{n + 1/2 + \hat{S}^z}\,\hat{S}^+_b, \end{aligned} \tag{2.83}$$

With these substitutions, we obtain the pseudo-spin Hamiltonian for the 2-species Bose-Hubbard Hamiltonian of Eq.(2.75), up to a constant:

$$\hat{H}_{\rm PS} = -J \sum_{\langle ij \rangle} \sqrt{n + 1/2 - \hat{S}^z_{bi}} \sqrt{n + 1/2 - \hat{S}^z_{bj}} \left(\hat{S}^x_i \hat{S}^x_j + \hat{S}^y_i \hat{S}^y_j \right) + \sum_i \left[(Un - \mu) \hat{S}^z_i + \omega_b \hat{S}^z_{bi} \right]. \tag{2.84}$$

This Hamiltonian describes a system with two spins ($\hat{\mathbf{S}}$ and $\hat{\mathbf{S}}_\mathbf{b}$) on each site, each of which responds to an independent external "magnetic field" in the z-direction. The interaction between transverse components of adjacent $\hat{\mathbf{S}}$ spins has a strength related to the z- components of the b spins on those sites. When $S^z_{bi} = -1/2$, which corresponds to having no particles in the b hyperfine state, $\hat{H}_{\rm PS}$ becomes the pseudo-spin approximation to the single-species Bose-Hubbard model of Eq.(2.46). The ground state of $\hat{H}_{\rm PS}$ is the same as Eq.(2.76), when written in the corresponding spin basis.

As we discussed in Subsection 2.4.1, the equivalence of the matrix representations of the Bose-Hubbard Hamiltonian and the pseudo-spin Hamiltonian imply that they also have the same excitations in the truncated space. Moreover, the Goldstone excitations of the pseudo-spin model, the spin waves, are equivalent to those of the Bose-Hubbard model, which are small density and phase distortion over a long length scale. To obtain the dispersion relations of the spin waves for $\hat{\mathbf{S}}$ and $\hat{\mathbf{S}}_\mathbf{b}$, we introduce two species of Holstein-Primakoff bosons ($\hat{A}$ and $\hat{B}$) to represent small fluctuations of the corresponding spins around their equilibrium value at zero temperature. Provided the fluctuations are sufficiently small such that all terms higher than quadratic can be neglected, the spin operators can be represented as

$$\begin{aligned}
\hat{\mathbf{S}} &= (\frac{\cos\theta}{2}(\hat{A}+\hat{A}^\dagger) + \sin\theta(\frac{1}{2} - \hat{A}^\dagger\hat{A}), \frac{i}{2}(\hat{A}+\hat{A}^\dagger), -\frac{\sin\theta}{2}(\hat{A}+\hat{A}^\dagger) + \cos\theta(\frac{1}{2} - \hat{A}^\dagger\hat{A})) \\
\hat{\mathbf{S}}_b &= (-\frac{1}{2}(\hat{B}+\hat{B}^\dagger), \frac{i}{2}(-\hat{B}+\hat{B}^\dagger), -\frac{1}{2} + \hat{B}^\dagger\hat{B}).
\end{aligned} \tag{2.85}$$

After substituting these into the pseudo-spin Hamiltonian and keeping terms up to quadratic order in the Holstein-Primakoff bosons, we Fourier transform the resulting Hamiltonian into momentum space, and perform a Bogoliubov transformation on the A bosons into α bosons ($\hat{A}_p = u_p\hat{\alpha}_p + v_p\hat{\alpha}^\dagger_{-p}$) to diagonalize the $\hat{A}$ terms. Thus we arrive at the diagonalized Hamiltonian:

$$\hat{H}_{\rm PS} = \sum_{p=-\pi/d_\ell}^{\pi/d_\ell} \epsilon_p\alpha^\dagger_p\alpha_p + \omega_B\hat{B}^\dagger_p\hat{B}_p, \tag{2.86}$$

where p is the lattice momentum and l the lattice spacing. The B terms correspond to the creation of a B boson with momentum p, while the α_p operator creates a Goldstone excitation in the condensate with momentum p. The excitation energy of the α excitations is the same as Eq. (2.57), which is not gapped. The excitation energy of of the B particles is

$$\omega_B = \omega_{ba} + (1/8)ZJ\sin\theta, \tag{2.87}$$

which is independent of p. This excitation is gapped (reflecting the fact that the b bosons are in their com-

mensurate state) and therefore should not be present in the initial state in RF transitions for temperatures $kT \ll \hbar\omega_{ba}$, which we assume throughout.

Turning to the role of the Goldstone modes in RF transitions, the form of the RF perturbation (given in the position basis of the physical particles as $\sum_i \gamma \hat{a}_i^\dagger \hat{b}_i + h.c.$) is given in the Goldstone basis by

$$H_{RF} = \quad - \quad \sqrt{N}\gamma \hat{B}_0^\dagger + \frac{\gamma \sin\theta}{4\sqrt{\bar{n}}} \sum_p [(v_p + u_p)\hat{B}_p^\dagger(\alpha_p + \alpha_{-p}^\dagger) + \text{h.c.}], \tag{2.88}$$

where N is the total number of particles and $\bar{n} = n + \cos^2(\theta/2)$ is the number density at zero temperature. The first term creates a B boson uniformly in space without any distortions in density or phase (which are represented by α bosons). The second term creates a B boson with momentum p accompanied by an α boson with momentum $-p$ or annihilation of an α boson with momentum p.

For the 3D system at zero temperature, the initial state consists of the ground state of the system purely comprised of a particles, and thus no Goldstone modes are excited. Under an RF field however, a small number of particles change their internal state to b. If this change is not uniform in space, it will be accompanied by Goldstone modes. Assuming that N_G is the total number of Goldstone bosons excited by the RF field, we can estimate the final state energy of a single site, which differs from that of the $N_G = 0$ case, as $(N_G/M)ZJ$, where M is the total number of sites and ZJ is the energy scale of the Goldstone mode spectrum. If the RF field is weak enough that the average number of excited Goldstone bosons per site (N_G/M) is much smaller than one, the change of the single-site energy gap is much smaller than ZJ, which is about the distance between the two peaks obtained in the last sebsection. In typical experimental settings, this indeed is the case given that about 10% of the particles make transitions to the b state. Therefore, exciting Goldstone modes at zero temperature ought not obscure the 2-peak signature.

We explicitly show that these modes provide a small background which still leaves the two-peak signature robust by using the above Goldstone representation of the RF perturbation in Fermi's golden rule of Eq. (2.81). We find the transition rate due to the first term of Eq. (2.81) is $I^{(1)}(\omega) \propto \delta(\omega - \omega_B)$. This delta peak corresponds to the first peak we obtained in Subsection 2.5.1, though slightly shifted given the slightly different mean-field energy estimates. The transition rate due to the second term is $I^{(2)}(\omega) \propto \sin^2\theta|\omega - \omega_B|^3$ which is so small compared to the delta function near ω_B that the effect of $I^{(2)}$ on the contrast of $I^{(1)}$ can be ignored. We expect similar argument to hold for the second peak obtained in Subsection 2.5.1. Therefore, we find that excitation of Goldstone modes by a weak RF field will not obscure the two-peak signature at zero temperature.

At low temperatures of order $kT \ll ZJ$, the initial state still contains zero B bosons but does con-

tain α bosons, or thermally-excited Goldstone modes, which reduces the condensate density. Taking these thermally-excited α bosons into consideration in the RF signal, we find that $I^{(1)}$ is still a delta peak, while $I^{(2)}$ becomes a finite function of $|\omega - \omega_B|$ which does not obscure the peak $I^{(1)}$. As a result, we expect a slight reduction in the height of the two peaks and a slightly larger contribution to the background. Nevertheless, for three-dimensional systems, we expect the two-peak condensate signature to persist at these temperatures.

Close to the critical temperature $kT_c \approx ZJ$, the average number of α bosons per site is of order 1 or more and the higher order terms in H_{RF} cannot be ignored. At this temperature regime, we also expect the average thermal expectation value $\sum_j \langle a_j \rangle / N$ of the order parameter to vanish, corresponding to destruction of long-range order in the system. Within the decoupled-site mean field approximation, $\langle a_i \rangle$ fluctuates in magnitude and phase from site to site. The kinetic part of the mean-field energy in the Bose-Hubbard Hamiltonian can thus be thought of as having a spread of order $(n+1)ZJ$. Given that the two low-temperature peaks in the RF spectrum are also separated by about $(n+1)ZJ$, we predict that the two peaks merge into a continuum around the critical temperature. In two-dimensions, even the smallest temperature suffices for the Goldstone modes to destroy true long-range order and we believe that this will be reflected in the smearing out of the two-peak structure for low-dimensional systems.

For the inhomogeneous shell situation, the Goldstone modes become quantized due to confinement (see Subsection 2.4.2). The essential issue is whether the quantized modes along each direction which are accessible at temperature T are numerous enough to form an effective continuum. Modifying the arguments above to include these inhomogeneous effects, we deduce that the two peak structure would remain at low temperatures for a condensate shell with a thickness of several lattice sites.

Finally, in this section we argue that the presence of condensate order can be detected in a two-peak RF spectrum for appropriate RF parameter settings in contrast to the one-peak structure of the Mott phase. Our results also suggest that when the condensate becomes a normal fluid at $T = T_c$, the two-peak structure is washed out. Our arguments can be made more rigorous by way of numerical simulations such as those of the previous subsection that would include the Goldstone modes and finite temperature effects; such a treatment is for the future study.

2.6 Matter-wave interference

Experimental observation of matter-wave interference peaks in absorption images have provided striking evidence for BEC states in shallow optical lattices [20]. In addition, the concentric Mott shell system

has been observed to preserve finite visibility in the interference pattern [86, 87]. Characteristics of the interference patterns have been analytically and numerically studied under several specific conditions for normal fluid, BEC and Mott insulating phases in the lattice boson system [88, 54, 89, 90]. Here, we consider bosons in the deep lattice regime and ask what signatures of matter-wave interference can distinguish the presence of a condensate shell between two Mott-insulating shells. We work at zero temperature, which should be valid for temperatures $kT \ll J$, where one would expect the contrast between these states to be strongest. We begin by considering a homogeneous system, where the many-body wavefunctions of the Mott and deep-lattice condensate phases can be exactly time-evolved to obtain the density profile measured by absorption imaging. For simplicity, we ignore the effect of interaction during time-of-flight [88], which is expected to quantitatively influence the intensity and width of peaks but preserve the qualitative signatures of the interference pattern [89]. By calculating the time-evolution of a system of bosons on a ring lattice, we show that condensate states will have sharp interference maxima, in contrast to Mott states, after free expansion of the system. To illustrate how these features would be displayed in an inhomogeneous system, we also the time-evolve a system of concentric ring lattices that have a Mott-condensate-Mott structure and point to signatures of the condensate in the time-evolved profiles.

2.6.1 Density profile upon expansion

For the commensurate state $||n\rangle\rangle$, the many-body wave function is a product of N single-particle wave functions:

$$\begin{aligned}\Psi(\mathbf{r}_1,\ldots,\mathbf{r}_N) &\equiv \langle \mathbf{r}_1,\ldots,\mathbf{r}_N \mid |n\rangle\rangle \\ &= A \sum_{\mathrm{sym}\{\mathbf{r}\}} \prod_{i=1}^{N} \psi(\mathbf{r}_i - \mathbf{s}^{(i)}) \\ &= A \sum_{\{\mathbf{s}\}} \prod_{i=1}^{N} \psi(\mathbf{r}_i - \mathbf{s}^{(i)}), \end{aligned} \tag{2.89}$$

where $\psi(\mathbf{r}_i - \mathbf{s}^{(i)})$ is the single particle wave function of particle i localized on a site at position $\mathbf{s}^{(i)}$, and A is a normalization constant. To satisfy Bose-Einstein statistics, we need to symmetrize all N degrees of freedom; this symmetrization (denoted by $\sum \mathrm{sym}\{\mathbf{r}\}$) is equivalent to the sum over all configurations of $\{\mathbf{s}^{(i)}\}$ (denoted by $\sum_{\{\mathbf{s}\}}$), which are permutations of $\{\underbrace{\mathbf{s}_1,\ldots,\mathbf{s}_1}_{n},\underbrace{\mathbf{s}_2,\ldots,\mathbf{s}_2}_{n},\ldots\underbrace{\mathbf{s}_M,\ldots,\mathbf{s}_M}_{n}\}$, where $\mathbf{s}_j$ is the position of site j.

Near the center of a lattice site, the lattice potential can be approximated as harmonic with frequency $\omega = \sqrt{4V_0 E_R}/\hbar$, where V_0 is the depth of the optical lattice and E_R is the recoil energy. The single-particle

wave function can thus be approximated as a harmonic oscillator ground state wave function well-localized on a site. If we ignore interactions (valid at low density), after turning off the lattice potential and the trap potential all single-particle wave functions are time-evolved by the free particle Hamiltonian $\hat{\mathbf{p}}^2/2m$. The wave function at later times is then given by

$$\psi_t(\mathbf{r}_i - \mathbf{s}^{(i)}) = \left(\frac{2l^2}{\pi}\right)^{d/4} \frac{\exp[-(\mathbf{r}_i - \mathbf{s}^{(i)})^2/(l^2 + 2i\hbar t/m)]}{(l^2 + 2i\hbar t/m)^{d/2}}, \tag{2.90}$$

where d is the dimensionality of the system, and l is the characteristic length of the single-particle wave function. The density profile as a function of position and time is obtained by calculating the diagonal elements of the single-particle density matrix.

$$\begin{aligned} \rho(r,t) &\equiv N \int \Psi_t^*(\mathbf{r}, \mathbf{r}_2, \ldots, \mathbf{r}_N)\Psi_t(\mathbf{r}, \mathbf{r}_2, \ldots, \mathbf{r}_N) d\mathbf{r}_2 \ldots d\mathbf{r}_N \\ &= N\,|A|^2 \sum_{\{\mathbf{s}\}} \sum_{\{\mathbf{s}'\}} \psi_t^*(\mathbf{r} - \mathbf{s}^{(1)})\psi_t(\mathbf{r} - \mathbf{s}'^{(1)}) \exp[-\sum_{i=2}^{N} (\mathbf{s}^{(i)} - \mathbf{s}'^{(i)})^2/(2l^2)]. \end{aligned} \tag{2.91}$$

For the condensate state $|\Psi\rangle$ of Eq.(2.70), the density profile $\rho_c(\mathbf{r}, \mathbf{t})$ is given by

$$\rho_c = N\,|A|^2 \sum_{\{\eta\}} \sum_{\{\eta'\}} C^*_{\{\eta'\}} C_{\{\eta\}} \{ \sum_{\{\mathbf{s};\{\eta\}\}} \sum_{\{\mathbf{s}';\{\eta'\}\}} \psi_t^*(\mathbf{r} - \mathbf{s}^{(1)})\psi_t(\mathbf{r} - \mathbf{s}'^{(1)}) \exp[-\sum_{i=2}^{N} (\mathbf{s}^{(i)} - \mathbf{s}'^{(i)})^2/(2l^2)]\}, \tag{2.92}$$

where $\sum_{\{\eta\}}$ denotes the same sum in Eq. (2.70), and $\sum_{\{\mathbf{s};\{\eta\}\}}$ denotes the sum over all $\{\mathbf{s}^{(i)}\}$ with a specific $\{\eta\}$; $\{\mathbf{s}^{(i)}\}$ are permutations of the set including $n+1$ each $\mathbf{s}_{\eta_i}$ of the sites $\eta_1, \ldots, \eta_{M_1}$ and n each $\mathbf{s}_j$ of the other sites. If $M_1 = 0$ or $M_1 = M$, $\{\eta\}$ has only one configuration, and hence Eq. (2.92) becomes Eq. (2.91).

2.6.2 Example: expansion of bosons in a ring lattice

As a concrete case that shows how sharp interference peaks emerge upon release and expansion of the condensate, we consider the illustrative example of bosons in a one-dimensional lattice of sites located on a ring of radius s in a two dimensional plane. Because of the symmetry of the ring, constructive interference is expected at its center. We therefore calculate the center density contributed by one particle, defined as $\tilde{\rho}(t) \equiv \rho(0,t)/N$. The result is

$$\tilde{\rho}(t) = F \left(\frac{2l^2}{\pi}\right)^{d/2} \frac{\exp[-2s^2 l^2/(l^4 + 4\hbar^2 t^2/m^2)]}{(l^4 + 4\hbar^2 t^2/m^2)^{d/2}}, \tag{2.93}$$

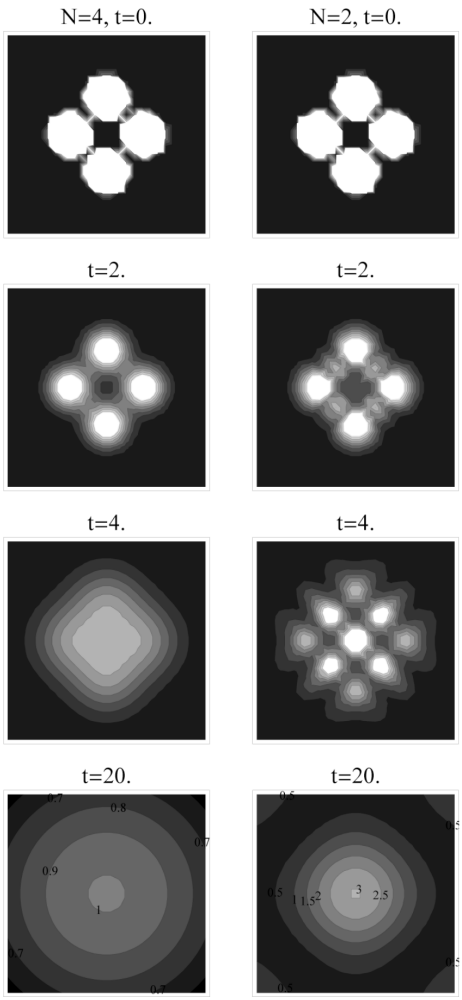

Figure 2.17: Matter wave interference patterns (per particle contribution). The left column is the 4-particle 4-site Mott insulator, and the right one is the 2-particle 4-site condensate. The four rows from top to bottom are at $t = 0$, 2, 4, and 20 time units$(ml^2/2\hbar)$. All parts of the figure have the same spatial scale. The number in the last row is the relative value of the density.

where $d = 2$ for this system and F is equal to

$$F_M = |A|^2 \sum_{\{\mathbf{s}\}} \sum_{\{\mathbf{s}'\}} \exp[-\sum_{i=2}^{N} (\mathbf{s}^{(i)} - \mathbf{s}'^{(i)})^2/(2l^2)] \tag{2.94}$$

for the Mott state and

$$F_c = |A|^2 \sum_{\{\eta\}} \sum_{\{\eta'\}} C^*_{\{\eta'\}} C_{\{\eta\}} \{ \sum_{\{\mathbf{s};\{\eta\}\}} \sum_{\{\mathbf{s}';\{\eta'\}\}} \exp[-\sum_{i=2}^{N} (\mathbf{s}^{(i)} - \mathbf{s}'^{(i)})^2/(2l^2)] \} \tag{2.95}$$

for the condensate. If $s \gg l$, $\tilde{\rho}(t)$ has a maximum at

$$t_m = mls/\sqrt{d}\hbar \tag{2.96}$$

and a half width $\Delta t = 2^{1/d} mls/\hbar$. While t_m indicates the time it takes matter waves to disperse from the ring to the center, Δt measures the duration of constructive interference processes. Eq. (2.96) is of the same form as a continuum BEC confined to a shell geometry with the characteristic length l given by the thickness of the shell [91]. The terms with $\{\eta'\} = \{\eta\}$ in the sum for F are the same for the Mott and condensate states. However, F for the condensate state has many additional terms with $\{\eta'\} \neq \{\eta\}$ that contribute to the center density which are not present in F_M. Therefore, we see that the center density of the condensate state has a much sharper peak than that of the Mott state. At finite temperature, the interference pattern is the thermal average over the densities of all possible pure states. The coefficients $C_{\{\eta\}}$ of higher energy states are not necessarily real and positive and thus would decrease the value of F given that not all terms give positive contributions. Therefore, we expect that the interference pattern of a condensate becomes more blurred with increasing temperature.

Although here we have only analytically solved for the density at the center of the ring, constructive interference patterns will occur throughout space after the system is released from its ring trap. The differences in these spatial patterns between initial Mott and initial condensed states gives further evidence for condensate order. As a toy example that exhibits these patterns, we numerically simulated the expansion processes of a 4-site Mott insulator of $|1\rangle|1\rangle|1\rangle|1\rangle$ and a 4-site condensate of Eq. (2.82) in the ring geometry and display the results in Figure 2.17. Both cases have the same initial density profile but have very different interference patterns in expansion. The condensate shows more interference peaks and has a much higher density in the center at long times than the Mott insulator does. This difference is similar to the difference between the phase-coherent state (BEC) and the phase-incoherent state (the Mott insulator) in the experiment of Ref. [20]. Although the initial density profiles of the two cases look the same, their interference patterns behave quite differently during the expansion process.

2.6.3 Inhomogeneous systems

The above discussions show how homogeneous systems of condensate and Mott insulator display different patterns upon release and expansion and that interference is a signature of condensate order in the system. To illustrate how these signatures can be used to probe condensate order realistic experimental situations, we consider a simplified inhomogeneous system of ^{87}Rb atoms displaying the nested, or "wedding-cake",

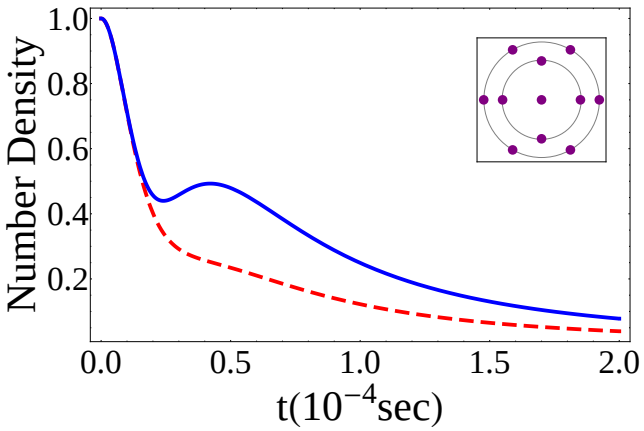

Figure 2.18: Density at the center point, as a function of time, during expansion of the system. The inset shows the geometry and the site positions of the model. The solid curve corresponds to the system that has a center site and an outer ring in Mott-insulating states and the inner ring in the condensate state. The dashed curve corresponds to the control system with the inner ring also in the Mott insulating state. The vertical axis is the relative density with respect to the initial value. The peak and the relatively large value at long times are evidence of the condensate part of the system.

structure of bosons in optical lattices in the presence of a harmonic trap. Building on the results of the previous subsection for bosons on a ring lattice, we model a two-dimensional system made up of a center point and two concentric rings, where the central site is in the $n = 2$ Mott insulating state, the 4 sites in the inner ring are in the $\langle n \rangle = 1.5$ condensate state, and 6 sites in the outer ring are in the $n = 1$ Mott insulating state. Site spacings of the two rings are both $d_\ell = 0.532$ μm. For the lattice depth $V_0 = 20E_R$, the characteristic length of the initial single-particle wave function is $l = 0.283 d_\ell$. If the lattice potential is turned off at $t = 0$, the density at the center point as a function of time shows a peak at $t = 4.2 \times 10^{-5}$ s (Figure 2.18). Compared to a control system where the inner ring has Mott states of the same density (2 sites in $n = 2$ and 2 sites in $n = 1$), the peak and the larger long-time residual density in the center indicate large constructive interference due to the condensate part of the system. Considering expansion of a 3d inhomogeneous system of Figure 2.13, we expect to observe a density peak in the center of the sphere at $t = 3.67$ ms, which is about 1/4 the duration of the time of flight in the experiment of Ref. [20]. We expect that such a time-evolved density profile should also be able to discern the presence of condensate interlayers for larger systems with realistic numbers of bosons.

In summary, we obtain interference signatures of a thin condensate inter-layer between two Mott insulator layers. For a toy system exhibiting concentric co-existent phases, we show that the condensed phase contributes a sharp peak to the time-evolved central particle density. As performed for single phases, simulations of realistic inhomogeneous large-sized three-dimensional systems within our truncated wavefunction basis and extraction of measurable quantities, such as the visibility, are in order; we believe that our results

here are indicative of the signatures of the condensate layer that would be obtained in actual systems.

2.7 Discussion and outlook

In this section, we discuss several open issues associated with our research on BEC in deep lattices. First we review recent studies on validity of local density approximation (LDA) and conclude that the LDA-predicted BEC regions are still robust in a real inhomogeneous system. We give a physical interpretation of the two-peak radio-frequency (RF) spectrum of the BEC phase, which implies the BEC is a two-component fluid. We discuss possible reasons that the two-peak signature for the BEC has not been observed in experiments. We discuss factors in the time-of-flight (TOF) experiments that are yet to be considered in our theoretical model. Finally we present future directions following the Bose-Hubbard study in this chapter.

The basic idea of LDA is to treat an inhomogeneous system as locally uniform enough such that the local properties are the same as those in the corresponding uniform system. The true local properties must differ from the LDA results due to the inhomogeneity, with the deviation depending on how locally uniform the system is. It is expected that LDA does not work well near a critical point or near a phase boundary where physical properties sharply change on short length scales, but the question here is whether LDA is qualitatively or just quantitatively incorrect. In a 2D trapped system, quantum Monte Carlo (QMC) simulations [44] and the experimental results [46] show that slightly below the critical value of $(J/U)_c$ the system can undergo a transition from the coexistence of Mott-insulating and BEC state to a pure BEC state by increasing the total number of particles; this effect can not be explained by LDA. Validity of LDA has also been tested for 1D systems [47, 48, 49]. Even if LDA fails around the tip of the Mott lobe, in sufficiently deep lattices we believe that the existence of the BEC is still robust in the wedding-cake system because a number-fluctuating region (which is predicted to be a BEC) between two Mott-insulators is expected to be energetically favorable due to tunneling.

We have shown that the RF spectrum of BEC in deep optical lattices displays one more peak than the Mott-insulator due to the appearance of the second final state that the Mott-insulator lacks. A two-peak structure of the BEC is also predicted in different parameter settings [41]. For the single-site BEC state of our setting, the second final state in the RF transition is associated with density and phase fluctuations, while the first final state, continuously evolving from the final state of Mott-insulating state, is associated with relatively small density fluctuations and no phase change. Different properties of the two final states imply that the BEC in deep optical lattice is composed of two kinds of fluid with one having a higher compressibility than the other. Each RF peak is attributed to each of the components. A similar conclusion

has also been made in Ref. [41]. To confirm the two-component model, we expect that associated density fluctuations can be measured by recently developed experimental techniques that directly image number density profiles of the system with high resolution and precision [21, 22, 23, 24, 25].

Now we turn to experimental issues regarding the two-peak structure that has not been noted in Ref. [38]. (1) The region of the BEC phase is narrow such that signals indicating total number transferred are too small to be detected by current devices. (2) In experiments, the optical lattice potential is adiabatically turned on after the atoms are well trapped and cooled down. In this process, the entropy of the Mott-insulating region transfers to the BEC region and hence the temperature increases to destroy BEC [58, 59]. A solution proposed is to use a surrounding gas to absorb the released entropy [60]. (3) The heating effect can also happen when the RF field is applied. The energy gap in the hyperfine state transition is much larger than the critical temperature of the BEC, which is of order ZJ. If dissipation or spontaneous emission occurs in the RF transition process, the heat released can destroy the BEC. A solution is to shorten the time duration of the RF field. (4) The distance between the two peaks in the spectrum is of order ZJ, which has a typical value $10-50$Hz in the deep lattice regime. According to the uncertainty principle, in order to resolve the two peaks the time duration of the RF field should be more than 100ms. As a result, (1) and (2) are expected to be solved with technical developments in future experiments, while (3) and (4) give a fundamental constraint of the time duration of RF field.

The other experimental signature we have predicted for the BEC shells in the wedding-cake system is relative high interference peaks compared to a pure Mott insulating case. However, a series of theoretical studies show that even a non-BEC gas at $T > T_c$ can display interference peaks [54, 55], a fact confirmed by the experiment [56]. An alternative signature of the onset of BEC is a drastic rising in the interference peaks as temperature is decreased across T_c [57]. In addition, a short TOF expansion that is considered in our toy model does not reflect the exact momentum distribution, which is recovered from the density distribution only in the limit $t \to \infty$ [53]. Quantum and thermal fluctuations [50, 51], interactions [52] and coherence between BEC shells [42] also alter the interference pattern upon TOF expansion. As a test of the robustness of our conclusion, corrections to the interference pattern of our toy model due to the factors presented above are of great interests.

The author's future studies focus on modified Bose-Hubbard systems and suggest three possible avenues. (1) In the presence of a phonon or photon bath, lattice bosons can separately or collectively couple to a set of harmonic oscillators. This system is theoretically described by modifying the Bose-Hubbard model with additional coupling terms, analogous to the Hubbard-Holstein model of the fermion system. Our calculations show that the local coupling to a phonon field tends to delocalize the lattice bosons, which

would provide an experimental method to increase the critical temperature of the condensate by immersing the lattice bosons into another BEC gas. (2) The order parameter at a Mott-insulator (MI) -BEC, MI-MI, or BEC-BEC junction may have a drastic change on the boundary or a certain proximity effect around the boundary. A BEC-BEC junction is supposed to carry particle current in the presence of chemical potential gradient, while a MI-MI junction is not. Our goal is to investigate the order parameter across the junction under various boundary conditions and hence derive conducting properties of the system. As an application, we are interested in designing a device that would be a BEC-BEC junction at certain chemical potential gradient but become a MI-MI junction when the gradient changes sign. Such a device would lead to a possible realization of atomic diodes. (3) The lack of direct evidence of superfluidity in the shell-structure system motivates us to study the moment of inertia of the BEC layers. We would like to investigate the lattice bosons in a rotational field and relate the response of the system to the moment of inertia and other observable quantities.

Chapter 3

Oscillatory pairing in spatially separated fermionic atoms

In this chapter, we turn to another topic of interest: the pairing state in Fermi systems, focusing on that between two hyperfine species of fermionic atoms. We find that due to a specific inhomogeneous confinement that we call a "spin-split trap" (which we will define later), the system can exhibit the coexistence of three phases. One of them is the partially-polarized pairing phase, known as the Fulde-Ferrell-Larkin-Ovchinnikov (FFLO) state, which has oscillatory pairing amplitude but lacks experimental evidence so far. The spin-split-trap system has two advantages motivating us to do further research. (1) It has a richer coexisting-phase structure, compared to the coexistence of two phases in a general population imbalanced system. (2) It provides an experimentally controllable parameter that can be tuned to generate a significant spatial region corresponding to the elusive FFLO state. We will explore and employ these advantages in the following sections. Here we describe a general picture of the study with relevant references and present the organization of this chapter.

A pairing state in systems of attractively interacting fermions was suggested more than fifty year ago and applied in the Bardeen-Cooper-Schrieffer (BCS) theory which successfully explains classical superconductivity [5]. The BCS ground state describes a condensation of pairs composed of two fermions of different spins with zero center of mass momentum in spin singlet state. If different spin species have different density, the number of minor spins (with less density) determines the maximum number of pairs. Therefore, at zero temperature, an equal-mix system is naturally in a fully-paired condensation (or superfluid) phase described by BCS ground state, while a fully polarized (with zero minor species) system is a normal gas due to the lack of pairing. A phase transition, as first suggested in Ref. [92, 93], is expected to take place at a certain critical polarization below which the system is a fully-paired superfluid with unpaired spins spatially separated and above which the system is a normal gas. However, in a certain polarization regime between the fully-paired and fully-polarized phases is another energetically favorable paired phase, the FFLO state [94, 95], in which major and minor spin species of a pair occupy different momentum states and cause condensed pairs having a finite center of mass momentum. Such characteristic momentum, $\mathbf{q}$, is reflected in spatial modulation of the pairing function of the form $e^{i\mathbf{q}\cdot\mathbf{r}}$ [94] or $\cos(\mathbf{q}\cdot\mathbf{r})$ [95].

In atomic systems, tunable interaction via a Feshbach resonance [96] has provided realizations of BCS-paired superfluid states in two-species ultra-cold Fermi gases [12, 97]. In a uniform gas, the number imbalance, or equivalently a chemical potential difference, between the two species tends to suppress pairing, leading to imbalanced superfluid phases and superfluid-normal-gas separation [98, 99, 100] which have been observed in recent experiments [101, 102, 103, 104]. However, the FFLO state, reflecting a partially paired superfluid phase (with spatially-varying pairing amplitude concomitant with the number imbalance), has remained elusive in 3D and has not yet been directly observed although it has been extensively studied theoretically [105, 106, 107].

Recently, attention has turned to one-dimensional (1D) spin-imbalanced systems as a means of realizing FFLO-type states [108, 109, 110, 111, 112, 113, 114, 115, 116, 117] due to the fact that the parameter regime over which they are predicted to exist is much wider than in three dimensions [100]. In recent experiments, a trapped quasi-1D system is realizable in optical lattices [118], and a partially polarized phase that is expected to be of the FFLO type has been observed by inducing population imbalance [119], although the experiment did not probe the associated oscillatory pairing correlations. In this chapter, we study an alternate one-dimensional spin-split-trap setup in which two hyperfine species (representing the two spin states) of attractively interacting fermionic alkali atoms are separately trapped in a controllable way, such as by applying a magnetic field gradient or a species-selective trapping potential in experiments [120, 121, 122]. The system is shown to yield coexistence of a fully-paired phase in which equal population of the two species fully pair with each other, a partially-polarized pairing phase in which the presence of population imbalance causes only a fraction of fermions to form pairs, and a fully-polarized normal phase with only one species of particles and no pairing.

In Section 3.1, we define the 1D spin-split-trap and discuss a means of realizing it. We consider the dependence of relative Zeeman energy between the two hyperfine states on magnetic field and propose a tunable spin-split trap that is created by applying a magnetic field gradient.

In Section 3.2, we capture the coarse-grained features of the phases and pairing amplitudes of the system by various approaches. We discuss possible phases in the local density approximation (LDA) analysis, based on the phase diagram for the homogeneous system derived from a Bethe ansatz treatment. We employ the BCS theory and LDA to compute the gap function at zero separation and estimate the critical separation above which the FFLO-type state emerges. In addition, we provide a simple argument to show the oscillatory behavior of the gap function by considering the Cooper pair wave function in the spin-spilt trap.

In Section 3.3, we introduce the self-consistent mean-field theory, derive the extended Bogoliubov-de Gennes (BdG) equation with spin-dependent trapping, discuss symmetry of the system, and express related

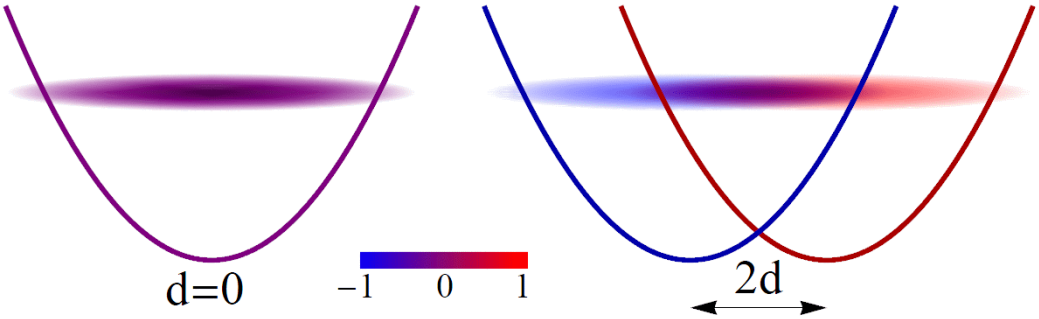

Figure 3.1: Illustration of our proposed setup of cold fermions in a spin-split trap, showing trapping potentials with separation 0 (left) and $2d$ (right) for the two species of fermion with minima for the cigar-shaped clouds shifted along the z direction. The density profiles are shown in grayness, while the spin polarization profiles are shown in color (see color scale).

physical quantities in terms of the quasi-particle wave functions. We use an iterative procedure to numerically solve the BdG equation and compute the gap function as well as the density and imbalance profiles, at various separations. We identity the critical separation and the nodes of the oscillatory gap function. We also plot the finite temperature phase diagram and discuss experimental signatures in local density of states and pair momentum distribution function which reflects appearance of the oscillatory pairing amplitude. Finally, we present directions for future study in Section 3.4.

3.1 Spin-split trap

In this section, we write down a mathematical form the 1D spin-split-trap. The issues of 1D conditions and experimentally realizing a spin-split-trap system are discussed. We consider the dependence of relative Zeeman energy between the two hyperfine states on magnetic field and propose a tunable spin-split trap that is created by applying a magnetic field gradient. The values of field gradient for separating the systems of ^{40}K and ^{6}Li in recent experiments are estimated.

The spin-split trap can be described by the spin-dependent potentials

$$V_\sigma(\mathbf{r}) = \frac{m}{2}[\omega_r^2(x^2+y^2) + \omega_z^2(z-\sigma d)^2], \tag{3.1}$$

where $\omega_z(r)$ are the trapping frequencies in the axial (transverse) directions, m is the atomic mass, and $\sigma = \pm 1$ correspond to the two hyperfine species. The centers of the two traps are separated by a distance $2d$ along z direction. Figure 3.1 shows the spin-split trap with zero and finite separations. We consider the equal-mixed system of N spin-up and N spin-down particles in a quasi-one-dimensional geometry. This limit can be achieved in a highly anisotropic trap having a transverse trapping frequency ω_r such that, for

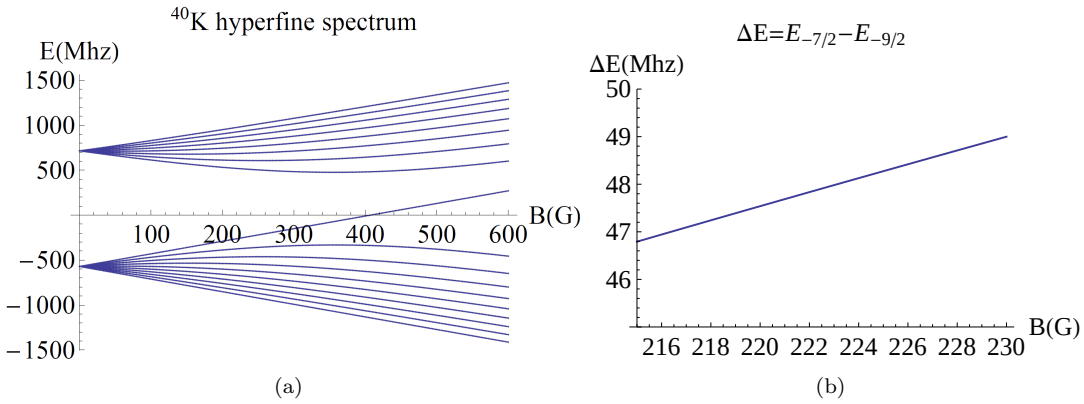

Figure 3.2: (a) The hyperfine spectrum of ^{40}K. (b) The energy difference between the hyperfine states $|F = 9/2, m_F = -9/2\rangle$ and $|F = 9/2, m_F = -7/2\rangle$, the lowest two curves in (a).

N fermions of each species,

$$N\omega_z/\omega_r \quad < \quad 1, \tag{3.2}$$

$$N|a_s|/R_z \quad \ll \quad 1, \tag{3.3}$$

with $\sigma = \pm 1$ for spin up/down species. Here $R_z = \sqrt{2N-1}\,\ell_z$ (with $\ell_z \equiv \sqrt{\hbar/m\omega_z}$ the oscillator length) is the classical radius of the free gas in the z-direction and a_s is the s-wave scattering length for the two-body interactions. In such a trap, Eq. 3.2 guarantees that all particles are well-constrained in the harmonic ground state in the transverse direction, while Eq. 3.3 guarantees that they will not scatter into the excited state in the transverse direction through interaction (the dilute limit). In other words, particles are allowed to disperse only in z direction, and hence form a cigar-shaped cloud (see the density plots in Figure 3.1). Because the transverse degrees of freedom is frozen out, the physical quantities is only z-dependent, and thus the potential becomes

$$V_\sigma(z) = \frac{1}{2}m\omega_z^2(z - \sigma d)^2. \tag{3.4}$$

The boundary of the cloud in z direction is determined in the semi-classical picture by $V_\sigma(z) = \mu_\sigma$, where μ_σ is the chemical potential associated with N. For a non-interacting gas in the spin-split trap, the spin-up (down) species are bounded in the interval $[d - R_z, d + R_z]$ ($[-d - R_z, -d + R_z]$). The cigar-shaped profile in Figure 3.1 represents the total density $\rho(z) = \rho_\uparrow(z) + \rho_\downarrow(z)$ in grayness, and spin polarization $P(z) = M(z)/\rho(z)$ in color referred in the color bar, where $M(z) = \rho_\uparrow(z) - \rho_\downarrow(z)$ in the spin imbalance. When the separation is zero, there is zero spin imbalance everywhere.

The relative potential energy between the two species is linear in space,

$$V_\uparrow(z) - V_\downarrow(z) = 2m\omega_z^2 dz. \tag{3.5}$$

Such a difference can be achieved as the Zeeman energy difference with the application of a magnetic field gradient. To compute the value of the gradient, we consider the hyperfine spectrum of an alkali atom in an external magnetic field with magnitude B and along z direction. The hyperfine Hamiltonian reads

$$\begin{aligned} \hat{H}_{\rm hf} &= A_{\rm hf}\hat{\mathbf{I}}\cdot\hat{\mathbf{J}} + \frac{\mu_B}{h}(g_J\hat{J}_z + g_I\hat{I}_z)B \\ &= \frac{A_{\rm hf}}{2}(\hat{I}_+\hat{J}_- + \hat{I}_-\hat{J}_+) + [A_{\rm hf}\hat{I}_z\hat{J}_z + \frac{\mu_B}{h}(g_J\hat{J}_z + g_I\hat{I}_z)B], \end{aligned} \tag{3.6}$$

where $\hat{\mathbf{I}}$ and $\hat{\mathbf{J}}$ are the nuclear and total electronic angular momentum operators respectively, g_I and g_J are the corresponding g-factors, $A_{\rm hf}$ is the hyperfine constant, and $\mu_B = 1.4$ MHz/Gauss is the Bohr magneton. The spectrum as a function of the magnetic field is obtained by diagonalizing the hyperfine Hamiltonian, which is of finite size in the basis $|I, m_I, J, m_J\rangle$.

Figure 3.2(a) shows the numerically-obtained hyperfine spectrum of a ^{40}K atom as a function of B. The lower and higher groups of curves correspond to the states of $F = 9/2$ and $7/2$ respectively, where F is the quantum number of the total angular momentum. Two states of experimental interests are $|F = 9/2, m_F = -9/2\rangle$ and $|F = 9/2, m_F = -7/2\rangle$, correspond the lowest two curves in Figure 3.2(a). The energy difference between them around the Feshbach resonance regime is roughly linear, as shown in Figure 3.2(b). If we apply an inhomogeneous field $B(z) = B'z$ (where B' is the gradient) on a trapped gas, the two hyperfine species will separate by a distance satisfying Eq. (3.5).

We estimate the gradient needed to have the separation d by expanding the Breit-Rabi formula [123], which well interpolates the energy difference between the weak and strong field limits, in the resonance regime. We obtain

$$E_\uparrow - E_\downarrow = \frac{\mu_B g_J B' z}{2} \times \sum_\sigma \frac{\sigma(\frac{2m_{F\sigma}}{2I+1} + \frac{\bar{B}}{B_0})}{\sqrt{1 + \frac{4m_{F\sigma}}{2I+1} \times \frac{\bar{B}}{B_0} + \left(\frac{\bar{B}}{B_0}\right)^2}}, \tag{3.7}$$

where $\bar{B}$ is the resonance field and B_0 is the characteristic field depending on the atom. Comparing Eq. (3.7) with Eq. (3.5), we can get the relation between the field gradient B' and the separation d. In the experiment of [118], for example, spin-up (down) Fermions correspond to ^{40}K atoms in the $|F = 9/2, m_F = -9/2(-7/2)\rangle$ hyperfine states. The trap frequencies are $\omega_r = 2\pi \times 69$ kHz and $\omega_z = \omega_r/270$, respectively, and $N \sim 100$.

We substitute $\bar{B} = 204$G and $B_0 = 459$G for ^{40}K into Eq. (3.7), substitute ω_z, m, and $d = 0.1R_z$ into Eq. (3.5), and obtain $B' \sim 50$G/cm, which is comparable to the value in experiments [121]. For the system of ^{6}Li atoms [119], we estimate $B' \sim 5000$G/cm, which is less feasible in experiments.

3.2 Coarse-grained features

In this section, we use several approximate approaches to capture the coarse-grained features of the 1D fermions in a spin-split trap. In Subsection 3.2.1, we discuss expected phases in the trap by employing an LDA analysis based on the phase diagram for 1D homogeneous spin-imbalanced fermionic systems derived from a Bethe ansatz treatment [109]. In Subsection 3.2.2, we use the BCS gap equation and LDA analysis to compute the pairing profile. Considering the competition between the gap energy and the exchange energy, we estimate the critical separation as a function of interaction and number of particles. In Subsection 3.2.3, we take into account the inhomogeneous basis (beyond the LDA) and write down the Cooper pair wave function, which shows oscillation when the separation is over a certain value. Although the Cooper problem is a simplified two-body problem, the wave function does possess the same qualitative signatures as the pairing amplitude. Such similarity leads to a detailed study incorporating the many-body effect, which will be discussed in the next section.

3.2.1 Expected phases

To understand the phases of attractive fermions in the 1D spin-split trap, we first summarize previous study of Ref. [109] on the phases of the homogeneous imbalanced system composed of $N_\uparrow$ and $N_\downarrow$ fermions (we assume $N_\uparrow \geq N_\downarrow$). Given the interaction is point-contact-like, the Hamiltonian is

$$H = -\frac{\hbar^2}{2m}\sum_{i=1}^{N_\uparrow+N_\downarrow}\frac{\partial^2}{\partial z_i^2} + g\sum_{i=1}^{N_\uparrow}\sum_{j=N_\uparrow+1}^{N_\uparrow+N_\downarrow}\delta(z_i - z_j), \tag{3.8}$$

where g is the 1D coupling constant and taken negative for attractive interaction. In the quasi-1D system we discussed in the last section, g is related to the 3D scattering length a_s and the transverse oscillator length $\ell_r = \sqrt{\hbar/m\omega_r}$ as [124]

$$g = \frac{2\hbar^2 a_\mathrm{s}}{m\ell_r^2(1 - 1.033a_\mathrm{s}/\ell_r)}. \tag{3.9}$$

Bethe's ansatz provides an exact solution for the ground state energy of Eq. (3.8), as a function of number density $n_{\uparrow,\downarrow} = N_{\uparrow,\downarrow}/L$, with L the size of the system. The chemical potential for each species can be obtained

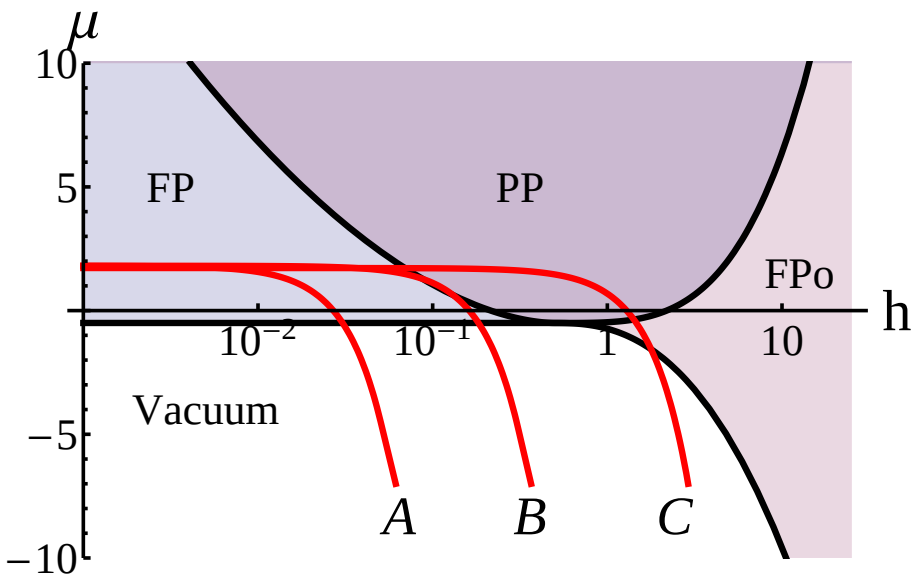

Figure 3.3: Phase diagram of the uniform system taken from Ref. [109]. Here μ and h are measured in units of $mg^2/4\hbar^2$, where g is the 1D coupling constant. The black curves identify boundaries between the four different phases (see text).The red curves A, B, and C represent the LDA trajectories followed by the spin-split system for $d < d_c$, $d = d_c$ and $d > d_c$,respectively.

by $\mu_{\uparrow,\downarrow} = \partial(E/L)/\partial n_{\uparrow,\downarrow}$, so do the total chemical potential μ and the effective magnetic field h given by

$$\begin{aligned} \mu &= (\mu_\uparrow + \mu_\downarrow)/2 \\ h &= (\mu_\uparrow - \mu_\downarrow)/2. \end{aligned} \tag{3.10}$$

Finally, the curves of $n_\uparrow = 0$, $n_\downarrow = 0$, and $n_\uparrow = n_\downarrow$ are plotted in the μ-h plane (black curves in Figure 3.3). Those curves divide the plane into four regions, which correspond to four different phases: the fully-paired (FP) state, where $n_\uparrow = n_\downarrow > 0$, the partially polarized (PP) state, where $n_\uparrow > n_\downarrow > 0$, the fully polarized (FPo) state, where $n_\uparrow > n_\downarrow = 0$, and the vacuum, where $n_\uparrow = n_\downarrow = 0$. The PP phase is expected to be of the FFLO type [108] with a spatially-varying pairing amplitude.

Now we turn to the spin-split-trap system. Within the LDA analysis, we define the local chemical potential $\mu_{\uparrow,\downarrow}(z) = \mu_0 - V_{\uparrow,\downarrow}(z)$, where μ_0 is the total chemical potential of the system. We use the potential of Eq. (3.4) and find that μ and h, defined in Eq. (3.10) and now as a function of z, are related through

$$\mu = \mu_0 - \frac{h^2}{2m\omega_z^2 d^2}. \tag{3.11}$$

The relation of Eq. (3.11) corresponds to downward facing parabolae in the μ versus h phase diagram.

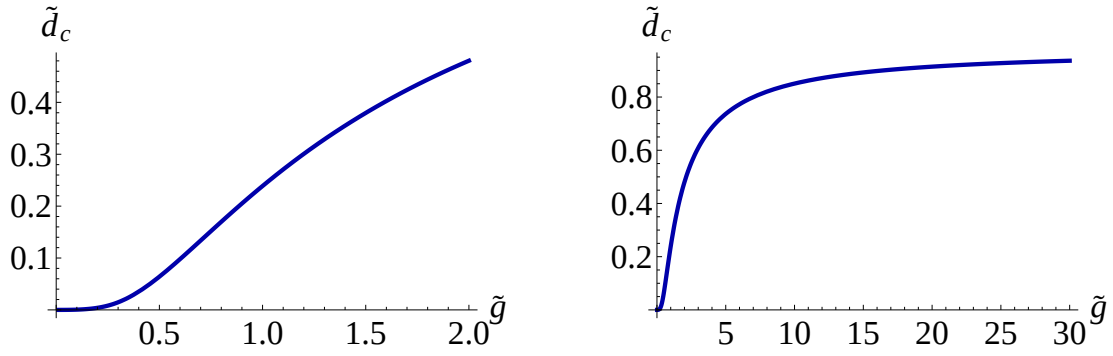

Figure 3.4: Critical Separation $\tilde{d}_c$ vs coupling $\tilde{g}$, based on the BCS theory. The range of $\tilde{g}$ goes from 0 to 2 (30) in the left (right) panels.

In Figure 3.3, we show three curves corresponding to different values of the distance between the two traps. One can see that they traverse different phases from the center $z = 0$ (where $h = 0$) to the edges. For small separation d, the system respects a tight parabola and is thus confined to the fully paired phase. But for larger separation, the parabola broadens and beyond a critical separation $d > d_c$ traverses all three phases as a function of space. In this case, at small z, the local imbalance h remains small enough that the system is locally fully paired. At larger z, the local h exceeds a critical value such that locally the system enters the PP phase which is expected to have oscillatory pairing amplitude [108], although Bethe ansatz does not provide such information. At even larger z, near the edges of the trap, the system is locally in a fully polarized normal phase. Note that in the case of a globally spin-imbalanced system with a single trap, the system would trace a vertical line in the phase diagram, yielding only two regions – a partially polarized core and either fully polarized or fully paired edges [109]. In contrast, our system is able to host all three regions.

3.2.2 BCS theory

In the last subsection, Bethe's ansatz does not provide information about pairing in the imbalanced system. In this subsection, we discuss the profile of the gap function based on the BCS theory and LDA analysis. We consider the competition between the gap function and the effective magnetic field and estimate the critical separation d_c, above which the FFLO-type state emerges.

The BCS gap equation is given by

$$\frac{1}{|g|} = \sum_k \frac{1}{2\sqrt{(\epsilon_k - \mu)^2 + |\Delta|^2}}, \tag{3.12}$$

which takes the form in 1D as

$$\frac{1}{|g|} = \int_{-\infty}^{\infty} \frac{dk_z}{2\sqrt{\left(\epsilon_{k_z} - \mu\right)^2 + |\Delta|^2}} = \int_{0}^{\infty} \frac{N(\epsilon)d\epsilon}{2\sqrt{\left(\epsilon - \mu\right)^2 + |\Delta|^2}}. \tag{3.13}$$

We replace the 1D density of state $N(\epsilon) = \sqrt{m/(2\pi^2\epsilon)}$ and obtain the solution for the gap function in an approximated expression,

$$\Delta = 2(\sqrt{2}+1)\mu \exp\left[-\sqrt{2\hbar^2\pi^2\mu/mg^2}\right]. \tag{3.14}$$

If the potentials for the two species coincide ($d = 0$), in the LDA analysis, we obtain the gap function profile for the trapped system by directly substituting the local the chemical potential $\mu(z) = m\omega_z^2(R_z^2 - z^2)/2$ into Eq. (3.14), where R_z is the classical radius of the cloud. Such a profile is non-monotonic in space and takes the maximum value

$$\Delta_{\max} = \frac{2(\sqrt{2}+1)}{e^2\pi^2}\frac{mg^2}{\hbar^2} \tag{3.15}$$

at the place where $\mu(z) = 2mg^2/\hbar^2\pi^2$.

In the case of finite separation, the local chemical potentials for the two species are different everywhere except at $z = 0$, where $\mu_\uparrow = \mu_\downarrow = m\omega_z^2(R_z^2 - d^2)/2$. Therefore, we can use Eq. (3.14) to estimate the gap at $z = 0$ as a function of d, $\Delta_{z=0}(d)$, which shows the same non-monotonic behavior as the gap profile $\Delta(z)$ at $d = 0$. We would expect $\Delta_{\max} \sim \Delta_{z=0}(d)$ at non-zero separation. If the transition temperature T_c depends on the $\Delta_{\max}$, it would also be a non-monotonic function of d. The mean-field calculations in Section 3.3 show the same results.

From Eq. (3.5), the local field $h(z, d) = V_\uparrow(z) - V_\downarrow(z) = 2m\omega_z^2 dz$, which linearly rises with increase in the separation d. In presence of the field, generating of spin imbalance will lower the energy of the system but cost energy to break pairs. When the field is comparable to the gap, the pairing becomes unstable. We estimate d_c by equating the energy of the system contributed by each of them, which is

$$\int_0^{R_z} h(z, d_c)M(z)dz = \int_0^{R_z} \Delta(z)\rho_p(z)dz, \tag{3.16}$$

where M is the spin imbalance and ρ_p is the pair density. We use the LDA expressions that $M \propto 2d_c z$ and

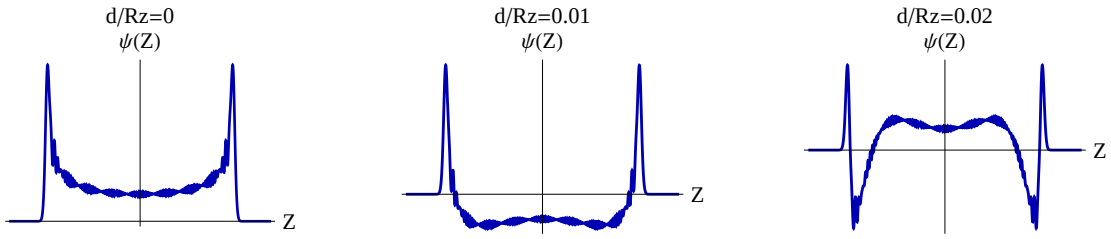

Figure 3.5: The center of mass wave function of a Cooper pair in the spin-split system with separation being 0, 0.01, and $0.02R_z$, from left to right.

$\rho_p \propto (R_z^2 - z^2)/2$ to solve for d_c. The solution in a dimensionless form is

$$\tilde{d}_c = \left\{ \frac{3(\sqrt{2}+1)}{4} \int_0^1 (1-\tilde{z}^2)^2 \exp[-\frac{\pi}{|\tilde{g}|}\sqrt{1-\tilde{z}^2}] d\tilde{z} \right\}^{1/2}, \tag{3.17}$$

where $\tilde{d}_c = d_c/R_z$, $\tilde{z} = z/R_z$, and $\tilde{g} = g/(\hbar\omega_z R_z)$. Figure 3.4 shows the trend of $\tilde{d}_c$ vs $\tilde{g}$. The curve is linear around $\tilde{g} = 1$. In addition, Eq. (3.17) shows that $\tilde{d}_c$ is independent of number of particles N at fixed $\tilde{g}$. Both results agree with the mean-field calculations in Section 3.3.

3.2.3 Cooper pair wave function

In this subsection, we give a simple physical argument about oscillatory behavior of the pairing amplitude due to separation by looking at the wave function of a single Cooper pair. Because occurrence of the paired superfluid state indicates condensation of Cooper pairs, the center of mass wave function of a Cooper pair qualitatively reflects macroscopic pairing amplitude. We write down the Cooper pair wave function in the basis of the harmonic trap, so no LDA analysis is applied here.

We consider two Fermions near the Fermi surface forming a bound pair. Because point-contact interaction only exists between opposite spins, the Hamiltonian of a pair can be represented in the spin space spanned by two states $|\uparrow\downarrow\rangle$ and $|\downarrow\uparrow\rangle$.

$$\hat{H} = \left[\frac{1}{2m}(\hat{p}_{z1}^2 + \hat{p}_{z2}^2) + \frac{1}{2}m\omega_z^2(\hat{z}_1^2 + \hat{z}_2^2) + g\delta(\hat{z}_1 - \hat{z}_2) \right] \begin{pmatrix} 1 & 0 \\ 0 & 1 \end{pmatrix} + 2m\omega_z^2 d(\hat{z}_1 - \hat{z}_2) \begin{pmatrix} 1 & 0 \\ 0 & -1 \end{pmatrix} \tag{3.18}$$

It is checked that if $\begin{pmatrix} \psi(z_1, z_2) \\ 0 \end{pmatrix}$ is an eigen wave function of $\hat{H}$, $\begin{pmatrix} 0 \\ \psi(z_2, z_1) \end{pmatrix}$ is also an eigen wave function with the same energy. Considering that for identical Fermions the wave function is antisymmetric,

we can write down the eigen wave function as

$$\Psi(z_1\sigma_1, z_2\sigma_2) = \psi(z_1, z_2) \otimes |\uparrow\downarrow\rangle - \psi(z_2, z_1) \otimes |\downarrow\uparrow\rangle \,. \tag{3.19}$$

To solve for $\psi(z_1, z_2)$, we can assume

$$\psi(z_1, z_2) = \sum_{m,n=n_F}^{n_F+\delta n} C_{mn}\phi_m(z_1 - d)\phi_n(z_2 + d), \tag{3.20}$$

where $\phi_n(z)$ is the nth eigen wave function of a simple harmonic oscillator (SHO). Substituting Eq. (3.20) into the Schrödinger equation with the Hamiltonian of Eq. (3.18), we obtain a set of equations

$$(E - \epsilon_m - \epsilon_n)C_{mn} = \sum_{m',n'=n_F}^{n_F+\delta n} U_{mnm'n'}C_{m'n'}, \quad \text{for } m, n = n_F \ldots n_F + \delta n \ , \tag{3.21}$$

with the interaction matrix element being

$$U_{mnm'n'} \equiv \int dx_1 dz_2 \phi_n^*(z_2 + d)\phi_m^*(z_1 - d)U(|z_1 - z_2|)\phi_{m'}(z_1 - d)\phi_{n'}(z_2 + h). \tag{3.22}$$

Here ϵ_n is the nth SHO eigen energy. By solving Eq. (3.21), we can exactly get the Cooper pair wave function. However, we can also use a hand-waving argument below to approximately write down the wave function.

If interaction strength is smaller than $\hbar\omega$, the amplitude of pairing between different energy states is ignorable, which means $C_{mn} = \delta_{mn}C_n$. Therefore the total wave function of Eq. (3.19) becomes

$$\Psi(z_1\sigma_1, z_2\sigma_2) = \sum_{n=n_F}^{n_F+\delta n} C_n \left[\phi_n(z_1 - d)\phi_n(z_2 + d) \otimes |\uparrow\downarrow\rangle - \phi_n(z_1 + d)\phi_n(z_2 - d) \otimes |\downarrow\uparrow\rangle\right]. \tag{3.23}$$

The center of mass wave function of a single Cooper pair can show signatures of the gap function. We rewrite Eq. (3.23) in terms of the center of mass coordinate $Z = (z_1 + z_2)/2$ and the relative coordinate $z = (z_1 - z_2)$ and expand it in series of r.

$$\Psi(Z, z, \sigma_1, \sigma_2) = \sum_{n=n_F}^{n_F+\delta n} C_n\phi_n(Z - d)\phi_n(Z + d) \otimes [|\uparrow\downarrow\rangle - |\downarrow\uparrow\rangle] + \mathcal{O}(z). \tag{3.24}$$

Given $n_F = 100$ and $\delta n = 10$, Figure 3.5 shows the center of mass wave function of the leading term in Eq. (3.24). Similar to the BCS results in Subsection 3.2.2, the curve is non-monotonic at $d = 0$. Here the reason in understood by considering higher probability of a particle staying near the edge in a 1d

harmonic trap. We can also see the wave function displaying oscillations at d above a critical value, and the number of nodes increases with increase in d. In this heuristic argument, we assume two particles of different species form a bound pair, but we do not consider the actual effect of the interaction. However, the pair wave function naturally exhibits oscillations in the separated trap basis. In the next section, we will follow the BdG method, considering the interaction by introducing two mean fields into the microscopic Hamiltonian. By self-consistently solve the mean-field Hamiltonian, we obtain the quasi-particle energy and the corresponding wave functions, which can be use the calculate the gap function and other related physical quantities at zero or finite temperature.

3.3 Mean-field approach

In the last section, we saw that the gap function profile can be in a spin-spilt trap because of the trap potential and the FFLO pairing. The two methods we use to study the pairing states approach the answer from different aspects and have their disadvantages. (1) The LDA analysis considers many-body effect but simplifies the trap effect. The Hamiltonian includes many-body degrees of freedom but no trap potential. The trap effect is applied after the uniform solutions are obtained. (2) The Cooper problem, however, considers the trap effect but simplifies the many-body effect. The Hamiltonian includes the trap potential but only 2-body degrees of freedom.

In this section, we apply the self-consistent mean-field (BdG) theory, considering both many-body and trap effects, which is expected to provide more accurate results. In Subsection 3.3.1, we construct the mean-field Hamiltonian for a general spin-dependent system, introducing two mean fields, the Hartree field and the BCS pairing field. By self-consistently minimizing the free energy, we derive the extended Bogoliubov-de Gennes (BdG) equation, which solves for the quasi-particle energies and wave functions. We write down the gap function, density profiles, and free energy of the system in terms of those quasi-particle solutions. Subsection 3.3.2 discusses symmetry of the system, including the time reversal correspondence between the BdG solutions and the parity symmetry that is specifically for the 1D spin-split trap. In Subsection 3.3.3, we present an iterative procedure to numerically solve the BdG equation and discuss the parameter regime where the numerical calculation is convergent. In Subsection 3.3.4, we illustrate gap, density, and imbalance profiles from the numerical calculations as a function of various parameters. We identity the critical separation above which the system has three concurrent phases and the nodes of the oscillatory gap function in the partially-polarized region. We also plot the finite temperature phase diagram and show how robust the nodal structure of the gap function is against the temperature effect. In Subsection 3.3.5, we discuss experimental signatures

in the pair momentum distribution and density of states, which reflects appearance of the oscillatory pairing, or equivalently, the FFLO state.

3.3.1 BdG treatment

We begin with a general microscopic Hamiltonian in a second quantization form describing interacting Fermions of two species,

$$H = \int d\mathbf{r} \sum_{\sigma} \hat{\psi}^{\dagger}_{\sigma}(\mathbf{r}) H^{0}_{\sigma} \hat{\psi}_{\sigma}(\mathbf{r}) + g \hat{\psi}^{\dagger}_{\uparrow}(\mathbf{r}) \hat{\psi}^{\dagger}_{\downarrow}(\mathbf{r}) \hat{\psi}_{\downarrow}(\mathbf{r}) \hat{\psi}_{\uparrow}(\mathbf{r}), \tag{3.25}$$

where $H^{0}_{\sigma} = -p^2/2m_{\sigma} + V_{\sigma}(\mathbf{r}) - \mu_{\sigma}$ is the single particle Hamiltonian, including kinetic energy, potential energy and chemical potential corresponding to spin σ. The coupling constant g is negative for BCS pairing. Following the standard mean-field approach [125], we construct the mean-field Hamiltonian,

$$H_M = \int d\mathbf{r} \sum_{\sigma} \hat{\psi}^{\dagger}_{\sigma}(\mathbf{r}) [H^{0}_{\sigma} + U_{\sigma}(\mathbf{r})] \hat{\psi}_{\sigma}(\mathbf{r}) + \Delta(\mathbf{r}) \hat{\psi}^{\dagger}_{\uparrow}(\mathbf{r}) \hat{\psi}^{\dagger}_{\downarrow}(\mathbf{r}) + \Delta^{*}(\mathbf{r}) \hat{\psi}_{\downarrow}(\mathbf{r}) \hat{\psi}_{\uparrow}(\mathbf{r}), \tag{3.26}$$

where $\Delta(\mathbf{r})$ and $U_{\sigma}(\mathbf{r})$ are the BCS field and the Hartree-Fock fields correspondingly. H_M is diagonalized as

$$H_M = E_g + \sum_{n>0,\sigma} \epsilon_{n\sigma} \hat{\gamma}^{\dagger}_{n\sigma} \hat{\gamma}_{n\sigma} \tag{3.27}$$

by a Bogoliubov transformation,

$$\hat{\psi}_{\sigma}(\mathbf{r}) = \sum_{n>0} [u_{n\sigma}(\mathbf{r}) \hat{\gamma}_{n\sigma} - \sigma v^{*}_{n\sigma}(\mathbf{r}) \hat{\gamma}^{\dagger}_{n,-\sigma}]. \tag{3.28}$$

The quasi-particle energies $\epsilon_{n\sigma}$ and wave functions (u, v) are determined by the BdG equation,

$$\begin{pmatrix} H^{0}_{\sigma} + U_{\sigma} & \Delta \\ \Delta^{*} & -H^{0}_{-\sigma} - U_{-\sigma} \end{pmatrix} \begin{pmatrix} u_{n\sigma} \\ v_{n,-\sigma} \end{pmatrix} = \epsilon_{n\sigma} \begin{pmatrix} u_{n\sigma} \\ v_{n,-\sigma} \end{pmatrix}, \tag{3.29}$$

where we label positive ϵ_n with $n = 1, 2, 3...$ and negative ϵ_n with $n = -1, -2, -3$, keeping the order that $\epsilon_n < \epsilon_m$ if $n < m$. We need the solutions only with positive ϵ to calculate physical quantities. There are some identities for the quasi-particle wave functions,

$$\int dr [u^{*}_{m\sigma}(\mathbf{r}) u_{n\sigma}(\mathbf{r}) + v^{*}_{m,-\sigma}(\mathbf{r}) v_{n,-\sigma}(\mathbf{r})] = \delta_{mn}$$

$$\int d\mathbf{r}[u_{n\uparrow}(\mathbf{r})v_{m\uparrow}(\mathbf{r}) - u_{m\downarrow}(\mathbf{r})v_{n\downarrow}(\mathbf{r})] = 0$$
$$\sum_{n>0}[u^*_{n\sigma}(\mathbf{r})u_{n\sigma}(\mathbf{r}') + v_{n,-\sigma}(\mathbf{r})v^*_{n,-\sigma}(\mathbf{r}')] = \delta(\mathbf{r}-\mathbf{r}')$$
$$\sum_{n>0}[u_{n\uparrow}(\mathbf{r})v^*_{n\downarrow}(\mathbf{r}') - v^*_{n\uparrow}(\mathbf{r})u_{n\downarrow}(\mathbf{r}')] = 0 \tag{3.30}$$

The mean-field variables Δ and U_σ are self-consistently determined by requiring the free energy of the system calculated from the initial Hamiltonian of Eq. (3.25) and the eigen states of the mean-field Hamiltonian H_M ($F = \langle H - TS\rangle$) be stationary with variance of the fields. We let $\delta F = 0$ and derive the self-consistent equations,

$$\Delta(\mathbf{r}) = g\left\langle\hat{\psi}_\downarrow\hat{\psi}_\uparrow\right\rangle = -g\sum_{n>0}[u_{n\downarrow}(\mathbf{r})v^*_{n\uparrow}(\mathbf{r})(1-f_{n\downarrow}) - u_{n\uparrow}(\mathbf{r})v^*_{n\downarrow}(\mathbf{r})f_{n\uparrow}]$$
$$U_{-\sigma}(\mathbf{r}) = g\left\langle\hat{\psi}^\dagger_\sigma\hat{\psi}_\sigma\right\rangle = g\rho_\sigma(\mathbf{r}) = g\sum_{n>0}[|u_{n\sigma}(\mathbf{r})|^2 f_{n\sigma} + |v_{n\sigma}(\mathbf{r})|^2(1-f_{n,-\sigma})], \tag{3.31}$$

where $f_{n\sigma} = [\exp(\epsilon_{n\sigma}/k_BT)+1]^{-1}$ is Fermi distribution function. Once the quasi-particle solutions are known, we can directly calculate the spatial profiles of the gap function, total density, and spin imbalance from Eq. (3.31). The system is in the superfluid phase if $\Delta(\mathbf{r}) \neq 0$ while in the normal phase if $\Delta(\mathbf{r}) = 0$. The free energy of the system is given by

$$\begin{aligned} F &= \sum_{n>0,\sigma}\epsilon_{n\sigma}[f_{n\sigma} - \int|v_{n,-\sigma}(\mathbf{r})|^2 d\mathbf{r}] - \frac{1}{g}\int(U_\uparrow(\mathbf{r})U_\downarrow(\mathbf{r}) + |\Delta(\mathbf{r})|^2)d\mathbf{r} \\ &\quad -k_BT\sum_{n>0,\sigma}[f_{n\sigma}\ln f_{n\sigma} + (1-f_{n\sigma})\ln(1-f_{n\sigma})] \end{aligned} \tag{3.32}$$

3.3.2 Time-reversal and parity symmetry

In this subsection, we discuss time-reversal symmetry of the general BdG solutions and specific parity symmetry for the 1D spin-spilt potential. Applying the symmetry properties will simplify the calculations for physical quantities.

Given H^0_σ and U_σ real, the Hamiltonians with $\sigma = \uparrow, \downarrow$ in Eq.(3.29) are related to each other by a time-reversal transformation

$$(-i\sigma_y K) = \begin{pmatrix} 0 & -1 \\ 1 & 0 \end{pmatrix} K \equiv \Theta, \tag{3.33}$$

where K is the complex conjugate operator. We transform Eq.(3.29) of $\sigma =\downarrow$ and have

$$\Theta \begin{pmatrix} H_\downarrow & \Delta \\ \Delta^* & -H_\uparrow \end{pmatrix} \Theta^{-1}\Theta \begin{pmatrix} u_{n\downarrow} \\ v_{n\uparrow} \end{pmatrix} = \Theta\epsilon_{n\downarrow} \begin{pmatrix} u_{n\downarrow} \\ v_{n\uparrow} \end{pmatrix}$$
$$\Rightarrow \quad \begin{pmatrix} H_\uparrow & \Delta \\ \Delta^* & -H_\downarrow \end{pmatrix} \begin{pmatrix} -v^*_{n\uparrow} \\ u^*_{n\downarrow} \end{pmatrix} = -\epsilon_{n\downarrow} \begin{pmatrix} -v^*_{n\uparrow} \\ u^*_{n\downarrow} \end{pmatrix}, \tag{3.34}$$

where $H_\sigma \equiv H^0_\sigma + U_\sigma$ is also real.

We compare it with Eq.(3.29) of $\sigma =\uparrow$,

$$\begin{pmatrix} H_\uparrow & \Delta \\ \Delta^* & -H_\downarrow \end{pmatrix} \begin{pmatrix} u_{n\uparrow} \\ v_{n\downarrow} \end{pmatrix} = \epsilon_{n\uparrow} \begin{pmatrix} u_{n\uparrow} \\ v_{n\downarrow} \end{pmatrix}, \tag{3.35}$$

keep the order of labeling, and get the time reversal correspondence

$$(\epsilon_{n\downarrow}, u_{n\downarrow}, v_{n\uparrow}) = (-\epsilon_{-n\uparrow}, v^*_{-n\downarrow}, -u^*_{-n\uparrow}). \tag{3.36}$$

We can solve the whole spectrum of the spin-up case and use the correspondence to obtain the solutions of positive energies for the spin-down case. We can also simplify the self-consistent equations as

$$\Delta(\mathbf{r}) = g \sum_{\text{all n}} u_{n\uparrow}(\mathbf{r}) v^*_{n\downarrow}(\mathbf{r}) f_{n\uparrow}$$
$$U_{-\sigma}(\mathbf{r}) = g\rho_\sigma = g \sum_{\text{all n}} |u_{n\sigma}(\mathbf{r})|^2 f_{n\sigma} \tag{3.37}$$

Now we turn to the 1D spin-split trap system with potential of Eq. (3.4). The trap shifts spin-up and spin-down components by the same distance d but toward opposite directions In other words, the potentials of the time-reversed partners has parity symmetry as $V_\downarrow(z) = V_\uparrow(-z)$. Therefore we expect the density distributions also have parity symmetry that

$$\rho_\uparrow(z) = \rho_\downarrow(-z) \Rightarrow U_\downarrow(z) = U_\uparrow(-z). \tag{3.38}$$

Applying this symmetry on the diagonal elements of the BdG Hamiltonian of Eq. (3.29), we obtain the same parity symmetry,

$$H_\uparrow(-z) = H_\downarrow(z), \text{ with} \tag{3.39}$$

$$H_\sigma(z) = -\frac{1}{2m}\partial_z^2 + \frac{1}{2}m\omega^2(z-\sigma d)^2 - \mu + U_\sigma(z). \tag{3.40}$$

Because the gap function is time-reversal invariant ($\langle\Theta^{-1}\hat{\psi}_\downarrow\hat{\psi}_\uparrow\Theta\rangle = \langle\hat{\psi}_\downarrow\hat{\psi}_\uparrow\rangle$), the parity transformation of Δ should be related to itself, up to a global phase. Assuming Δ real without lost of generality leaves us two possibilities $\Delta(-z) = \pm\Delta(z)$. We would like to show that both satisfy the self-consistent equation.

If $\Delta(-z) = \Delta(z)$, the parity transformation of Eq. (3.35) becomes

$$\epsilon_{n\uparrow}\begin{pmatrix} u_{n\uparrow}(-z) \\ v_{n\downarrow}(-z) \end{pmatrix} = \begin{pmatrix} \hat{H}_\uparrow(-z) & \Delta(-z) \\ \Delta(-z) & -\hat{H}_\downarrow(-z) \end{pmatrix}\begin{pmatrix} u_{n\uparrow}(-z) \\ v_{n\downarrow}(-z) \end{pmatrix} = \begin{pmatrix} \hat{H}_\downarrow(z) & \Delta(z) \\ \Delta(z) & -\hat{H}_\uparrow(z) \end{pmatrix}\begin{pmatrix} u_{n\uparrow}(-z) \\ v_{n\downarrow}(-z) \end{pmatrix} \tag{3.41}$$

We compare it with Eq. (3.29) of $\sigma =\downarrow$,

$$\begin{pmatrix} H_\downarrow & \Delta \\ \Delta^* & -H_\uparrow \end{pmatrix}\begin{pmatrix} u_{n\downarrow} \\ v_{n\uparrow} \end{pmatrix} = \epsilon_{n\downarrow}\begin{pmatrix} u_{n\downarrow} \\ v_{n\uparrow} \end{pmatrix}, \tag{3.42}$$

using the time-reversal correspondence of Eq. (3.36), and get

$$\{\epsilon_{n\uparrow}, u_{n\uparrow}(-z), v_{n\downarrow}(-z)\} = \{\epsilon_{n\downarrow}, u_{n\downarrow}(z), v_{n\uparrow}(z)\} = \{-\epsilon_{-n\uparrow}, v^*_{-n\downarrow}(z), -u^*_{-n\uparrow}(z)\}. \tag{3.43}$$

The self-consistency is checked as

$$\begin{aligned} \Delta(-z) &= g\sum_{\text{all n}} u_{n\uparrow}(-z)v^*_{n\downarrow}(-z)f_{n\uparrow} = g\sum_{\text{all n}} -v^*_{-n\downarrow}(z)u_{-n\uparrow}(z)(1-f_{-n\uparrow}) \\ &= g\sum_{\text{all n}} v^*_{n\downarrow}(z)u_{n\uparrow}(z)f_{n\uparrow} = \Delta(z). \end{aligned} \tag{3.44}$$

Here we apply the identity $\sum_{\text{all n}} u_{n\uparrow}(z)v^*_{n\downarrow}(z) = 0$ derived from Eq.(3.30).

If $\Delta(-z) = -\Delta(z)$, the parity transformation of Eq.(3.35) becomes

$$\begin{aligned} &\begin{pmatrix} \hat{H}_\uparrow(-z) & \Delta(-z) \\ \Delta(-z) & -\hat{H}_\downarrow(-z) \end{pmatrix}\begin{pmatrix} u_{n\uparrow}(-z) \\ v_{n\downarrow}(-z) \end{pmatrix} = \epsilon_{n\uparrow}\begin{pmatrix} u_{n\uparrow}(-z) \\ v_{n\downarrow}(-z) \end{pmatrix} \\ \Rightarrow\ &\begin{pmatrix} \hat{H}_\downarrow(z) & -\Delta(z) \\ -\Delta(z) & -\hat{H}_\uparrow(z) \end{pmatrix}\begin{pmatrix} u_{n\uparrow}(-z) \\ v_{n\downarrow}(-z) \end{pmatrix} = \epsilon_{n\uparrow}\begin{pmatrix} u_{n\uparrow}(-z) \\ v_{n\downarrow}(-z) \end{pmatrix} \\ \Rightarrow\ &\begin{pmatrix} \hat{H}_\uparrow(z) & \Delta(z) \\ \Delta(z) & -\hat{H}_\downarrow(z) \end{pmatrix}\begin{pmatrix} u_{n\uparrow}(-z) \\ v_{n\downarrow}(-z) \end{pmatrix} = -\epsilon_{n\uparrow}\begin{pmatrix} u_{n\uparrow}(-z) \\ v_{n\downarrow}(-z) \end{pmatrix} \end{aligned} \tag{3.45}$$

It turns back to Eq.(3.35) with

$$\{u_{n\uparrow}(-z), v_{n\downarrow}(-z)\} = \{v_{-n\downarrow}(z), u_{-n\uparrow}(z)\}. \tag{3.46}$$

The self-consistency is checked as

$$\begin{aligned}\Delta(-z) &= g\sum_{\text{all n}} u_{n\uparrow}(-z)v^*_{n\downarrow}(-z)f_{n\uparrow} = g\sum_{\text{all n}} v_{-n\downarrow}(z)u^*_{-n\uparrow}(z)f_{n\uparrow} = g\sum_{\text{all n}} v_{n\downarrow}(z)u^*_{n\uparrow}(z)(1-f_{n\uparrow}) \\ &= -g\sum_{\text{all n}} v_{n\downarrow}(z)u^*_{n\uparrow}(z)f_{n\uparrow} = -\Delta^*(z) = -\Delta(z). \end{aligned} \tag{3.47}$$

In summary, we have shown the time-reversal correspondence between the solutions of the general BdG equation and had the gap functions of even and odd parity are both self-consistently checked for the 1D spin-split-trap system. However, our numerical calculations in the next subsection show that the even-parity solution is always energetically favorable. Therefore, we present only the even-parity solution in this chapter.

3.3.3 Numerical calculations

As we discussed in the last subsection, the time-reversal symmetry allows us to get the quasi-particle solutions of the BdG equation of Eq.(3.29) by solving only the spin-up case of Eq.(3.35). In numerical calculations, we use the variational method to get the self-consistent gap function and an iterative procedure to vary the gap function until it converges to the self-consistent solution [126]. The procedure is below.

(a) We solve Eq. (3.35) with the one-particle Hamiltonian of Eq. (3.40) at given coupling g, separation d and temperature T. We begin with $\rho^{(0)}_\sigma$ being density profiles of interacting normal gases in the same trap configurations, and a trial gap function $\Delta^{(0)}(z)$.

(b) We put the solutions $\{\epsilon^{(1)}_{n\sigma}, u^{(1)}_{n\sigma}, v^{(1)}_{n\sigma}\}$ into the self-consistent equation of Eq. (3.37) to calculate the density profile $\rho^{(1)}_\sigma$ and the gap function $\Delta^{(1)}$.

(c) We repeat the step (b) to get $\Delta^{(q)}$ from $\Delta^{(q-1)}$ until the variance of the gap

$$D^{(q)}_\Delta = \frac{\int |\Delta^{(q)} - \Delta^{(q-1)}|^2 dz}{\int |\Delta^{(q-1)}|^2 dz} \tag{3.48}$$

and variance of the density $D^{(q)}_\rho$ (of the same form) are within the precision we need. Therefore $\Delta^{(q)}$ and $\rho^{(q)}$are self-consistent solutions to the BdG equation.

(d) In case that the self-consistent solutions obtained are associated with the local maximum of the free energy. We use the same iterative method to get the Hartree fields for the normal state with the constrain

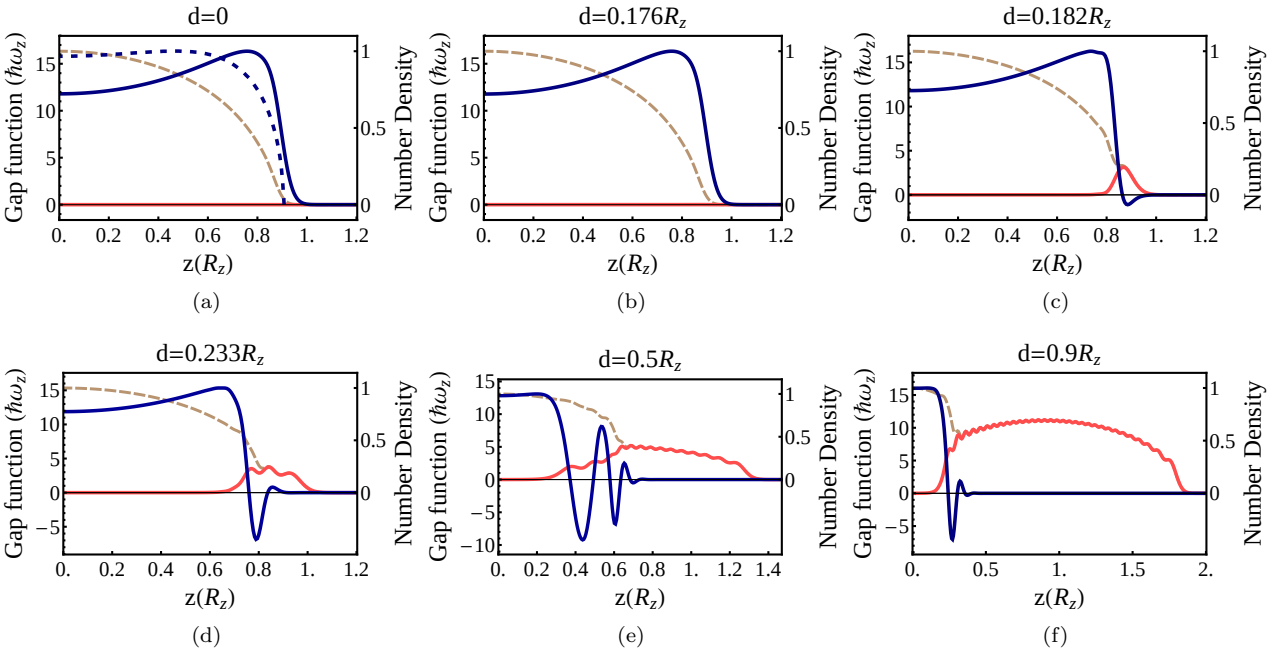

Figure 3.6: (a-f) Spatial profiles of the gap Δ (solid dark-blue curve; axis on left-hand side of graph), normalized total density $\rho/\max[\rho]$, and spin imbalance $M/\max[\rho]$ (dashed light-brown and solid light-red curves, respectively; axis on right-hand side of graph) in the $z \geq 0$ region at $d = 0$, 0.176, 0.182, 0.233, 0.5 and $0.9R_z$, respectively. In (a), the dashed dark-blue curve is the gap function obtained by LDA and BCS gap equation. In (b) and (c), the separations are just below and above the critical value for appearance of the first node.

$\Delta = 0$. By checking that the free energy of the superfluid state is smaller than that of the normal state, we ensure the superfluid state is energetically favorable.

In the numerical calculations, the solutions converge within a parameter range of the coupling constant. We estimate the convergent range below. Given that the gap function $\tilde{\Delta}$, the eigen functions $(\tilde{u}, \tilde{v})$ and the eigen energy $\tilde{\epsilon}$ are the self-consistent solutions to the BdG equation (for simplicity we do not consider the spin subscripts), and the trial wave function $\Delta^{(0)}$ is different from $\tilde{\Delta}$ by

$$\Delta^{(0)} = \tilde{\Delta} + \delta\Delta^{(0)}. \tag{3.49}$$

We use perturbation theory to estimate a condition at which the difference will become smaller and smaller in the iterative calculations. Substituting Eq.(3.49) into the BdG equation, we have

$$\left[\begin{pmatrix} \hat{H} & \tilde{\Delta} \\ \tilde{\Delta} & -\hat{H} \end{pmatrix} + \begin{pmatrix} 0 & \delta\Delta^{(0)} \\ \delta\Delta^{(0)} & 0 \end{pmatrix}\right]\left[\begin{pmatrix} \tilde{u}_n \\ \tilde{v}_n \end{pmatrix} + \begin{pmatrix} \delta u_n^{(1)} \\ \delta v_n^{(1)} \end{pmatrix}\right] = (\tilde{\epsilon}_n + \delta\epsilon_n^{(1)})\left[\begin{pmatrix} \tilde{u}_n \\ \tilde{v}_n \end{pmatrix} + \begin{pmatrix} \delta u_n^{(1)} \\ \delta v_n^{(1)} \end{pmatrix}\right] \tag{3.50}$$

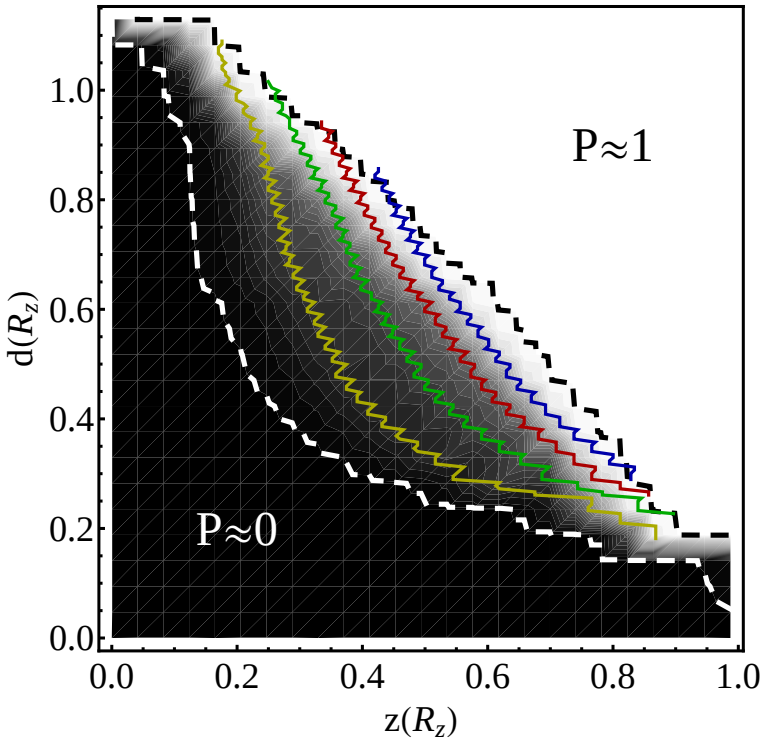

Figure 3.7: Density plot of the polarization P as a function of position z and separation d. The gray scale is bounded by 0 and 1. The dashed white (black) contours correspond to $P = 0.01$ (0.99). The solid curves indicate positions of the first four nodes.

The first order perturbation theory yields

$$\begin{pmatrix} \delta u_n^{(1)} \\ \delta v_n^{(1)} \end{pmatrix} = \sum_{k\neq n} \frac{\delta\Delta_{kn}^{(0)} + \delta\Delta_{nk}^{(0)}}{\tilde{\epsilon}_n - \tilde{\epsilon}_k} \begin{pmatrix} \tilde{u}_k \\ \tilde{v}_k \end{pmatrix}, \tag{3.51}$$

where $\delta\Delta_{kn}^{(0)} \equiv \int dr \tilde{u}_k(r)\delta\Delta^{(0)}(r)\tilde{v}_n(r)$. We use the self-consistent equation to obtain $\Delta^{(1)}$,

$$\begin{aligned} \Delta^{(1)} &= g\sum_{\text{all n}} (\tilde{u}_n + \delta u_n^{(1)})(\tilde{v}_n + \delta v_n^{(1)})f_n = \tilde{\Delta} + g\sum_{\text{all n}} (\tilde{u}_n\delta v_n^{(1)} + \tilde{v}_n\delta u_n^{(1)})f_n \\ \Rightarrow \quad \delta\Delta^{(1)} &= \Delta^{(1)} - \tilde{\Delta} = g\sum_{\text{all n,k}\neq\text{n}} (\frac{\delta\Delta_{kn}^{(0)} + \delta\Delta_{nk}^{(0)}}{\tilde{\epsilon}_n - \tilde{\epsilon}_k})(\tilde{u}_n\tilde{v}_k + \tilde{v}_n\tilde{u}_k)f_n. \end{aligned} \tag{3.52}$$

We can do the estimation by considering

$$\begin{aligned} &\tilde{\epsilon}_n - \tilde{\epsilon}_k \sim \mathcal{O}(\hbar\omega), \\ &\delta\Delta_{kn}^{(0)} \sim \mathcal{O}(\delta\Delta^{(0)}), \\ &u \sim v \sim \mathcal{O}(R^{-D/2}), \end{aligned}$$

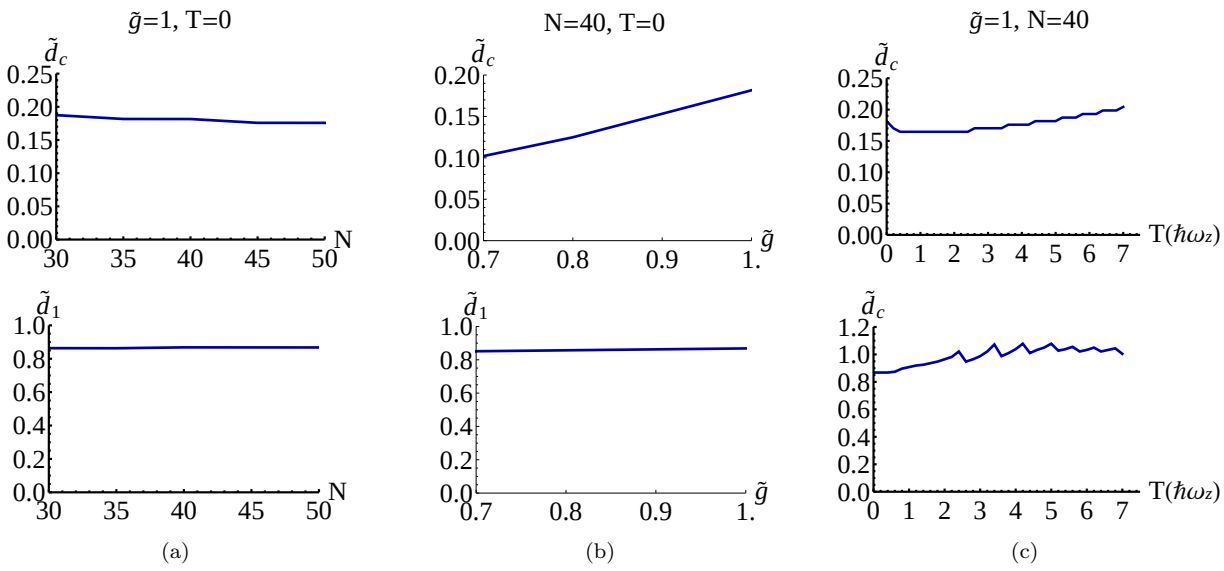

Figure 3.8: Dimensionless critical separation $\tilde{d}_c$ (up panels) and position of the first node $\tilde{d}_1$ at d just above d_c (down panels) vs number of particles N, dimensionless coupling $\tilde{g}$, and temperature, with the other two fixed ((a), (b), and (c), respectively).

$$\Rightarrow \quad \delta\Delta^{(1)}/\delta\Delta^{(0)} \sim \mathcal{O}(\frac{g}{\hbar\omega R^D}), \tag{3.53}$$

where R is the characteristic size of the system and D the dimension. In the 1D trapped system, $R = R_z = \sqrt{2N-1}\ell_z$. If $g < \mathcal{O}(\hbar\omega_z R_z)$, the trial gap function will finally converge to the self-consistent solution. The numerical calculations confirm that the result does not converge if $g > 1.5\hbar\omega_z R_z$.

3.3.4 Numerical results: gap function with nodes

In this subsection, we present the numerical results of the BdG calculations for the system of $N_\uparrow = N_\downarrow = 40$ and $g = \hbar\omega_z R_z$. We show the behavior of the gap function $\Delta(z)$ as well as the density $\rho(z)$ and imbalance $M(z)$ in various parameter regimes and specify the regime where the gap function is oscillatory with nodes, the signature for the FFLO state.

First we increase the separation d of the spin-split trap and present in Figure 3.6 the evolution of $\Delta(z)$ (solid dark-blue curve), $\rho(z)$ (dashed light-brown curve), and $M(z)$ (solid light-red curve) with respect to d. The density and gap have even parity symmetry, while the imbalance has odd parity symmetry, so we can easily get the information for $z < 0$ region. At $d = 0$, the gap function is non-monotonic as we expected from the 1D BCS gap equation and LDA analysis (dashed dark-blue curve in Panel (a)), and the imbalance is zero everywhere in the system. If the separation is non-zero but smaller than the critical value ($d < d_c$), the gap function and density profiles almost remain the same shape as those of $d = 0$. Panel (b) shows

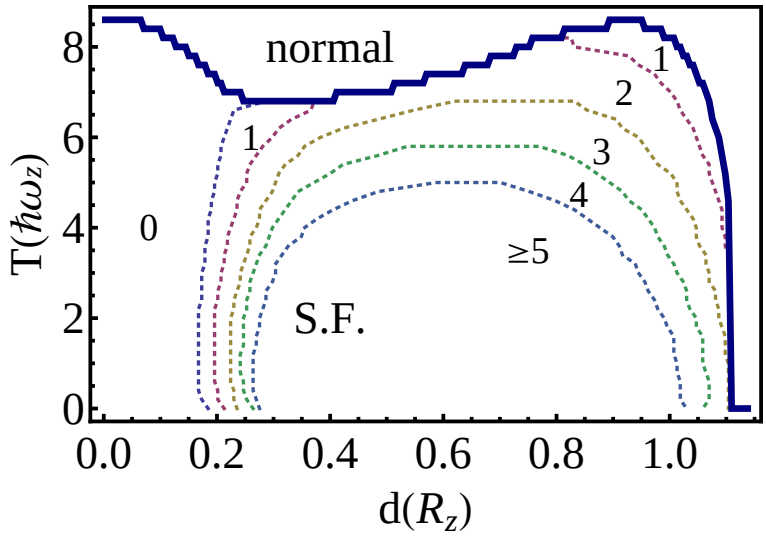

Figure 3.9: Phase diagram as a function of separation and temperature. The solid line separates the normal phase and the superfluid phase. In the superfluid phase, the dashed lines separate regions of the gap functions with different number of nodes.

the profiles when d just below d_c. The spin imbalance becomes non-zero but small compared with that at $d > d_c$ such that we can not tell the difference between the $M(z)$ in Panel (b) from that in Panel (a). When d is right above d_c, as shown in Panel (c), the profiles near the center of the trap do not show much difference from the $d < d_c$ case. However, $M(z)$ sharply increases to a significant value in a short range near the edge, and $\Delta(z)$ develops a node in this region. The regions of $\rho(z) > M(z) \sim 0$, $\rho(z) > M(z) > 0$, and $\rho(z) \sim M(z) > 0$ correspond to the fully-paired (FP, $P = 0$), partially-polarized (PP, $0 < P < 1$), and fully-polarized (Fpo, $P = 1$) phases in the LDA analysis in Subsection 3.2.1, where the polarization is defined as $P(z) = M(z)/\rho(z)$. Therefore, the mean-field results agree with the LDA analysis in three concurrent phases at $d > d_c$, although they disagree in the quantitative value of d_c. Above $d > d_c$, with continuing increase in d, the PP region increases, and more nodes of the gap functions emerge in this region, as shown in Panel (d) of two nodes and (e) of more than five nodes. However, for larger d ($> 0.5R_z$), the PP region shrinks and the number of nodes in Δ decrease. At $d = 0.9R_z$ of Panel (f), the gap function has only three nodes, less than that in Panel (e).

Our results clearly show the intimate connection between the PP phase and oscillatory pairing correlations. In Figure 3.7, we present a global view of the polarization P as a function of position z, and separation d, along with the spatial position of the nodes in $\Delta(z)$. It can be clearly seen that the nodes only exist in the PP region, $0 < P < 1$. The correlation between the polarization and nodal structure indicates that this region is indeed of the FFLO type and is sandwiched by a FP superfluid for $P \to 0$ towards the center of the spin-split trap and a FPo normal fluid for $P \to 1$ at the edges. Partial polarization, thus, provides an

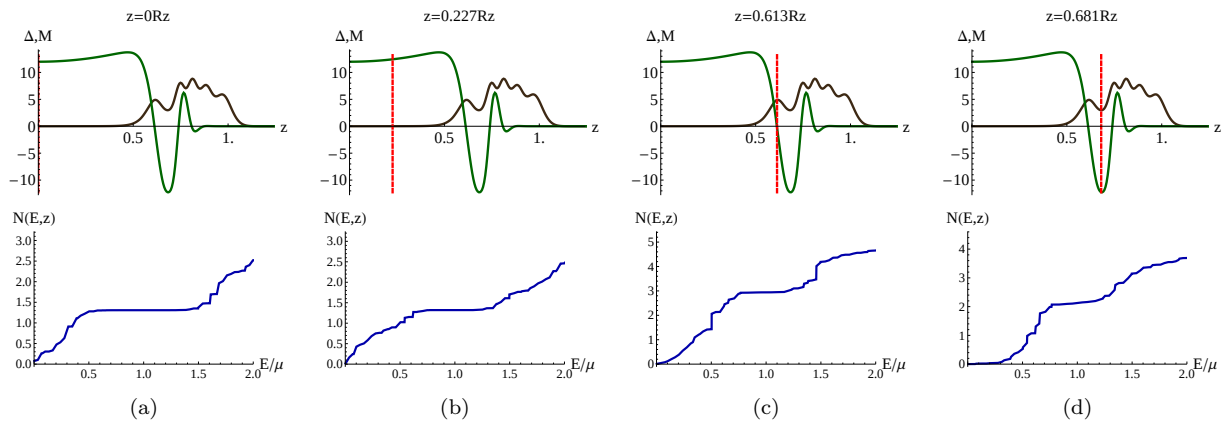

Figure 3.10: Top: the gap function and spin imbalance profile at $d = 0.28R_z$. Bottom: the local number of state $N(E, z)$ (with its derivative with respect to E being the local density of state) at the position corresponds to the red dashed vertical line in the up panels.

indirect experimentally measurable signature of the oscillatory pairing correlations.

Figure 3.8 shows the trends of the dimensionless critical separation $\tilde{d}_c = d_c/R_z$ and position of the first node $\tilde{d}_1$ at $\tilde{d}$ just above $\tilde{d}_c$ with respect to the total number of particles N from 35 to 50, the dimensionless coupling constant $\tilde{g} = g/(\hbar\omega_z R_z)$ from 0.7 to 1, and temperature T from 0 to $7\hbar\omega_z$. Those ranges are chosen in the regime of numerical convergence. We see that $\tilde{g}$ is independent in N and linear in $\tilde{g}$, in agreement with the BCS results in Subsection 3.2.2. The position of the first node $\tilde{d}_1$ is robust against N and $\tilde{g}$. In addition, we notice that positions of nodes are also robust against the separation d until a new node appears. When it happens, all existing nodes suddenly shift toward the center. The evolution of positions of the first four nodes with d is shown as the dashed curve in Figure 3.11(b). Back to Figures 3.8, both $\tilde{d}_c$ and $\tilde{d}_1$ slightly fluctuate with T. We illustrate more details in finite temperature regime in Figure 3.9. We find that the nodal structure is robust against finite temperature effects. Within the superfluid phase, regions with different numbers of nodes in $\Delta(z)$ are indicated. We note that the transition temperature T_c in the spatially-modulated phase is of the same order as in the fully balanced ($d = 0$) case. The non-monotonic behavior of T_c as a function of d agrees with the heuristic BCS-based LDA analysis.

3.3.5 Experimental measures

In the last subsection, we numerically show that the partially-polarized phase is associated with the FFLO state displaying oscillatory pairing. In this subsection, we discuss another measure in the local density of states, which also implies the oscillatory pairing, and a direct measure of the pairing profile, the pair momentum distribution function. We present the corresponding signatures for the FFLO state.

First we discuss the experimental measure the local density of states, or equivalently its integral with

respect to energy, the local number of states below energy E, $N(E,\mathbf{r})$, which separately counts the two components of the quasi-particle wave functions. We justify the expression by recovering the normal state $N(E,\mathbf{r})$ when the gap function is zero. We plot $N(E,z)$ for the 1D spin-split trap system and discuss the signatures for the oscillatory pairing phase.

The $N(E,\mathbf{r})$ is written as

$$N(E,\mathbf{r}) = \int_{-\mu}^{E} d\epsilon \sum_{n>0,\sigma} \left[|u_{n,\sigma}(\mathbf{r})|^2 \delta(\epsilon - \epsilon_{n,\sigma}) + |v_{n,-\sigma}(\mathbf{r})|^2 \delta(\epsilon + \epsilon_{n,\sigma}) \right] \tag{3.54}$$

Here we sum over only positive n. Let's check if we can recover the normal state DoS from Eq. (3.54). The normal state has solutions satisfying

$$(H-\mu)\phi_n = \tilde{\epsilon}_n \phi_n, \tag{3.55}$$

where we label positive $\tilde{\epsilon}_n$ with $n = 1, 2, 3...$ and negative $\tilde{\epsilon}_n$ with $n = -1, -2, -3$ in the order that $\tilde{\epsilon}_n < \tilde{\epsilon}_m$ if $n < m$. $N(E,\mathbf{r})$ of the normal state is

$$N_n(E,\mathbf{r}) = \int_{-\mu}^{E} d\epsilon \sum_{\text{all } n} |\phi_n(\mathbf{r})|^2 \delta(\epsilon - \tilde{\epsilon}_n) \tag{3.56}$$

For the normal state we don't have $\tilde{\epsilon}_{-n} = -\tilde{\epsilon}_n$, so the DoS doesn't have symmetry around μ.

Now considering the BdG equation in the normal state limit $\Delta \to 0$, we have

$$\begin{pmatrix} H-\mu & 0 \\ 0 & -(H-\mu) \end{pmatrix} \begin{pmatrix} u_n \\ v_n \end{pmatrix} = \epsilon_n \begin{pmatrix} u_n \\ v_n \end{pmatrix} \tag{3.57}$$

Comparing Eq. (3.57) with Eq. (3.55), we can write down the eigen functions and eigen energies as

$$\begin{pmatrix} u \\ v \end{pmatrix} = \begin{pmatrix} \phi_m \\ 0 \end{pmatrix}, \text{ with } \epsilon = \tilde{\epsilon}_m \tag{3.58}$$

and

$$\begin{pmatrix} u \\ v \end{pmatrix} = \begin{pmatrix} 0 \\ \phi_m \end{pmatrix}, \text{ with } \epsilon = -\tilde{\epsilon}_m \tag{3.59}$$

Because $\pm\tilde{\epsilon}_m$ are both eigenvalues for Eq. (3.57), if we label ϵ_n in the same way as we do for Eq. (3.55), we do have the symmetry $\epsilon_{-n} = -\epsilon_n$ here. Substituting Eq. (3.58) and Eq. (3.59) into Eq. (3.54), we have

$$\begin{aligned} N_n(E,\mathbf{r}) &= \int_{-\mu}^{E} d\epsilon \sum_{n>0} |u_n(\mathbf{r})|^2 \delta(\epsilon-\epsilon_n) + \sum_{n>0} |v_n(\mathbf{r})|^2 \delta(\epsilon+\epsilon_n) \\ &= \int_{-\mu}^{E} d\epsilon \sum_{m>0} |\phi_m(\mathbf{r})|^2 \delta(\epsilon-\tilde{\epsilon}_m) + \sum_{m<0} |\phi_m(\mathbf{r})|^2 \delta(\epsilon-\tilde{\epsilon}_m) = \int_{-\mu}^{E} d\epsilon \sum_{\text{all } m} |\phi_m(\mathbf{r})|^2 \delta(\epsilon-\tilde{\epsilon}_m) \end{aligned} \tag{3.60}$$

Here we drop the spin subscript for convenience. Finally we return to Eq. (3.56). Therefore in the quasi-particle basis it is correct to sum over only positive n for DoS, just as we do for other physical quantities. Even if the BdG equation gives symmetric eigen values, the DoS can be asymmetric due to the asymmetric weight from u and v in the positive n regime.

Let's keep simplifying Eq. (3.54) for the spin dependent superfluid state. Applying the time-reversal symmetry $(\epsilon_{n\downarrow}, u_{n\downarrow}, v_{n\uparrow}) = (-\epsilon_{-n\uparrow}, v^*_{-n\downarrow}, -u^*_{-n\uparrow})$, we have the relation

$$\begin{aligned} &\sum_{n>0} \Big[|u_{n\downarrow}(\mathbf{r})|^2 \delta(\epsilon-\epsilon_{n\downarrow}) + |v_{n\uparrow}(\mathbf{r})|^2 \delta(\epsilon+\epsilon_{n\downarrow}) \Big] = \sum_{n>0} \Big[|v_{-n\downarrow}(\mathbf{r})|^2 \delta(\epsilon+\epsilon_{-n\uparrow}) + |u_{-n\uparrow}(\mathbf{r})|^2 \delta(\epsilon-\epsilon_{-n\uparrow}) \Big] \\ = &\sum_{n<0} \Big[|v_{n\downarrow}(\mathbf{r})|^2 \delta(\epsilon+\epsilon_{n\uparrow}) + |u_{n\uparrow}(\mathbf{r})|^2 \delta(\epsilon-\epsilon_{n\uparrow}) \Big] \end{aligned} \tag{3.61}$$

Eq. (3.54) becomes

$$\begin{aligned} &N(E,\mathbf{r}) = \int_{-\mu}^{E} d\epsilon \sum_{n>0} \Big[|u_{n\uparrow}(\mathbf{r})|^2 \delta(\epsilon-\epsilon_{n\uparrow}) + |v_{n\downarrow}(\mathbf{r})|^2 \delta(\epsilon+\epsilon_{n\uparrow}) + |u_{n\downarrow}(\mathbf{r})|^2 \delta(\epsilon-\epsilon_{n\downarrow}) + |v_{n\uparrow}(\mathbf{r})|^2 \delta(\epsilon+\epsilon_{n\downarrow}) \Big] \\ = &\int_{-\mu}^{E} d\epsilon \sum_{n>0} \Big[|u_{n\uparrow}(\mathbf{r})|^2 \delta(\epsilon-\epsilon_{n\uparrow}) + |v_{n\downarrow}(\mathbf{r})|^2 \delta(\epsilon+\epsilon_{n\uparrow}) \Big] + \sum_{n<0} \Big[|v_{n\downarrow}(\mathbf{r})|^2 \delta(\epsilon+\epsilon_{n\uparrow}) + |u_{n\uparrow}(\mathbf{r})|^2 \delta(\epsilon-\epsilon_{n\uparrow}) \Big] \\ = &\int_{-\mu}^{E} d\epsilon \sum_{\text{all } n} \Big[|u_{n\uparrow}(\mathbf{r})|^2 \delta(\epsilon-\epsilon_{n\uparrow}) + |v_{n\downarrow}(\mathbf{r})|^2 \delta(\epsilon+\epsilon_{n\uparrow}) \Big] \end{aligned} \tag{3.62}$$

That is the equation we use in numerical calculations. Figure 3.10 shows the local number of state function $N(E,z)$ for the spin-split-trap system with the separation $d = 0.28R_z$. The down panels are $N(E,z)$ with the position z marked as the dashed red line in the up panels, which also display the gap function and imbalance profile. In Panel (a), corresponding to the center of the trap, the local imbalance is zero (fully-paired), and $N(E,z)$ has a plateau in $0.5 < E/\mu < 1.5$, which means a gap in the interval, like the fully-paired BCS state. In Panel (b), where the local imbalance is not zero but small, $N(E,z)$ still has a plateau but in a

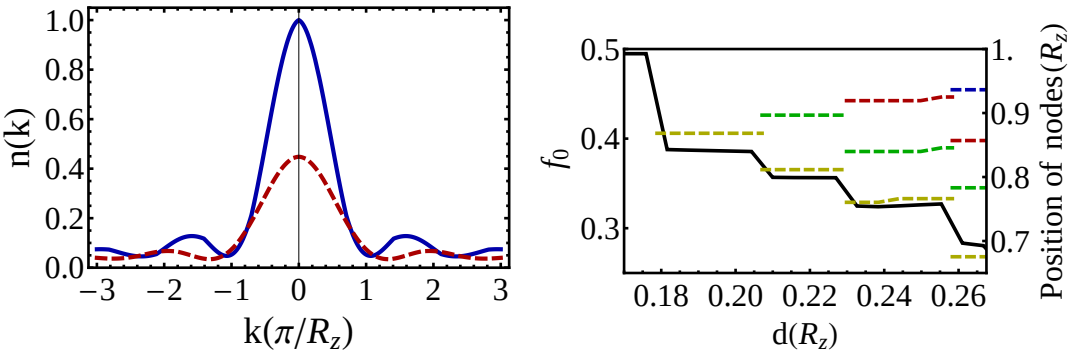

(a) (b)

Figure 3.11: (a) Momentum distribution $n(k)$ for parameters $d = 0$ (solid blue curve) and $d = 0.25R_z$ (dashed red curve). (b) Fraction of pairs (f_0) within the central peak shown in panel (a) (solid curve; axis on left-hand side of graph) and positions of the first four nodes (dashed curves; axis on right-hand side of graph) vs separation d.

narrower energy interval. Panel (c) shows the data at the position of a node in the partially polarized region. We can see that $N(E, z)$ has two jumps at $E/\mu = 0.5$ and 1.5 and another flat region in $E/\mu > 1.5$. This signature indicates a two-peak and two-gap structure of the density of state ($\partial N(E, z)/\partial E$), similar to the signature for the uniform FFLO system reflecting two different Fermi surfaces for each species. In Panel (d), which corresponds to the local maximum of Δ in the partially polarized region, the two-peak and two-gap structure is obscured. The detailed relations between the local density of states and the local properties of the gap and imbalance are a direction for future studies.

Now we switch gears to a direct measure of the pairing profile, the pair momentum distribution, which is calculated from the pair one-particle density matrix given by

$$\begin{aligned}\rho(\mathbf{r},\mathbf{r}') &= \langle\psi^\dagger_\uparrow(\mathbf{r})\psi^\dagger_\downarrow(\mathbf{r})\psi_\downarrow(\mathbf{r}')\psi_\uparrow(\mathbf{r}')\rangle \\ &= \langle\psi^\dagger_\uparrow(\mathbf{r})\psi^\dagger_\downarrow(\mathbf{r})\rangle\langle\psi_\downarrow(\mathbf{r}')\psi_\uparrow(\mathbf{r}')\rangle - \langle\psi^\dagger_\uparrow(\mathbf{r})\psi_\downarrow(\mathbf{r}')\rangle\langle\psi^\dagger_\downarrow(\mathbf{r})\psi_\uparrow(\mathbf{r}')\rangle + \langle\psi^\dagger_\uparrow(\mathbf{r})\psi_\uparrow(\mathbf{r}')\rangle\langle\psi^\dagger_\downarrow(\mathbf{r})\psi_\downarrow(\mathbf{r}')\rangle, \quad (3.63)\end{aligned}$$

where

$$\begin{aligned}\langle\psi^\dagger_\uparrow(\mathbf{r})\psi^\dagger_\downarrow(\mathbf{r})\rangle\langle\psi_\downarrow(\mathbf{r}')\psi_\uparrow(\mathbf{r}')\rangle &= \Delta^*(\mathbf{r})\Delta(\mathbf{r}')/g^2, \\ \langle\psi^\dagger_\uparrow(\mathbf{r})\psi_\downarrow(\mathbf{r}')\rangle\langle\psi^\dagger_\downarrow(\mathbf{r})\psi_\uparrow(\mathbf{r}')\rangle &= 0, \\ \langle\psi^\dagger_\uparrow(\mathbf{r})\psi_\uparrow(\mathbf{r}')\rangle\langle\psi^\dagger_\downarrow(\mathbf{r})\psi_\downarrow(\mathbf{r}')\rangle &= \sum_{m,n>0}\left\{u^*_{m\uparrow}(\mathbf{r})u_{m\uparrow}(\mathbf{r}')f(\epsilon_{m\uparrow}) + v_{m\uparrow}(\mathbf{r})v^*_{m\uparrow}(\mathbf{r}')[1-f(\epsilon_{m\downarrow})]\right\} \\ &\times \left\{u^*_{n\downarrow}(\mathbf{r})u_{n\downarrow}(\mathbf{r}')f(\epsilon_{n\downarrow}) + v_{n\downarrow}(\mathbf{r})v^*_{n\downarrow}(\mathbf{r}')[1-f(\epsilon_{n\uparrow})]\right\}. \quad (3.64)\end{aligned}$$

Applying the time-reversal correspondence $(\epsilon_{n\downarrow}, u_{n\downarrow}, v_{n\uparrow}) = (-\epsilon_{-n\uparrow}, v^*_{-n\downarrow}, -u^*_{-n\uparrow})$, finally we have

$$\rho(\mathbf{r},\mathbf{r}') = \Delta^*(\mathbf{r})\Delta(\mathbf{r}')/g^2 + \sum_{\text{all } m,n} u^*_{m\uparrow}(\mathbf{r})u_{m\uparrow}(\mathbf{r}')f(\epsilon_{m\uparrow})v_{n\downarrow}(\mathbf{r})v^*_{n\downarrow}(\mathbf{r}')[1-f(\epsilon_{n\uparrow})] \tag{3.65}$$

The pair momentum distribution function $n(\mathbf{k})$ is defined as

$$n(\mathbf{k}) = \int d\mathbf{r}d\mathbf{r}' e^{i\mathbf{k}\cdot(\mathbf{r}-\mathbf{r}')}\rho(\mathbf{r},\mathbf{r}'). \tag{3.66}$$

If we define the density matrix operator for one pair, $\hat{\rho}$, as its spatial representation being

$$\langle \mathbf{r}|\, \hat{\rho}\, |\mathbf{r}'\rangle \equiv \rho(\mathbf{r},\mathbf{r}'), \tag{3.67}$$

then $n(\mathbf{k})$ is the diagonal matrix element in $\mathbf{k}$ representation. We get an equivalent equation of Eq.(3.66) as

$$n(\mathbf{k}) = \langle \mathbf{k}|\, \hat{\rho}\, |\mathbf{k}\rangle = \int d\mathbf{r}d\mathbf{r}' \langle \mathbf{k} \mid \mathbf{r}\rangle \langle \mathbf{r}|\, \hat{\rho}\, |\mathbf{r}'\rangle \langle \mathbf{r}' \mid \mathbf{k}\rangle . \tag{3.68}$$

Now we extend the idea to define the off-diagonal terms in k space as

$$n(\mathbf{k},\mathbf{k}') \equiv \langle \mathbf{k}|\, \hat{\rho}\, |\mathbf{k}'\rangle . \tag{3.69}$$

From Eq.(3.63) and Eq.(3.69), the gap function and the number density distributions are related to the density matrix elements in $\mathbf{k}$ space as

$$\begin{aligned} & \rho(\mathbf{r},\mathbf{r}) = \int d\mathbf{k}d\mathbf{k}' \langle \mathbf{r} \mid \mathbf{k}\rangle \langle \mathbf{k}|\, \hat{\rho}\, |\mathbf{k}'\rangle \langle \mathbf{k}' \mid \mathbf{r}\rangle \\ \Rightarrow \quad & |\Delta(\mathbf{r})|^2/g^2 + \rho_\uparrow(\mathbf{r})\rho_\downarrow(\mathbf{r}) = \int d\mathbf{k}d\mathbf{k}' e^{ir\cdot(\mathbf{k}-\mathbf{k}')} n(\mathbf{k},\mathbf{k}'). \end{aligned} \tag{3.70}$$

It is known that $\rho_{\uparrow,\downarrow}$ and $n(\mathbf{k},\mathbf{k})$ $(= n(\mathbf{k}))$ are measurable in experiments [127, 128]. In the homogeneous case, the off-diagonal elements $n(\mathbf{k},\mathbf{k}')$ is zero due to translational invariance. The FFLO phase is characterized by a peak in $n(k)$ at nonzero k representing the characteristic spin-imbalance dependent wave vector of the FFLO state [111, 114]. In the trapped system, if $n(\mathbf{k},\mathbf{k}' \neq \mathbf{k})$ is also measurable, we could get the gap function from Eq. (3.70). However, even if we can only measure the diagonal elements, the profile has a discontinuous change when a node the the gap function emerges, which indicates the FFLO state.

In the 1D spin-split-trap system, typical plots of $n(k)$ are shown in Figure 3.11(a) for the cases of $d < d_c$ (uniform) and $d > d_c$ (modulated). Due to the spatial inhomogeneity of the imbalance h, the system does

not possess a characteristic wave vector for $n(k)$. However, $n(k)$ shows a sudden change in distribution with separation as Cooper pairs are shifted to higher momenta. As shown in Figure 3.11(b), the weight under the central peak suddenly decreases each time a new node appears in $\Delta(z)$. Thus, $n(k)$ displays a striking signature of modulated phases.

3.4 Outlook

In summary, we have proposed the easily tunable spin-split trap system in 1D as a candidate for realizing the FFLO phase. We studied the system from several perspectives and showed that the system can exhibit three phases concurrently and in the partially polarized phase the gap function is oscillatory and exhibits a nodal structure. It is of great interests to compare our results with those from techniques amenable to rigorous analysis in 1D, such as density matrix renormalization group and quantum Monte-Carlo methods which would give a quantitatively accurate description. The author's future research would extend the current study to higher dimensions. In experiments, the gas is trapped in a cigar-shaped geometry. The 1d condition is fulfilled when the aspect ratio of the longitudinal trapping frequency to the transverse one is small enough that particles barely occupy the excited states in the transverse direction. Since the FFLO state is stable in a larger parameter range in 1d than 3d, it would be interesting to investigate the evolution of the pairing amplitude with increasing aspect ratio, during which the system undergoes a crossover from 1d to 3d. If FFLO state finally disappears, a critical value of the aspect ratio would be expected. Another approach toward higher dimensional phenomenon is to couple several of these spin-split 1D systems in the transverse direction. By introducing tunneling and interacting effects between these individual 1D systems we can investigate the nature of ensuing phases.

Chapter 4

Transport properties in superconductor-ferromagnetic-metal hybrids

In this chapter, we study the electronic transport properties of superconductor-ferromagnetic-metal (S/F) hybrid systems. Such a system has multiple spatially separated phases, but unlike the cold atomic cases, they are made by artificially combining different materials together. However, the interfaces between the coexisting phases display interesting electronic transport effects. Our goal is to study these effects to explain recent experimental results from the group of Madalina O'hara and Dale Van Harlingen at UIUC. Their results show opposite trends in relative resistance compared to those at another experimental group. Previous theoretical studies have explained the trend of the other group's measurement but can not explain the opposite trend. In order to understand the mystery, we build a theoretical model with degrees of freedom that depend on the S/F interface properties. Our model can exhibit different trends in different parameter regimes. We specify the regimes in which Madalina and Dale's results are well described. Our findings imply that the samples of the two groups may have different interface properties. Below are a brief introduction to the physics in the hybrid system and the organization of this chapter.

To understand the trends of resistance in the hybrid system, we employ the Blonder-Tinkham-Klapwijk (BTK) model [129], deriving conducting properties across the junction. In the BTK treatment, charge is carried by electrons for a simple superconductor-normal-metal (S/N) hybrid, and holes (or strictly speaking, quasi-particles and quasi-holes of a Landau Fermi liquid) in the normal metal and by Bogoliugov quasi-particles in the superconductor. The S/N interface is modeled as a δ-function potential up to a strength parameter. The problem is simplified as a case of 1D quantum scattering through a delta potential. By matching the wave functions of electrons and holes in the normal region with the wave functions of quasi-particles in the superconducting region at the interface, we can obtain the scattering amplitudes for all possible scattering processes, as illustrated in Figure 4.1, and hence are able to calculate the current as a function of these amplitudes. A special scattering process, called Andreev reflection (AR, the hole reflection in Figure 4.1), describes an incident electron in the normal region with reflection of a hole of opposite spin in the normal region and transmission of a Cooper pair in the superconducting region [130]. AR only exists in the presence of a superconducting state and plays an important role in transport properties, especially

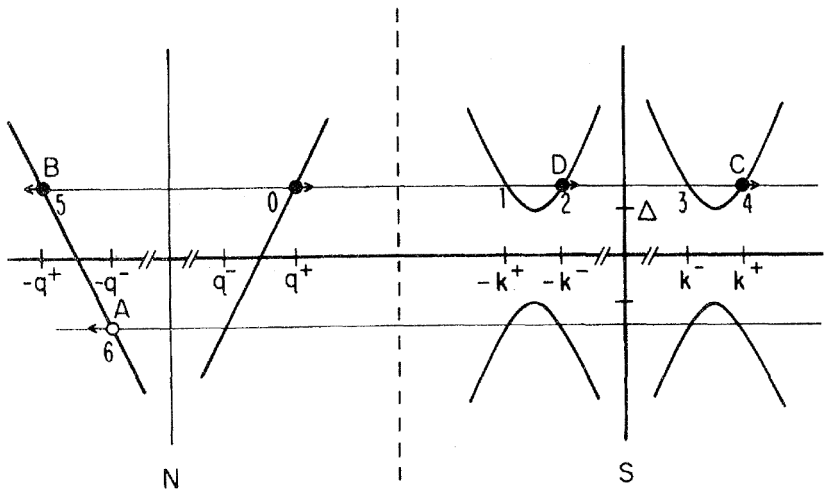

Figure 4.1: (Reproduced from Ref. [129]) Energy-momentum spectrum at a superconductor (Left)/normal metal (Right) junction. A typical scattering wave function is a combination of an incident electron (0) in the normal region, electron (5) and hole (6) reflections in the normal region, and electron-like (4) and hole-like (2) quasi-particle transmissions in the superconducting region, with corresponding amplitudes B, A, C, and D, respectively.

when voltage across the junction is smaller than the superconducting gap. The BTK model well describes various phenomena and trends in a hybrid system, such as Josephson effects, Andreev bound states, the sub-gap structure, and re-entrance effects [131, 132, 133, 134, 135, 136, 137].

Recent studies have turned to the hybrid system in which two N or F wires are connected to a S electrode with distance between the two junctions smaller than the superconducting coherence length [138, 139, 140]. Such a system has additional crossed processes like crossed Andreev reflection (CAR) and crossed normal reflection (CNR, or elastic co-tunneling, EC), in which the incidence of an electron from one wire into the superconductor is accompanied with reflection of a hole with opposite spin (in CAR) or an electron with the same spin (in CNR) into the other wire [141, 142, 143]. In addition, magnetization of the two F wires can be induced parallel or anti-parallel. Recent experiments have studied transport properties of the S/FF/S hybrids [144, 145] in which two F wires, made of ferromagnetic metallic materials, are both laid across two S electrodes made of BCS s-wave superconducting materials, with the separation between the two wires smaller than the superconducting coherence length, and with the separation between the two S electrodes on the order of the electronic phase coherence length in the ferromagnet, as shown in Figure 4.2. A series of measurement have been performed on resistance cross the two S electrodes in samples with the F wires of various material, size, and magnetization. With the other conditions unchanged relative resistance between parallel and anti-parallel alignment of magnetization of the F wires exhibits qualitative difference

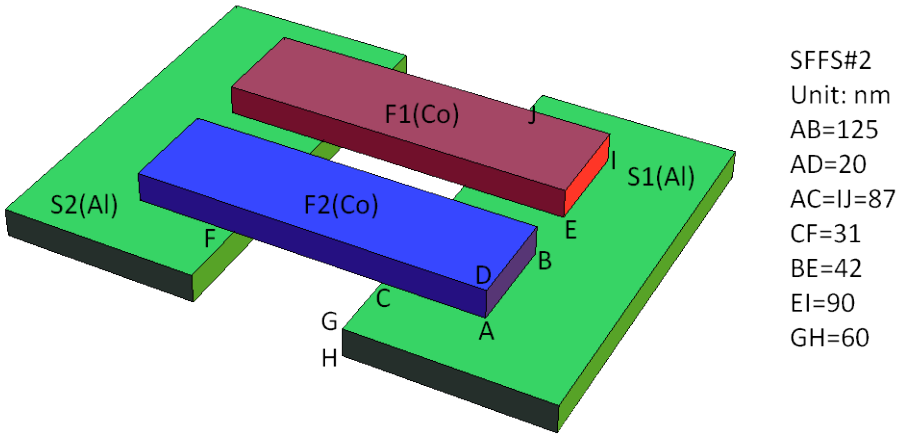

Figure 4.2: Geometry of a S/FF/S hybrid. The system is composed of two aluminum (Al) electrodes in superconducting state and two cobalt (Co) wires in ferromagnetic normal state. The right column show sizes in nanometers of a sample in Ref. [145].

from sample to sample. We define the normalized resistance difference as

$$\delta R \equiv \frac{R_{\rm ap} - R_{\rm p}}{(R_{\rm ap} + R_{\rm p})/2}, \tag{4.1}$$

where $R_{\rm p}$ and $R_{\rm ap}$ are the resistance of the parallel and anti-parallel configurations, respectively. Negative δR means that the system with anti-parallelly magnetized F wires has lower resistance, while positive δR means the opposite.

An intuitive theoretical consideration would expect negative δR. In an simple S/F junction, magnetization in F region reduces available hole states of minor species and hence suppresses AR. It is easy to understand an extreme case in which AR is completely suppressed when F is fully-polarized (a half metal), because there is no minor species accommodating the reflecting hole in AR. In other words, incoming major species would be blocked from transferring to the the S region and accumulate around the interface. In the S/FF/S junction of the parallel state, given the two F wires both fully-polarized, the AR and CAR are both completely suppressed, as is the S/F junction. However, in the anti-parallel case, CAR would not be suppressed because opposite spin species in the two wires become a counterpart of each other participating in CAR. Therefore, the anti-parallel state is supposed to have lower resistance than the parallel state. In fact, the experiment of Ref. [144] shows $\delta R < 0$ at low temperature (Figure 4.3(a)). A detailed theoretical explanation has been made associated with spin accumulation effects [146], with which the major spins accumulate more around the interface of the parallel state than the anti-parallel state and increase relative resistance. However, the experiment of Madalina O'Hara and Dale Van Harlingen shows an opposite result [145], $\delta R > 0$ (Figure 4.3(b)), with the physics still being a mystery.

In this chapter, we would like to explain both experimental results with one physical picture, in which the sign of δR depends on the property of the S/F interface, which is affected by alignment of magnetization. In fact, the dependence of resistance on orientations of magnetization of the two F wires implies spin-dependent transport processes through the interface. An S/F interface can lead to different interfacial phase shifts between electrons with spin parallel (major species) and anti-parallel (minor species) to the magnetization of the ferromagnet [147, 148, 149]. We find that in the BTK theory the spin-dependent phase shift can be parameterized by properly modeling the interfacial potential. Similar treatment has been discussed for an S/F/S junction [150] and the interface between an half-metal and a superconductor [151]. In our model, relative phase shift between regular and crossed processes causes interference, which is reflected in the coefficients of the scattering wave function. For example, the AR and CAR processes of an incident electron can have the corresponding Cooper pairs of different amplitudes and phases shown as the dashed arrows in Fig. 4.4. The current as well as the resistance are altered by such interference and hence to be a function of interfacial parameters and orientations of magnetization. We find that in small magnetization regime, the interference effect can overcome the suppression of CAR due to magnetization and lead to a positive δR, exhibiting similar trends observed Madalina and Dale's experiment.

In Section 4.1, we propose a scenario for theoretical calculations. We write down related parameters for the system, with an assumption of a magnetized interface potential with spin-dependent strength $Z_{M(m)}$ for the major (minor) electron species in F wires. We discuss the effects of $Z_{M(m)}$ on resistivity and their possible microscopic mechanisms. In Section 4.2, we apply a modified BTK model, incorporating a magnetized S/F interface, to calculate the current as a function of those parameters. In Section 4.3, we show the numerical results of δR as a function of interface parameters $Z_{M(m)}$, the Zeeman energy h in the F wires, and temperature, and compare them with the experimental results.

4.1 The system with spin-dependent interface

In experiments, the two S electrodes are not correlated because no super current is measured across the F wires. The resistance is thus separately contributed by the SFF junctions on each side. We consider two dimensional configuration of a SFF junction shown in Figure 4.4. The S electrode of width W_S is located in the $x > 0$ half plane, while the two F wires ($F1$ and $F2$), of widths W_{F1} and W_{F2} respectively, are located in the $x < 0$ half plane and separated by L in y direction. The exchange energy $h_{\rm ex}$, which exists only in $F1$ and $F2$ regions, and the gap function Δ, which exists only in S region, are represented by the step function

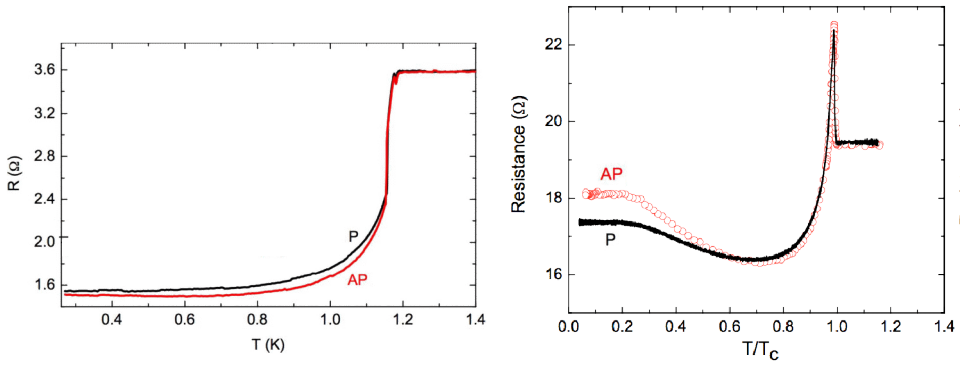

(a) (b)

Figure 4.3: Two experimental results show opposite signs in δR in low temperature regime. (a) (reproduced from Ref. [144]) shows $\delta R < 0$ ($R_{\rm AP} < R_{\rm P}$), while (b) (reproduced from Ref. [145]) shows $\delta R > 0$ ($R_{\rm AP} > R_{\rm P}$). Here P/AP mean the parallel/anti-parallel alignment of magnetization of the two F wires.

Θ as

$$h_{ex}(\mathbf{r}) = \Theta(-x)[h_1\eta_{F1}(y) + h_2\eta_{F2}(y)] \tag{4.2}$$

$$\Delta(\mathbf{r}) = \Theta(x)\eta_S(y), \tag{4.3}$$

where

$$\eta_{F1(F2)}(y) \equiv \Theta(\frac{W_{F1(F2)}}{2} - \left|y \mp \frac{L}{2}\right|)$$
$$\eta_S(y) \equiv \Theta(\frac{W_S}{2} - |y|). \tag{4.4}$$

The interface potential V_I of the system is of the form of a δ-function with spin-dependent strength,

$$V_I(\mathbf{r}) = \delta(x)[Z_{1\sigma}\eta_{F1}(y) + Z_{2\sigma}\eta_{F2}(y)]. \tag{4.5}$$

We assume that the major (minor) spin species in each F wire are subject to interface potential strengths $Z_{M(m)}$. Given that the major species in $F1$ is spin-up, we have

$$Z_{1\uparrow} = Z_{2\uparrow(\downarrow)} = Z_M$$
$$Z_{1\downarrow} = Z_{2\downarrow(\uparrow)} = Z_m \tag{4.6}$$

for the parallel (anti-parallel) cases.

We consider a small voltage difference $V < \Delta$ between the $x < 0$ and $x > 0$ regions, as applied in the

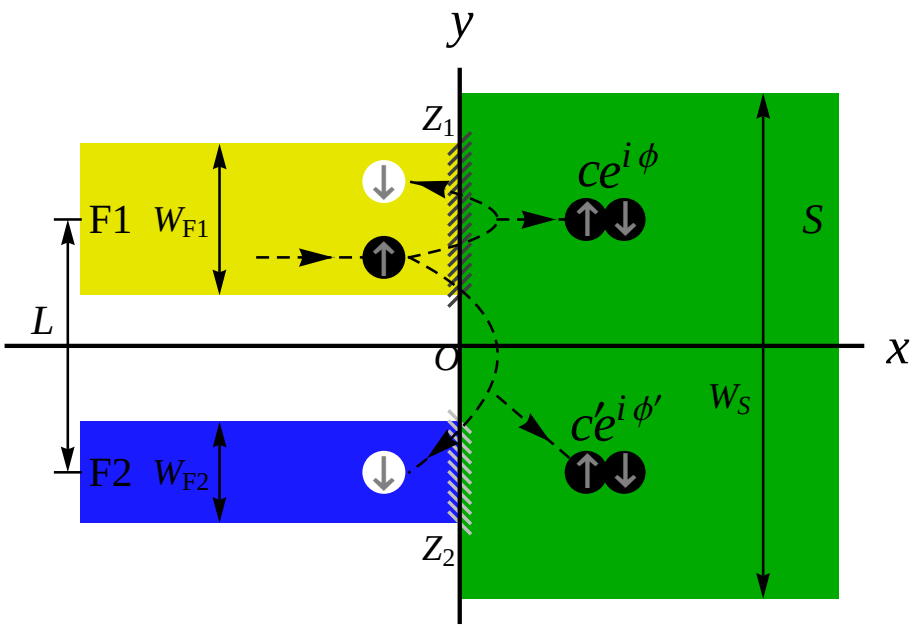

Figure 4.4: The SFF system and spin-dependent processes inside. The system has two ferro-magnetic wires $F1/2$, illustrated as the shaded regions in the second/third quadrant with width $W_{F1/2}$ and separation L between them, and a superconducting electrode, S, illustrated as the shaded region in the $x > 0$ plane with width W_S. The dashed arrows indicate the AR and CAR processes of an incident spin-up electron (black disk in $F1$), which involve reflection of spin down holes (white disks) and transmission of Cooper pairs (black disk pairs in S). The scattering Cooper pairs from AR and CAR have different amplitudes and phases depending on the spin-dependent interface parameters Z_1 and Z_2, respectively. Interference of the wave functions contributes to the charge current through the system, which is thus associated with the spin-dependent parameters.

experiment. Following the BTK treatment [129, 152], we compute probability currents for the regular normal reflection (NR), regular Andreev reflection (AR), elastic co-tunneling (or crossed normal reflection, CNR) and crossed Andreev reflection (CAR), and finally obtain the total current I as a function $I(V, T, \Delta, h_{ex}, Z_M, Z_m)$. The resistance is given by V/I. Detailed calculations are presented in Section 4.2.

A magnetized barrier possessing non-magnetic and magnetic potential strengths, g and Z, has been studied in an SFS junction [150], with Z being the original potential in the BTK model and g proportional to the barrier magnetization. In our system, we assume the S/F interface is magnetized and directly obtain the potential strength by definition,

$$Z_{M(m)} = Z \pm g \tag{4.7}$$

If $g = 0$, we have $Z_M = Z_m = Z$ and return to the original BTK assumption.

We notice that in the original BTK model for one interface, the scattering probability is always a function of Z^2, so a sign change of Z does not change the scattering physics and hence the total current. Therefore Z

can be chosen to be positive without loss of generality. Now our system has two interfaces, $F1/S$ and $F2/S$. Scattering wave functions through different interfaces may interfere with each other, depending on their magnitudes and relative phase, determined by the magnitude and sign of Z_1 and Z_2. Therefore both values and signs of Z_M and Z_m should be taken into account (parameters of the same magnitude but opposite signs are discussed in Ref. [151]). It is achievable by appropriately setting Z and g.

Figure 4.4 illustrates AR and CAR processes associated with spin-dependent scattering for an incident electron with spin up in $F1$. The wave function in the S region is a combination state of two Cooper pairs from AR and CAR respectively. The total current is thus affected by interference between the two pair wave functions. In our system, the parallel and anti-parallel cases have different interference, which causes δR to vary in sign and value.

In previous works on the magnetized interface, a semi-classical theory was applied to derive boundary conditions for spin-active interfaces [147], and find that An S/F interface can lead to different interfacial phase shifts between electrons with spin parallel (major species) and anti-parallel (minor species) to the magnetization of the ferromagnet [148, 149]. We find that in the BTK theory the spin-dependent phase shift can be parameterized by setting $Z = 0$ and $g \neq 0$, which leads to $Z_M = -Z_m = g$. Here we see that the opposite sign between Z_M and Z_m is a natural choice for such a case.

Here we discuss three possible microscopic mechanisms affecting the parameters Z and g. (1) Cleanness of the barrier equivalently influences the scattering of spin-up and spin-down particles, so it contributes to $|Z|$. (2) There is non-zero constant magnetic field in the F regions and no magnetic field in the S region, so there must be a large field gradient at the interface. With the presence of non-zero magnetic field gradient, a spin will feel a force, which is proportional to the spin times the gradient. If the spin up feels an attractive force from the interface, then the spin down feels a repulsive force, and vice versa. Therefore different spins are subject to potentials of opposite signs. As a result, the field gradient contributes to $|g|$. (3) The spin accumulation of major species at the interface will increases the field gradient and hence $|g|$. However, it also causes charge accumulation which repulses both spin up and down particles and hence increases $|Z|$.

4.2 BTK treatment

In this section, we present detailed calculations for the total current. We write down the scattering wave functions satisfying the BdG equation and boundary conditions. We solve for the amplitudes and probability currents for each processes and finally compute the current by summing the probability currents over all scattering channels and energies weighed by the Fermi distribution function.

We begin with the BdG Hamiltonian,

$$H = \begin{pmatrix} -\frac{\hbar^2}{2m}\nabla^2 + h_{\rm ex} + V_{I\uparrow} & \Delta \\ \Delta^* & -(-\frac{\hbar^2}{2m}\nabla^2 - h_{\rm ex} + V_{I\downarrow}) \end{pmatrix}, \tag{4.8}$$

where the elements are given in Eq. (4.2), (4.3), and (4.5). The solution in the S region is written as

$$\begin{aligned} \Psi_{\pm k_l^+}(\mathbf{r}) &= \begin{pmatrix} u_0 \\ v_0 \end{pmatrix} e^{\pm i k_l^+ x} \Phi_{S,l}(y) \\ \Psi_{\pm k_l^-}(\mathbf{r}) &= \begin{pmatrix} v_0 \\ u_0 \end{pmatrix} e^{\pm i k_l^- x} \Phi_{S,l}(y), \end{aligned} \tag{4.9}$$

with

$$u_0^2 = 1 - v_0^2 = \frac{1}{2}\left(1 + \sqrt{1 - \frac{\Delta^2}{E^2}}\right) \tag{4.10}$$

and

$$\Phi_{S,l}(y) = \sqrt{\frac{2}{W_S}} \sin l\pi \left(\frac{y}{W_S} + \frac{1}{2}\right) \eta_S(y). \tag{4.11}$$

Here $k^{\pm}$ are the wave vectors for the particle-like (hole-like) wave functions in x direction. Integer l defines the quantum mode (or channel) in y direction. We use μ_F and k_F^{-1} be the energy and length units. The eigenvalue of the l mode is

$$E_l = \left(\frac{l\pi}{W_S}\right)^2. \tag{4.12}$$

The wave vectors are

$$k_l^{\pm} = \sqrt{1 \pm \sqrt{E^2 - \Delta^2} - E_l}. \tag{4.13}$$

In the $F1$ ($F2$) regions, the solutions are

$$\Psi_{\pm p(q)_{\sigma,l}^+}(\mathbf{r}) = \begin{pmatrix} 1 \\ 0 \end{pmatrix} e^{\pm i p(q)_{\sigma,l}^+ x} \Phi_{F1(F2),l}(y)$$

$$\Psi_{\pm p(q)^-_{\sigma,l}}(\mathbf{r}) = \begin{pmatrix} 0 \\ 1 \end{pmatrix} e^{\pm ip(q)^-_{\sigma,l}x}\Phi_{F1(F2),l}(y), \tag{4.14}$$

with

$$\Phi_{F1(F2),l}(y) = \sqrt{\frac{2}{W_{F1(F2)}}}\sin l\pi\left(\frac{y \mp L/2}{W_{F1(F2)}} + \frac{1}{2}\right)\eta_{F1(F2)}(y). \tag{4.15}$$

We have the spin index σ in the normal region. The eigenvalues in y direction and the wave vectors in x direction are

$$\begin{aligned} E_{F1(F2),l} &= \left(\frac{l\pi}{W_{F1(F2)}}\right)^2 \\ p(q)^{\pm}_{\sigma,l} &= \sqrt{1 \pm (E + \sigma h_{1(2)}) - E_{F1(F2),l}} \end{aligned} \tag{4.16}$$

Considering the elastic scattering of an incident electron of spin σ and channel n from $F1$ to S, we have six processes including regular Andreev and normal reflections in $F1$ region, crossed Andreev and normal reflections in $F2$ region, and particle-like and hole-like transmissions in S region, with amplitudes a, b, c, d, α, and β respectively. The outgoing wave functions in F regions are combinations of all possible propagating modes, which have real wave vectors. In a steady system, the particles do not scatter into the bound states, which have complex wave vectors. In S region, the wave function is sum over all modes, because a quasi particle finally decays into the condensate and leaves an unoccupied state for incident particles to come in. In numerical calculations, we let the highest mode in S region be M_s and increase M_s until the results converge. We write down the wave functions in each region,

$$\begin{aligned} \Psi_{F1}(\mathbf{r}) &= \begin{pmatrix} 1 \\ 0 \end{pmatrix} e^{ip^+_{\sigma,n}x}\Phi_{F1,n}(y) + \sum_{l=1}^{M_a} a_{\sigma,ln}\begin{pmatrix} 0 \\ 1 \end{pmatrix} e^{ip^-_{\sigma,l}x}\Phi_{F1,l}(y) + \sum_{l=1}^{M_b} b_{\sigma,ln}\begin{pmatrix} 1 \\ 0 \end{pmatrix} e^{-ip^+_{\sigma,l}x}\Phi_{F1,l}(y) \\ \Psi_{F2}(\mathbf{r}) &= \sum_{l=1}^{M_c} c_{\sigma,ln}\begin{pmatrix} 0 \\ 1 \end{pmatrix} e^{iq^-_{\sigma,l}x}\Phi_{F2,l}(y) + \sum_{l=1}^{M_d} d_{\sigma,ln}\begin{pmatrix} 1 \\ 0 \end{pmatrix} e^{-iq^+_{\sigma,l}x}\Phi_{F2,l}(y) \\ \Psi_{S}(\mathbf{r}) &= \sum_{l=1}^{M_s}\left[\alpha_{\sigma,ln}\begin{pmatrix} u_0 \\ v_0 \end{pmatrix} e^{ik^+_l x} + \beta_{\sigma,ln}\begin{pmatrix} v_0 \\ u_0 \end{pmatrix} e^{-ik^-_l x}\right]\Phi_{S,l}(y), \end{aligned} \tag{4.17}$$

where $M_{a,b,c,d}$ are the highest propagating modes in corresponding processes. The boundary conditions at

$x = 0$ are

$$\Psi_{F1}(0,y)\eta_{F1}(y) + \Psi_{F2}(0,y)\eta_{F2}(y) = \Psi_S(0,y)\eta_S(y) \tag{4.18}$$

$$\partial_x[\Psi_S\eta_S(y) - \Psi_{F1}\eta_{F1}(y) - \Psi_{F2}\eta_{F2}(y)]_{x=0} = Z_{1\sigma}\Psi_{F1}(0,y)\eta_{F1}(y) + Z_{2\sigma}\Psi_{F2}(0,y)\eta_{F2}(y). \tag{4.19}$$

The probability current of a Nambu wave function $\begin{pmatrix} \psi_1 \\ \psi_2 \end{pmatrix}$ is defined as

$$J = \frac{\hbar}{m}(\psi_1^*\nabla\psi_1 - \psi_2^*\nabla\psi_2). \tag{4.20}$$

The currents of the wave functions in Eq.(4.17) have no y component. We calculate probability currents on the interface ($x = 0$) for the incoming wave and each scattering process as

$$\begin{aligned}
J^{\rm inc}_{\sigma,n} &= \frac{\hbar}{m}p^+_{\sigma,n}\int dy[\Phi_{F1,n}(y)]^2 = \frac{\hbar}{m}p^+_{\sigma,n} \\
J^a_{\sigma,n} &= \frac{\hbar}{m}\sum_{l,l'=1}^{M_a}{\rm Im}[a^*_{\sigma,l'n}a_{\sigma,ln}ip^-_{\sigma,l}]\int dy\Phi_{F1,l'}(y)\Phi_{F1,l}(y) = \frac{\hbar}{m}\sum_{l=1}^{M_a}|a_{\sigma,ln}|^2{\rm Re}[p^-_{\sigma,l}] \\
J^b_{\sigma,n} &= -\frac{\hbar}{m}\sum_{l=1}^{M_b}|b_{\sigma,ln}|^2{\rm Re}[p^+_{\sigma,l}] \\
J^c_{\sigma,n} &= \frac{\hbar}{m}\sum_{l=1}^{M_c}|c_{\sigma,ln}|^2{\rm Re}[q^-_{\sigma,l}] \\
J^d_{\sigma,n} &= -\frac{\hbar}{m}\sum_{l=1}^{M_d}|d_{\sigma,ln}|^2{\rm Re}[q^+_{\sigma,l}] \\
J^{\alpha(\beta)}_{\sigma,n} &= \frac{\hbar}{m}\sum_{l=1}^{M_s}\left|\alpha(\beta)_{\sigma,ln}\right|^2(|u_0|^2 - |v_0|^2){\rm Re}[k_l^{+(-)}]
\end{aligned} \tag{4.21}$$

The balance between the incoming and outgoing wave functions shows

$$\left(\left|J^a_{\sigma,n}\right| + \left|J^b_{\sigma,n}\right| + \left|J^c_{\sigma,n}\right| + \left|J^d_{\sigma,n}\right| + \left|J^\alpha_{\sigma,n}\right| + \left|J^\beta_{\sigma,n}\right|\right)/\left|J^{\rm inc}_{\sigma,n}\right| = 1. \tag{4.22}$$

We substitute Eq.(4.17) into Eq.(4.18) and (4.19), separate the particle and hole components, and project it into the channel m in the S region.

$$\Lambda^1_{nm} + \sum_{l=1}^{M_b}\Lambda^1_{lm}b_{\sigma,ln} + \sum_{l=1}^{M_d}\Lambda^2_{lm}d_{\sigma,ln} = u_0\alpha_{\sigma,mn} + v_0\beta_{\sigma,mn}, \tag{4.23}$$

$$\sum_{l=1}^{M_a}\Lambda^1_{lm}a_{\sigma,ln} + \sum_{l=1}^{M_c}\Lambda^2_{lm}c_{\sigma,ln} = v_0\alpha_{\sigma,mn} + u_0\beta_{\sigma,mn}, \tag{4.24}$$

where

$$\Lambda^{1(2)}_{lm} = \int dy \Phi_{F1(F2),l}(y)\Phi_{S,m}(y). \tag{4.25}$$

Similarly, we substitute Eq.(4.17) into Eq.(4.19) and project it into the channel m in the $F1$ and $F2$ region.

$$\begin{aligned}
(p^+_{\sigma,n} - iZ_{1\sigma})\delta_{mn} - (p^+_{\sigma,m} + iZ_{1\sigma})b_{\sigma,mn} &= \sum_{l=1}^{M_s} \Lambda^1_{m,l}(k^+_l u_0 \alpha_{\sigma,ln} - k^-_l v_0 \beta_{\sigma,ln}), &(4.26)\\
(p^-_{\sigma,m} - iZ_{1\sigma})a_{\sigma,mn} &= \sum_{l=1}^{M_s} \Lambda^1_{ml}(k^+_l v_0 \alpha_{\sigma,ln} - k^-_l u_0 \beta_{\sigma,ln}), &(4.27)\\
-(q^+_{\sigma,m} + iZ_{2\sigma})d_{\sigma,mn} &= \sum_{l=1}^{M_s} \Lambda^2_{ml}(k^+_l u_0 \alpha_{\sigma,ln} - k^-_l v_0 \beta_{\sigma,ln}), &(4.28)\\
(q^-_{\sigma,m} - iZ_{2\sigma})c_{\sigma,mn} &= \sum_{l=1}^{M_s} \Lambda^2_{ml}(k^+_l v_0 \alpha_{\sigma,ln} - k^-_l u_0 \beta_{\sigma,ln}). &(4.29)
\end{aligned}$$

If we let m go from 1 to M_s in Eq. (4.23) and (4.24), and to M_b, M_a, M_d, and M_c in Eq. (4.26-4.29) respectively, we obtain a linear equation with dimension $(M_a + M_b + M_c + M_d + 2M_s)$ to solve for all amplitudes.

Given the incoming population with spin σ in channel n in $F1$ being

$$f^{1,e}_{\sigma,n,\rightarrow}(E) = f_0(E - eV), \tag{4.30}$$

the outgoing population is

$$\begin{aligned}
f^{1,e}_{\sigma,n,\leftarrow}(E) &= \left(\sum_{l=1}^{M_a} \frac{p^-_{\sigma,l}}{p^+_{\sigma,n}}|a_{\sigma,ln}|^2 + \sum_{l=1}^{M_c} \frac{q^-_{\sigma,l}}{p^+_{\sigma,n}}|c_{\sigma,ln}|^2\right)[1 - f_\rightarrow(-E)] \\
&+ \left(\sum_{l=1}^{M_b} \frac{p^+_{\sigma,l}}{p^+_{\sigma,n}}|b_{\sigma,ln}|^2 + \sum_{l=1}^{M_d} \frac{q^+_{\sigma,l}}{p^+_{\sigma,n}}|d_{\sigma,ln}|^2\right) f_\rightarrow(E) \\
&+ \sum_{l=1}^{M_s}\left(\frac{\mathrm{Re}[k^+_{\sigma,l}]}{p^+_{\sigma,n}}|\alpha_{\sigma,ln}|^2 + \frac{\mathrm{Re}[k^-_{\sigma,l}]}{p^+_{\sigma,n}}|\beta_{\sigma,ln}|^2\right)(|u_0|^2 - |v_0|^2) f_0(E)
\end{aligned} \tag{4.31}$$

We use the conservation relation of Eq.(4.22)

$$\sum_{l=1}^{M_s}\left(\frac{\mathrm{Re}[k^+_{\sigma,l}]}{p^+_{\sigma,n}}|\alpha_{\sigma,ln}|^2 + \frac{\mathrm{Re}[k^-_{\sigma,l}]}{p^+_{\sigma,n}}|\beta_{\sigma,ln}|^2\right)(|u_0|^2 - |v_0|^2)$$

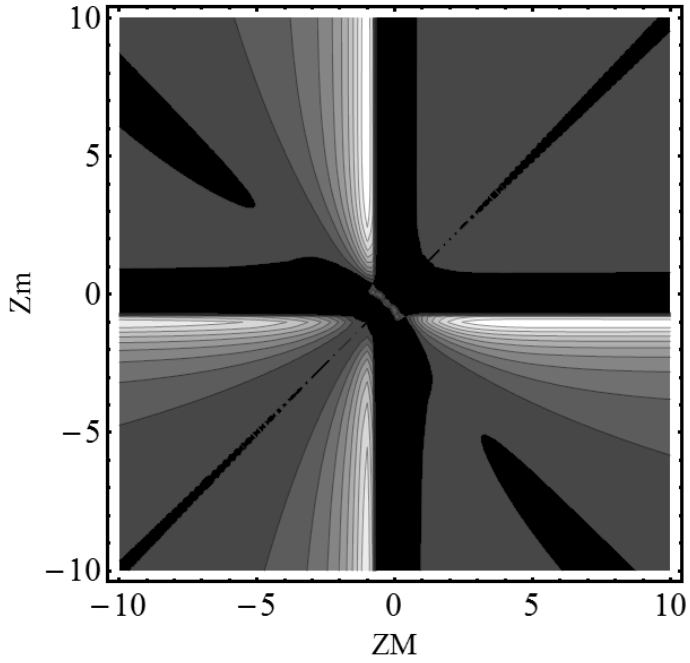

Figure 4.5: Contour plot of δR in the plane of Z_M and Z_m. The black region corresponds to $\delta R < 0$, while the dark gray one corresponds to $\delta R \sim 0$. The largest value appears to be $\delta R = 0.0083$ at $(Z_M, Z_m) = (-1, 5.6)$.

$$= 1 - \sum_{l=1}^{M_a} \frac{p^-_{\sigma,l}}{p^+_{\sigma,n}} |a_{\sigma,ln}|^2 - \sum_{l=1}^{M_c} \frac{q^-_{\sigma,l}}{p^+_{\sigma,n}} |c_{\sigma,ln}|^2 - \sum_{l=1}^{M_b} \frac{p^+_{\sigma,l}}{p^+_{\sigma,n}} |b_{\sigma,ln}|^2 - \sum_{l=1}^{M_d} \frac{q^+_{\sigma,l}}{p^+_{\sigma,n}} |d_{\sigma,ln}|^2 \tag{4.32}$$

and

$$1 - f_{\rightarrow}(-E) = 1 - f_0(-E - eV) = f_0(E + eV) \tag{4.33}$$

to simplify the outgoing population. Finally we obtain the current contributed by the incident electron with σ spin in $F1$ as

$$\begin{aligned} I^{1,e}_{\sigma}(T) &= \frac{e}{h} \int_0^{\infty} dE \sum_{n=1}^{M_b} [f^{1,e}_{\sigma,n,\rightarrow}(E) - f^{1,e}_{\sigma,n,\leftarrow}(E)] \\ &= \frac{e}{h} \int_0^{\infty} dE \sum_{n=1}^{M_b} \left(\sum_{l=1}^{M_a} \frac{p^-_{\sigma,l}}{p^+_{\sigma,n}} |a_{\sigma,ln}|^2 + \sum_{l=1}^{M_c} \frac{q^-_{\sigma,l}}{p^+_{\sigma,n}} |c_{\sigma,ln}|^2 \right) [f_0(E) - f_0(E + eV)] \\ &\quad + \left(1 - \sum_{l=1}^{M_b} \frac{p^+_{\sigma,l}}{p^+_{\sigma,n}} |b_{\sigma,ln}|^2 - \sum_{l=1}^{M_d} \frac{q^+_{\sigma,l}}{p^+_{\sigma,n}} |d_{\sigma,ln}|^2 \right) [f_0(E - eV) - f_0(E)]. \end{aligned} \tag{4.34}$$

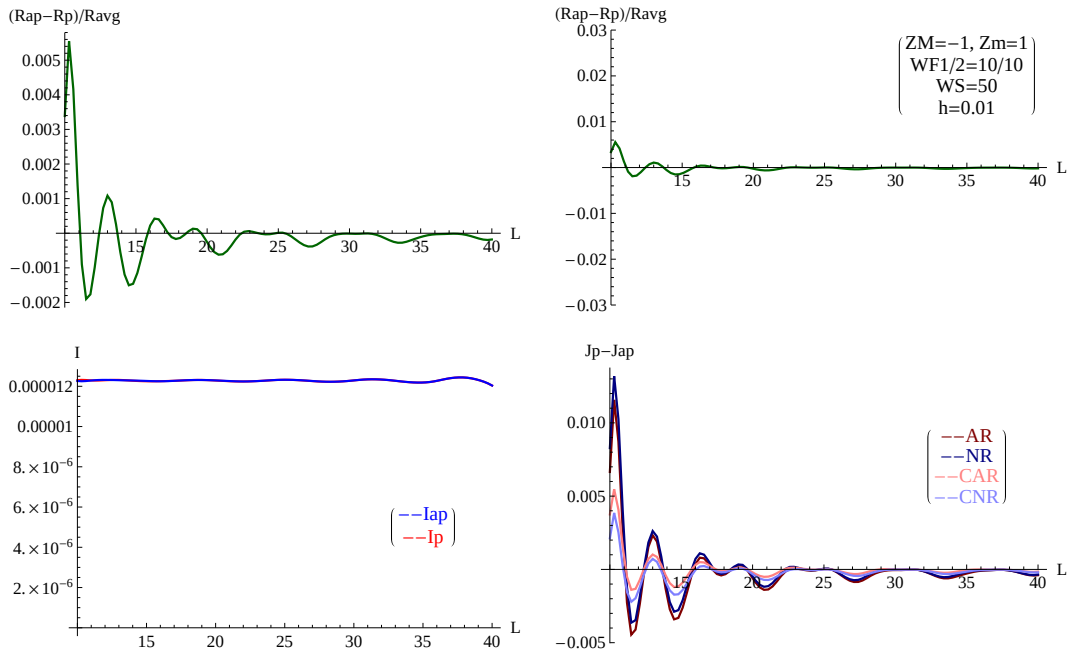

Figure 4.6: Up left and right: δR vs the separation between two F sires L in the most appropriate scale and the experimental scale in Ref. [145], respectively. The inset shows other fixed parameters of the system. Down left: total current of anti-parallel (red) and parallel (blue) cases. Down right: probability currents difference between the parallel and anti-parallel cases ($J_p - J_{ap}$) for AR (darker red), NR (darker blue), CAR(lighter red), and CNR (lighter blue) processes.

At zero temperature,

$$I_\sigma^{1,e}(0) = \frac{e}{h}\int_0^{eV} dE \sum_{n=1}^{M_b}\left(1 - \sum_{l=1}^{M_b}\frac{p^+_{\sigma,l}}{p^+_{\sigma,n}}|b_{\sigma,ln}|^2 - \sum_{l=1}^{M_d}\frac{q^+_{\sigma,l}}{p^+_{\sigma,n}}|d_{\sigma,ln}|^2\right). \tag{4.35}$$

Considering the incident hole with spin σ in channel n in $F1$, we write the equations of the amplitudes as

$$\sum_{l=1}^{M_b}\Lambda^1_{lm}b_{\sigma,ln} + \sum_{l=1}^{M_d}\Lambda^2_{lm}d_{\sigma,ln} = u_0\alpha_{\sigma,mn} + v_0\beta_{\sigma,mn} \tag{4.36}$$

$$\Lambda^1_{nm} + \sum_{l=1}^{M_a}\Lambda^1_{lm}a_{\sigma,ln} + \sum_{l=1}^{M_c}\Lambda^2_{lm}c_{\sigma,ln} = v_0\alpha_{\sigma,mn} + u_0\beta_{\sigma,mn} \tag{4.37}$$

$$-(p^+_{\sigma,m} + iZ_{1\sigma})b_{\sigma,mn} = \sum_{l=1}^{M_s}\Lambda^1_{ml}(k^+_l u_0\alpha_{\sigma,ln} - k^-_l v_0\beta_{\sigma,ln}) \tag{4.38}$$

$$(-p^-_{\sigma,n} - iZ_{1\sigma})\delta_{mn} + (p^-_{\sigma,m} - iZ_{1\sigma})a_{\sigma,mn} = \sum_{l=1}^{M_s}\Lambda^1_{ml}(k^+_l v_0\alpha_{\sigma,ln} - k^-_l u_0\beta_{\sigma,ln}) \tag{4.39}$$

$$-(q^+_{\sigma,m} + iZ_{2\sigma})d_{\sigma,mn} = \sum_{l=1}^{M_s}\Lambda^2_{ml}(k^+_l u_0\alpha_{\sigma,ln} - k^-_l v_0\beta_{\sigma,ln}) \tag{4.40}$$

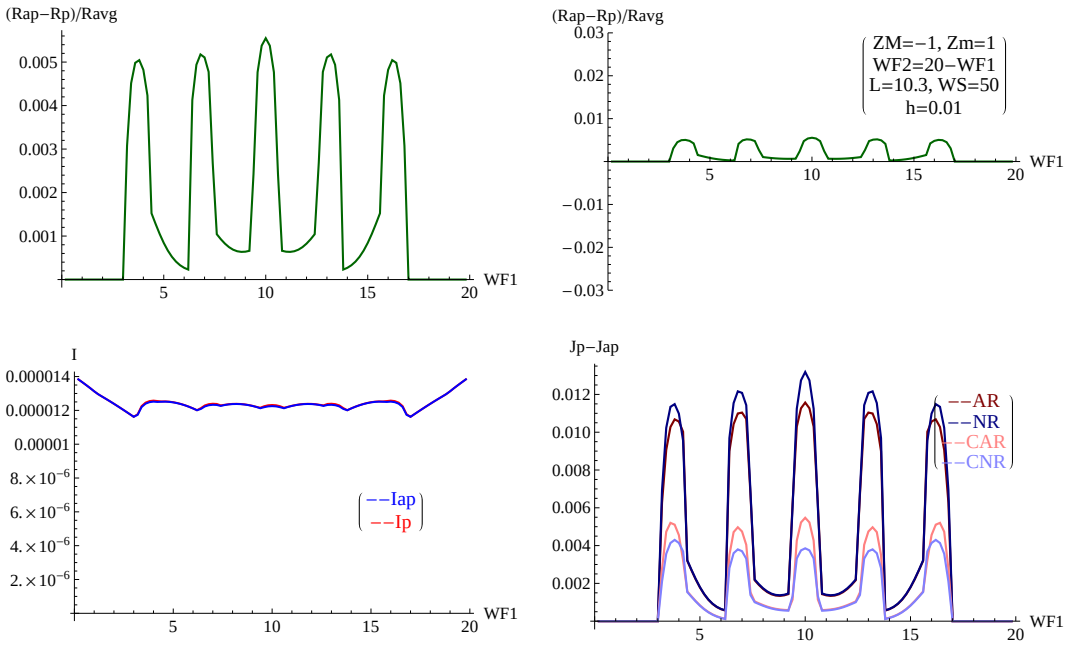

Figure 4.7: δR vs W_{F1}, with $W_{F1}+W_{F2}$ unchanged. All the panels are represented as in Figure 4.6.

$$(q^{-}_{\sigma,m} - iZ_{2\sigma})c_{\sigma,mn} = \sum_{l=1}^{M_s} \Lambda^2_{ml}(k^{+}_{l} v_0 \alpha_{\sigma,ln} - k^{-}_{l} u_0 \beta_{\sigma,ln}). \tag{4.41}$$

The current is

$$\begin{aligned} I^{1,h}_{\sigma}(T) &= \frac{e}{h}\int_0^{\infty} dE \sum_{n=1}^{M_a}\left(\sum_{l=1}^{M_b}\frac{p^{+}_{\sigma,l}}{p^{-}_{\sigma,n}}|b_{\sigma,ln}|^2 + \sum_{l=1}^{M_d}\frac{q^{+}_{\sigma,l}}{p^{-}_{\sigma,n}}|d_{\sigma,ln}|^2\right)[f_0(E-eV)-f_0(E)] \\ &\quad + \left(1 - \sum_{l=1}^{M_a}\frac{p^{-}_{\sigma,l}}{p^{-}_{\sigma,n}}|a_{\sigma,ln}|^2 - \sum_{l=1}^{M_c}\frac{q^{-}_{\sigma,l}}{p^{-}_{\sigma,n}}|c_{\sigma,ln}|^2\right)[f_0(E)-f_0(E+eV)] \end{aligned} \tag{4.42}$$

$$I^{1,h}_{\sigma}(0) = \frac{e}{h}\int_0^{eV} dE \sum_{n=1}^{M_a}\left(\sum_{l=1}^{M_b}\frac{p^{+}_{\sigma,l}}{p^{-}_{\sigma,n}}|b_{\sigma,ln}|^2 + \sum_{l=1}^{M_d}\frac{q^{+}_{\sigma,l}}{p^{-}_{\sigma,n}}|d_{\sigma,ln}|^2\right) \tag{4.43}$$

Similarly, we can obtain the current carried by electrons and holes in $F2$, $I^{2,e}_{\sigma}(T)$ and $I^{2,h}_{\sigma}(T)$. The total current is

$$I = \sum_{\sigma} I^{1,e}_{\sigma} + I^{1,h}_{\sigma} + I^{2,e}_{\sigma} + I^{2,h}_{\sigma} \tag{4.44}$$

Since the current is expressed only in amplitudes of a, b, c, d. In numerical calculations, we can significantly reduce variables of the linear equations by solving α and β first. Detailed calculations are left in Appendix A.

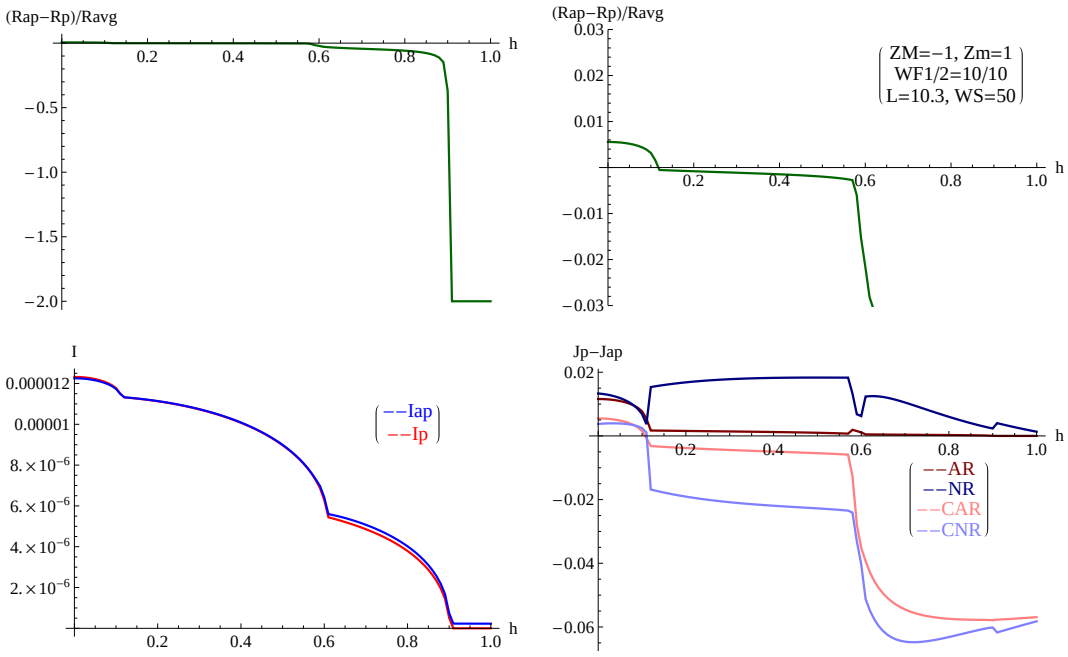

Figure 4.8: δR vs h, with all the panels are represented as in Figure 4.6.

4.3 Numerical results

In this section, we first present the numerical results for a system smaller than the real one at zero temperature. We plot $\delta R > 0$ as a function of the interface parameters, exchange energy, and the size of the system, and find the parameter regime to obtain positive δR comparable to the experiment of Ref. [145]. Then we calculate for a larger (more realistic) system and show the temperature dependence of δR, which fits the experimental results.

Figure 4.5 shows a contour plot of δR in the plane of Z_M and Z_m. The parameters of the system are $|h_1| = |h_2| = 0.01\mu_F$, $\Delta = 2 \times 10^{-4}\mu_F$, and $V = 0.01\Delta$, all of which are comparable to the experiment, and the sizes $W_{F1} = W_{F2} = L = 10/k_F$ and $W_S = 50/k_F$, an order smaller than the real system. The black region corresponds to $\delta R < 0$, while the dark gray one corresponds to $\delta R \sim 0$. The pattern has a mirror symmetry with respect to the line of $Z_M = Z_m$, which means δR is unchanged with exchange of Z_M and Z_m. We see that δR is either negative or quite small near the line of $Z_M = Z_m$ and in the region of $Z_M > 0$ and $Z_m > 0$. Large positive δR appears in the region where at least one of Z_M and Z_m is negative. The largest value is $\delta R = 0.0083$ at $(Z_M, Z_m) = (-1, 5.6)$, which corresponds to $Z = 2.3$ and $g = 3.3$. At $(Z_M, Z_m) = (-1, 1)$, or $(Z, g) = (0, -1)$ (pure magnetic barrier), we have 0.0032. Those δR's are comparable to the experimental order of 0.01 [145].

In Figure 4.6-4.8, we let $(Z_M, Z_m) = (-1, 1)$ and vary L, W_F, and h to see the trend of δR. The top

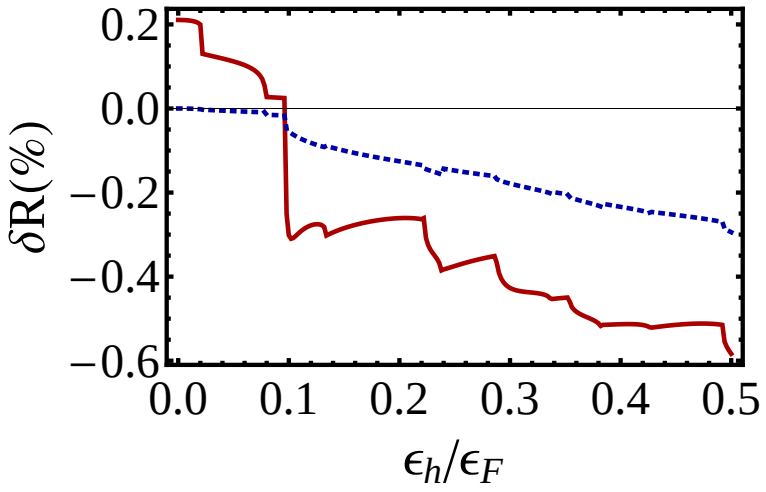

Figure 4.9: Relative resistance δR vs exchange energy ϵ_h of an SFF junction for spin-dependent (solid red curve) and spin-independent interfaces (dashed blue curve) at $T = 0$ and $|Z| = 0.35$. The other parameters are set as $W_{F1} = 54k_F^{-1}$, $W_{F2} = 36k_F^{-1}$, $L = 45k_F^{-1}$, $W_S = 180k_F^{-1}$, and $\Delta = 2 \times 10^{-4}\epsilon_F$.

left panel of each figure shows δR vs the variable of interests. The top right panel is the same curve of δR but of the experimental scale in Ref. [145], with an inset shows parameters we use for the system. The bottom left panel shows total current of anti-parallel (red) parallel (blue) cases. The bottom right panel shows probability currents difference between the parallel and anti-parallel cases ($J_p - J_{ap}$) for AR (darker red), NR (darker blue), CAR(lighter red), and CNR (lighter blue) processes. Sum of all processes should show the same behavior as δR.

Figure 4.6 shows δR is oscillatory between positive and negative values, with the oscillation amplitude decreasing with increase of L. The trend shows that the farer the two F wires separate from each other, the less they interfere with each other, so the difference between the parallel and anti-parallel cases gradually disappears. In Figure 4.7, we vary W_{F1} but keep $W_{F1} + W_{F2}$ unchanged to eliminate the effect of the total width. The δR curve is oscillatory but always positive with change of W_{F1}. The maximum value appears at $W_{F1} = W_{F2}$. Figure 4.8 shows δR vs the exchange field h. When $h \to 1$ (half metal), all Andreev reflections are suppressed in the parallel case, but the cross Andreev reflection (CAR) is sustained in the anti-parallel case. Therefore we have $I_p = 0$ and $I_{ap} > 0$, or equivalently $\delta R = -2$. Since $\delta R > 0$ at small h, we have a crossover point at which $\delta R = 0$. From the down left panel, we see that sudden drops in AR, CAR, and CNR are responsible for the sign change.

In Figure 4.9, we show comparison of δR as a function of exchange energy ϵ_h between the spin-dependent and spin-independent interfacial conditions in a larger (more realistic) system with $|Z| = 0.35$ at zero temperature. In the spin-independent case, the suppression of CAR in the parallel configuration causes δR being negative and monotonically decreasing in ϵ_h. In the spin-dependent case, however, the interference

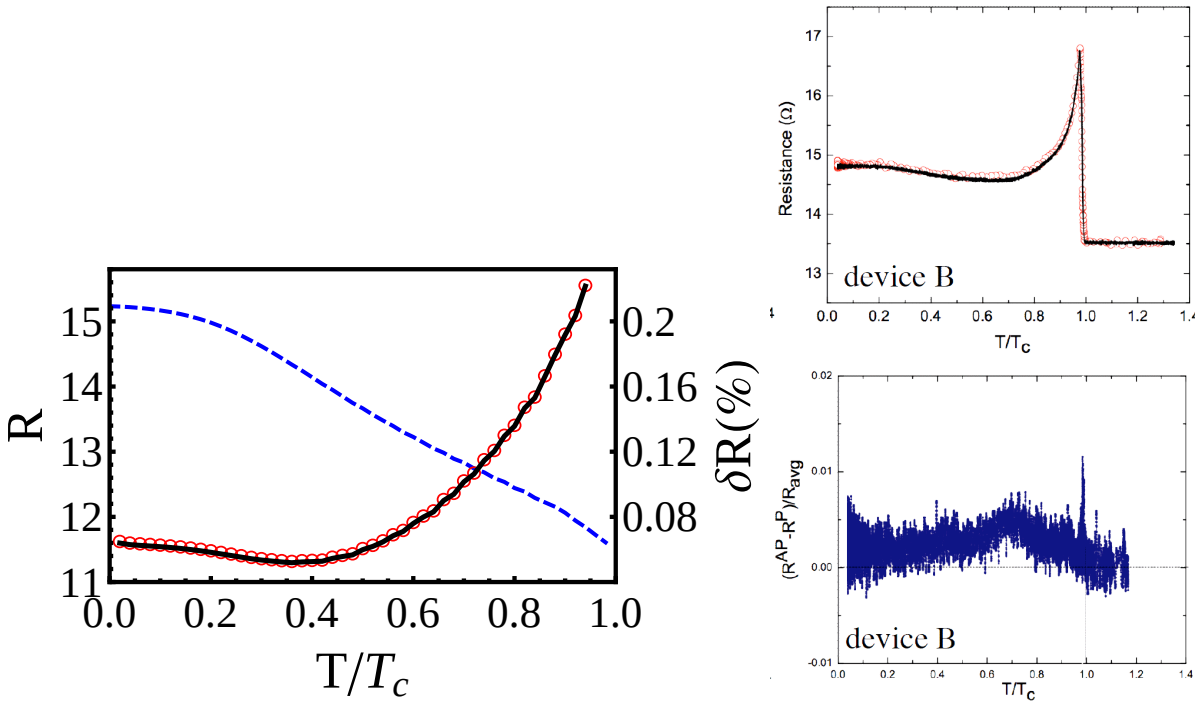

(a) (b)

Figure 4.10: (a)Resistance of the parallel and anti-parallel configurations (black solid curve and red circles, respectively; axis on left-hand side of graph) and δR (blue dashed curve; axis on right-hand side of graph) vs temperature. Here the interface is spin-dependent and the parameters are chosen the same as Figure 4.9. (b) The same plot from the experimental data (reproduced from Ref. [145]) for comparison.

effect can drive δR to be non-monotonic in ϵ_h and even to be positive at small ϵ_h, overcoming the suppression of CAR, although it finally goes negative with increase in ϵ_h when the suppression becomes stronger. Both δR curves have kinks at the same positions because number of scattering channels decreases by one at each kink. Our numerical calculation shows that the spin-dependent interface yields a significant parameter region in which the relative resistance $\delta R > 0$, while the spin-independent one does not due to the lack of the interference caused by the relative phase shift.

Finally, we plot the resistance vs temperature for spin-dependent barriers in Figure 4.10. Panel (a) shows the resistance curves of the parallel and anti-parallel cases and relative resistance between them. The non-monotonic behaviors of both curves indicate the re-entrant effect, which reduces the resistance due to increase in conducting states with increase in temperature, and suppression of AR and CAR due to depletion of the superconducting gap at $T \to T_c$. We see that δR is positive and slightly decreases with T, but does not change sign. Panel (b) is the same plot from the experimental results of Ref. [145]. As a results, our model, assuming spin-dependent barriers, faithfully captures the experimental features.

4.4 Outlook

In summary, we have applied a modified BTK model with spin-dependent interface parameters on an S/FF junction and well described the experimental measurement of Madalina and Dale [145], which shows the resistance of anti-parallel magnetization alignment of the two F wires higher than the parallel configuration. The author's future research lies in three directions. (1) We would like to extend the current study to more degrees of freedom. For example, besides the parallel and anti-parallel alignments, the magnetization of the two F wires can be in arbitrary directions. If the two directions are perpendicular to each other, the cross normal reflection and cross Andreev reflection are associated with a spin-flip process. A generalized BTK model for such magnetization and spin-flip processes is to be developed. (2) It is still an open question how a detailed interfacial structure determines the sign and value of the interfacial parameter Z. A self-consistent BdG calculation as we did for the atomic system in Chapter 3 can be performed to obtain the magnetic field and the gap function profile in proximity to the interface. Once the proximity effect is obtained, we could use more accurate potentials instead of a delta-function or step-function form to discuss relevant scattering processes. (3) The experiment shows that the curve of differential resistance vs. current displays peaks. Locations of these Andreev events and a quantitative description of them are to be studied.

Appendix A

Simplification for equations of scattering amplitudes

In Subcection 4.2, the linear equations of Eq. (4.23), (4.24), and (4.26-4.29) can be significantly simplified for a numerical purpose. We reduce variables α and β of by solving Eq. (4.23) and (4.24) first,

$$\begin{aligned}
\alpha_{\sigma,jn} &= \frac{1}{u_0^2 - v_0^2}[u_0(\Lambda^1_{nj} + \sum_{l=1}^{M_b}\Lambda^1_{lj}b_{\sigma,ln} + \sum_{l=1}^{M_d}\Lambda^2_{lj}d_{\sigma,ln}) - v_0(\sum_{l=1}^{M_a}\Lambda^1_{lj}a_{\sigma,ln} + \sum_{l=1}^{M_c}\Lambda^2_{lj}c_{\sigma,ln})] \\
\beta_{\sigma,jn} &= \frac{1}{u_0^2 - v_0^2}[-v_0(\Lambda^1_{nj} + \sum_{l=1}^{M_b}\Lambda^1_{lj}b_{\sigma,ln} + \sum_{l=1}^{M_d}\Lambda^2_{lj}d_{\sigma,ln}) + u_0(\sum_{l=1}^{M_a}\Lambda^1_{lj}a_{\sigma,ln} + \sum_{l=1}^{M_c}\Lambda^2_{lj}c_{\sigma,ln})]. \quad \text{(A.1)}
\end{aligned}$$

If we define

$$\Gamma^{\pm pq}_{mn} \equiv \sum_{j=1}^{M_s} k_j^{\pm}\Lambda^p_{mj}\Lambda^q_{nj}, \quad \text{(A.2)}$$

we have

$$\begin{aligned}
\sum_{j=1}^{M_s}\Lambda^1_{mj}k_j^{\pm}\alpha_{\sigma,jn} &= \frac{1}{u_0^2 - v_0^2}[u_0(\Gamma^{\pm 11}_{mn} + \sum_{l=1}^{M_b}\Gamma^{\pm 11}_{ml}b_{\sigma,ln} + \sum_{l=1}^{M_d}\Gamma^{\pm 12}_{ml}d_{\sigma,ln}) - v_0(\sum_{l=1}^{M_a}\Gamma^{\pm 11}_{ml}a_{\sigma,ln} + \sum_{l=1}^{M_c}\Gamma^{\pm 12}_{ml}c_{\sigma,ln})] \\
\sum_{j=1}^{M_s}\Lambda^1_{mj}k_j^{\pm}\beta_{\sigma,jn} &= \frac{1}{u_0^2 - v_0^2}[-v_0(\Gamma^{\pm 11}_{mn} + \sum_{l=1}^{M_b}\Gamma^{\pm 11}_{ml}b_{\sigma,ln} + \sum_{l=1}^{M_d}\Gamma^{\pm 12}_{ml}d_{\sigma,ln}) + u_0(\sum_{l=1}^{M_a}\Gamma^{\pm 11}_{ml}a_{\sigma,ln} + \sum_{l=1}^{M_c}\Gamma^{\pm 12}_{ml}c_{\sigma,ln})]
\end{aligned} \quad \text{(A.3)}$$

Substituting Eq. (A.3) into Eq. (4.26-4.29), we obtain

$$\begin{aligned}
&(p^-_{\sigma,m} - iZ_{1\sigma})a_{\sigma,mn} = \omega_3(\Gamma^{+11}_{mn} + \Gamma^{-11}_{mn}) - \sum_{l=1}^{M_a}(\omega_2\Gamma^{+11}_{ml} + \omega_1\Gamma^{-11}_{ml})a_{\sigma,ln} \\
&+ \sum_{l=1}^{M_b}\omega_3(\Gamma^{+11}_{ml} + \Gamma^{-11}_{ml})b_{\sigma,ln} - \sum_{l=1}^{M_c}(\omega_2\Gamma^{+12}_{ml} + \omega_1\Gamma^{-12}_{ml})c_{\sigma,ln} + \sum_{l=1}^{M_d}\omega_3(\Gamma^{+12}_{ml} + \Gamma^{-12}_{ml})d_{\sigma,ln}, \quad \text{(A.4)} \\
&(p^+_{\sigma,n} - iZ_{1\sigma})\delta_{mn} - (p^+_{\sigma,m} + iZ_{1\sigma})b_{\sigma,mn} = (\omega_1\Gamma^{+11}_{mn} + \omega_2\Gamma^{-11}_{mn}) - \sum_{l=1}^{M_a}\omega_3(\Gamma^{+11}_{ml} + \Gamma^{-11}_{ml})a_{\sigma,ln}
\end{aligned}$$

$$+\sum_{l=1}^{M_b}(\omega_1\Gamma^{+11}_{ml}+\omega_2\Gamma^{-11}_{ml})b_{\sigma,ln}-\sum_{l=1}^{M_c}\omega_3(\Gamma^{+12}_{ml}+\Gamma^{-12}_{ml})c_{\sigma,ln}+\sum_{l=1}^{M_d}(\omega_1\Gamma^{+12}_{ml}+\omega_2\Gamma^{-12}_{ml})d_{\sigma,ln}, \quad (A.5)$$

$$(q^-_{\sigma,m}-iZ_{2\sigma})c_{\sigma,mn}=\omega_3(\Gamma^{+21}_{mn}+\Gamma^{-21}_{mn})-\sum_{l=1}^{M_a}(\omega_2\Gamma^{+21}_{ml}+\omega_1\Gamma^{-21}_{ml})a_{\sigma,ln}$$
$$+\sum_{l=1}^{M_b}\omega_3(\Gamma^{+21}_{ml}+\Gamma^{-21}_{ml})b_{\sigma,ln}-\sum_{l=1}^{M_c}(\omega_2\Gamma^{+22}_{ml}+\omega_1\Gamma^{-22}_{ml})c_{\sigma,ln}+\sum_{l=1}^{M_d}\omega_3(\Gamma^{+22}_{ml}+\Gamma^{-22}_{ml})d_{\sigma,ln}, \quad (A.6)$$

$$-(q^+_{\sigma,m}+iZ_{2\sigma})d_{\sigma,mn}=(\omega_1\Gamma^{+21}_{mn}+\omega_2\Gamma^{-21}_{mn})-\sum_{l=1}^{M_a}\omega_3(\Gamma^{+21}_{ml}+\Gamma^{-21}_{ml})a_{\sigma,ln}$$
$$+\sum_{l=1}^{M_b}(\omega_1\Gamma^{+21}_{ml}+\omega_2\Gamma^{-21}_{ml})b_{\sigma,ln}-\sum_{l=1}^{M_c}\omega_3(\Gamma^{+22}_{ml}+\Gamma^{-22}_{ml})c_{\sigma,ln}+\sum_{l=1}^{M_d}(\omega_1\Gamma^{+22}_{ml}+\omega_2\Gamma^{-22}_{ml})d_{\sigma,ln}, \quad (A.7)$$

with

$$\omega_1=\frac{u_0^2}{u_0^2-v_0^2},\ \omega_2=\frac{v_0^2}{u_0^2-v_0^2},\ \omega_3=\frac{u_0v_0}{u_0^2-v_0^2}. \quad (A.8)$$

We let m goes from 1 to M_a, M_b, M_c, and M_d in Eq. (A.5-A.7) respectively and obtain a linear equation with dimension $(M_a+M_b+M_c+M_d)$, which has advantage in numerics when M_s is large. Similarly, for the hole case of Eq. (4.36-4.41), we have

$$(-p^-_{\sigma,n}-iZ_{1\sigma})\delta_{mn}+(p^-_{\sigma,m}-iZ_{1\sigma})a_{\sigma,mn}=-(\omega_2\Gamma^{+11}_{mn}+\omega_1\Gamma^{-11}_{mn})-\sum_{l=1}^{M_a}(\omega_2\Gamma^{+11}_{ml}+\omega_1\Gamma^{-11}_{ml})a_{\sigma,ln}$$
$$+\sum_{l=1}^{M_b}\omega_3(\Gamma^{+11}_{ml}+\Gamma^{-11}_{ml})b_{\sigma,ln}-\sum_{l=1}^{M_c}(\omega_2\Gamma^{+12}_{ml}+\omega_1\Gamma^{-12}_{ml})c_{\sigma,ln}+\sum_{l=1}^{M_d}\omega_3(\Gamma^{+12}_{ml}+\Gamma^{-12}_{ml})d_{\sigma,ln}, \quad (A.9)$$

$$-(p^+_{\sigma,m}+iZ_{1\sigma})b_{\sigma,mn}=-\omega_3(\Gamma^{+11}_{mn}+\Gamma^{-11}_{mn})-\sum_{l=1}^{M_a}\omega_3(\Gamma^{+11}_{ml}+\Gamma^{-11}_{ml})a_{\sigma,ln}$$
$$+\sum_{l=1}^{M_b}(\omega_1\Gamma^{+11}_{ml}+\omega_2\Gamma^{-11}_{ml})b_{\sigma,ln}-\sum_{l=1}^{M_c}\omega_3(\Gamma^{+12}_{ml}+\Gamma^{-12}_{ml})c_{\sigma,ln}+\sum_{l=1}^{M_d}(\omega_1\Gamma^{+12}_{ml}+\omega_2\Gamma^{-12}_{ml})d_{\sigma,ln}, \quad (A.10)$$

$$(q^-_{\sigma,m}-iZ_{2\sigma})c_{\sigma,mn}=-(\omega_2\Gamma^{+21}_{mn}+\omega_1\Gamma^{-21}_{mn})-\sum_{l=1}^{M_a}(\omega_2\Gamma^{+21}_{ml}+\omega_1\Gamma^{-21}_{ml})a_{\sigma,ln}$$
$$+\sum_{l=1}^{M_b}\omega_3(\Gamma^{+21}_{ml}+\Gamma^{-21}_{ml})b_{\sigma,ln}-\sum_{l=1}^{M_c}(\omega_2\Gamma^{+22}_{ml}+\omega_1\Gamma^{-22}_{ml})c_{\sigma,ln}+\sum_{l=1}^{M_d}\omega_3(\Gamma^{+22}_{ml}+\Gamma^{-22}_{ml})d_{\sigma,ln}, \quad (A.11)$$

$$-(q^+_{\sigma,m}+iZ_{2\sigma})d_{\sigma,mn}=-\omega_3(\Gamma^{+21}_{ml}+\Gamma^{-21}_{ml})-\sum_{l=1}^{M_a}\omega_3(\Gamma^{+21}_{ml}+\Gamma^{-21}_{ml})a_{\sigma,ln}$$
$$+\sum_{l=1}^{M_b}(\omega_1\Gamma^{+21}_{ml}+\omega_2\Gamma^{-21}_{ml})b_{\sigma,ln}-\sum_{l=1}^{M_c}\omega_3(\Gamma^{+22}_{ml}+\Gamma^{-22}_{ml})c_{\sigma,ln}+\sum_{l=1}^{M_d}(\omega_1\Gamma^{+22}_{ml}+\omega_2\Gamma^{-22}_{ml})d_{\sigma,ln} \quad (A.12)$$

References

[1] K. Sun, C. Lannert, and S. Vishveshwara, Phys. Rev. A **79**, 043422 (2009).

[2] K. Sun, J. S. Meyer, D. E. Sheehy, and S. Vishveshwara, preprint arXiv:1009.4476 (2010).

[3] A. Einstein, *Sitzungsberichte der Preussischen Akademie der Wissenschaften, Physikalisch-mathematische Klasse* (1924), p. 261; (1925), p. 3.

[4] A. J. Leggett, *Quantum Liquids*, 1st, ed. (Oxford University Press, Oxford, 2006).

[5] J. Bardeen, L. N. Cooper, and J. R. Schrieffer, Phys. Rev. **108**, 1175 (1957).

[6] M. H. Anderson, J. R. Ensher, M. R. Matthews, C. E. Wieman, and E. A. Cornell, Science **269**, 198 (1995).

[7] C. C. Bradley, C. A. Sackett, J. J. Tollett, and R. G. Hulet, Phys. Rev. Lett. **75**, 1687 (1995).

[8] K. B. Davis, M.-O. Mewes, M. R. Andrews, N. J. van Druten, D. S. Durfee, D. M. Kurn, and W. Ketterle, Phys. Rev. Lett. **75**, 3969 (1995).

[9] B. DeMarco and D. D. Jin, Science **285**, 1703 (1999).

[10] M. Greiner, Ph.D. thesis, Ludwig-Maximilians- Universitat Munchen(2003).

[11] D. Jaksch and P. Zoller, Annals of Physics **315**, 52 (2005).

[12] I. Bloch, J. Dalibard, and W. Zwerger, Rev. Mod. Phys. **80**, 885 (2008).

[13] C. Monroe, Nature **416**, 238 (2002).

[14] M. P. A. Fisher, P. B. Weichman, G. Grinstein, and D. S. Fisher, Phys. Rev. B **40**, 546 (1989).

[15] M. R. Andrews, C. G. Townsend, H.-J. Miesner, D. S. Durfee, D. M. Kurn, and W. Ketterle, Science **275**, 637 (1997).

[16] J. Stenger, S. Inouye, A. P. Chikkatur, D. M. Stamper-Kurn, D. E. Pritchard, and W. Ketterle, Phys. Rev. Lett. **82**, 4569 (1999).

[17] D. M. Harber, H. J. Lewandowski, J. M. McGuirk, and E. A. Cornell, Phys. Rev. A **66**, 053616 (2002).

[18] T. Stöferle, H. Moritz, C. Schori, M. Köhl, and T. Esslinger, Phys. Rev. Lett. **92**, 130403 (2004).

[19] I. B. Spielman, W. D. Phillips, and J. V. Porto, Phys. Rev. Lett. **98**, 080404 (2007).

[20] M. Greiner, O. Mandel, T. Esslinger, T. W. Hansch, and I. Bloch, Nature **415**, 39 (2002).

[21] N. Gemelke, X. Zhang, C.-L. Hung, and C. Chin, Nature **460**, 995 (2009).

[22] W. S. Bakr, J. I. Gillen, A. Peng, S. Fo̎lling, and M. Greiner, Nature **462**, 74 (2009).

[23] B. DeMarco, Science **329**, 523 (2010).

[24] W. S. Bakr, A. Peng, M. E. Tai, R. Ma, J. Simon, J. I. Gillen, S. Fölling, L. Pollet, and M. Greiner, Science **329**, 547 (2010).

[25] J. F. Sherson, C. Weitenberg, M. Endres, M. Cheneau, I. Bloch, and S. Kuhr, Nature **467**, 68 (2010).

[26] P. B. Blakie, and W.-X. Wang, Phys. Rev. A **76**, 053620 (2007).

[27] D. Jaksch, C. Bruder, J. I. Cirac, C. W. Gardiner, and P. Zoller, Phys. Rev. Lett. **81**, 3108 (1998).

[28] B. DeMarco, C. Lannert, S. Vishveshwara, and T.-C. Wei, Phys. Rev. A **71**, 063601 (2005).

[29] M. Yamashita and M. W. Jack, Phys. Rev. A **79**, 023609 (2009).

[30] D. van Oosten, P. van der Straten, and H. T. C. Stoof, Phys. Rev. A **63**, 053601 (2001).

[31] E. Taylor and E. Zaremba, Phys. Rev. A **68**, 053611 (2003).

[32] D. van Oosten, D. B. M. Dickerscheid, B. Farid, P. van der Straten, and H. T. C. Stoof, Phys. Rev. A **71**, 021601(R) (2005).

[33] K. Sengupta and N. Dupuis, Phys. Rev. A **71**, 033629 (2005).

[34] G. Pupillo, A. M. Rey, and G. G. Batrouni, Phys. Rev. A **74**, 013601 (2006).

[35] R. A. Barankov, C. Lannert, and S. Vishveshwara, Phys. Rev. A **75**, 063622 (2007).

[36] C. Menotti and N. Trivedi, Phys. Rev. B **77**, 235120 (2008).

[37] K. Mitra, C. J. Williams, and C. A. R. Sa de Melo, Phys. Rev. A **77**, 033607 (2008).

[38] G. K. Campbell, J. Mun, M. Boyd, P. Medley, A. E. Leanhardt, L. G. Marcassa, D. E. Pritchard, and W. Ketterle, Science **313**, 649 (2006).

[39] K. R. A. Hazzard and E. J. Mueller, Phys. Rev. A **76**, 063612 (2007).

[40] S. Folling, A. Widera, T. Muller, F. Gerbier, and I. Bloch, Phys. Rev. Lett. **97**, 060403 (2006).

[41] K. R. A. Hazzard and E. J. Mueller, Phys. Rev. A **81**, 033404 (2010).

[42] Y. Kato and N. Kawashima, Phys. Rev. E **79**, 021104 (2009).

[43] B. Capogrosso-Sansone, N. V. Prokof'ev and B. V. Svistunov, Phys. Rev. B **75**, 134302 (2007).

[44] M. Rigol, G. G. Batrouni, V. G. Rousseau, and R. T. Scalettar, Phys. Rev. A **79**, 053605 (2009).

[45] S. Ramanan, T. Mishra, M. S. Luthra, R. V. Pai, and B. P. Das, Phys. Rev. A **79**, 013625 (2009).

[46] K. Jimeèz-Garcìa, R. L. Compton, Y.-J. Lin, W. D. Phillips, J.V. Porto, and I. B. Spielman, Phys. Rev. Lett. **105**, 110401 (2010).

[47] L. D. Carr, M. L. Wall, D. G. Schirmer, R. C. Brown, J. E. Williams, and Charles W. Clark, Phys. Rev. A **81**, 013613 (2010).

[48] M. Campostrini and E. Vicari, Phys. Rev. A **81**, 063614 (2010).

[49] T. Roscilde, Phys. Rev. A **82**, 023601 (2010).

[50] D.-W. Wang, Phys. Rev. A **80**, 063620 (2009).

[51] S. Fang, R.-K. Lee, and D.-W. Wang, Phys. Rev. A **82**, 031601(R) (2010).

[52] J. N. Kupferschmidt and E. J. Mueller, Phys. Rev. A **82**, 023618 (2010).

[53] F. Gerbier, S. Trotzky, S. Fölling, U. Schnorrberger, J. D. Thompson, A. Widera, I. Bloch, L. Pollet, M. Troyer, B. Capogrosso-Sansone, N. V. Prokof'ev, and B. V. Svistunov, Phys. Rev. Lett. **101**, 155303 (2008).

[54] R. B. Diener, Q. Zhou, H. Zhai, and T.-L. Ho, Phys. Rev. Lett. **98**, 180404 (2007).

[55] Y. Kato, Q. Zhou, N. Kawashima, and N. Trivedi, Nature Phys. **4**, 617 (2008).

[56] S. Trotzky, L. Pollet, F. Gerbier, U. Schnorrberger, I. Bloch, N. V. Prokof'ev, B. Svistunov and M. Troyer, Nature Phys, (2010).

[57] A. Griffin, Nature Phys. **4**, 592 (2008).

[58] T.-L. Ho and Q. Zhou, Phys. Rev. Lett. **99**, 120404 (2007).

[59] L. Pollet, C. Kollath, K. Van Houcke, and M. Troyer, New Journal of Physics **10**, 065001 (2008)

[60] T.-L. Ho and Q. Zhou, Proceedings of the National Academy of Sciences **106**, 6916 (2009).

[61] O. Penrose and L. Onsager, Phys. Rev. **104**, 576 (1956).

[62] C. J. Pethick and H. Smith *Bose-Einstein Condensation in Dilute Gases*, 2st, ed. (Cambridge University Press, Cambridge, 2008).

[63] L. P. Pitaevskii and S. Stringari, *Bose-Einstein Condensation*, 1st, ed. (Oxford University Press, Oxford, 2003).

[64] L. P. Pitaevskii, Zh. Eksp. Teor. Fiz. **40**, 646 (1961).

[65] E. P. Gross, Nuovo Cimento **20**, 454 (1961); J. Math. Phys. **4**, 195 (1963).

[66] S. Stringari, Phys. Rev. Lett. **77**, 2360 (1996).

[67] D. S. Jin, J. R. Ensher, M. R. Matthews, C. E. Wieman, and E. A. Cornell, Phys. Rev. Lett. **77**, 420 (1996).

[68] M.-O. Mewes, M. R. Andrews, N. J. van Druten, D. M. Kurn, D. S. Durfee, C. G. Townsend, and W. Ketterle, Phys. Rev. Lett. **77**, 988 (1996).

[69] M. Edwards, P. A. Ruprecht, K. Burnett, R. J. Dodd, and C. W. Clark, Phys. Rev. Lett. **77**, 1671 (1996).

[70] Y. Castin and R. Dum, Phys. Rev. Lett. **77**, 5316 (1996).

[71] V. M. Pérez-García, H. Michinel, J. I. Cirac, M. Lewenstein, and P. Zoller, Phys. Rev. Lett. **77**, 5320 (1996).

[72] W. Zwerger, Journal of Optics B: Quantum and Semiclassical Optics **5**, S9 (2003).

[73] S. Sachdev, *Quantum Phase Transitions* (Cambridge University Press, Cambridge, 2006).

[74] J. Mun, P. Medley, G. K. Campbell, L. G. Marcassa, D. E. Pritchard, and W. Ketterle. PRL **99**, 150604 (2007).

[75] E. Altman, A. Polkovnikov, E. Demler, B. I. Halperin, and M. D. Lukin, Phys. Rev. Lett. **95**, 020402 (2005).

[76] D. S. Rokhsar and B. G. Kotliar, Phys. Rev. B **44**, 10328 (1991).

[77] T. Matsubara and H. Matsuda, Prog. Theor. Phys. **16**, 569 (1956).

[78] C. Bruder, R. Fazio, and G. Schon, Phys. Rev. B **47**, 342 (1993).

[79] E. Altman and A. Auerbach, Phys. Rev. Lett. **89**, 250404 (2002).

[80] M. R. Matthews, D. S. Hall, D. S. Jin, J. R. Ensher, C. E. Wieman, E. A. Cornell, F. Dalfovo, C. Minniti, and S. Stringari, Phys. Rev. Lett. **81**, 243 (1998).

[81] F. Gerbier, Phys. Rev. Lett. **99**, 120405 (2007).

[82] C. J. Pethick and H. T. C. Stoof, Phys. Rev. A **64**, 013618 (2001).

[83] D.-S. Luhmann, K. Bongs, K. Sengstock, and D. Pfannkuche, Phys. Rev. A **77**, 023620 (2008).

[84] S. Konabe, T. Nikuni, and M. Nakamura, Phys. Rev. A **73**, 033621 (2006).

[85] G. Pupillo, C. J. Williams, and N. V. Prokof'ev, Phys. Rev. A **73**, 013408 (2006).

[86] F. Gerbier, A. Widera, S. Folling, O. Mandel, T. Gericke, and I. Bloch, Phys. Rev. Lett. **95**, 050404 (2005).

[87] F. Gerbier, A. Widera, S. Folling, O. Mandel, T. Gericke, and I. Bloch, Phys. Rev. A **72**, 053606 (2005).

[88] R. Roth and K. Burnett, Phys. Rev. A **67**, 031602(R) (2003).

[89] G.-D. Lin, W. Zhang, and L.-M. Duan, Phys. Rev. A **77**, 043626 (2008).

[90] E. Toth, A. M. Rey, and P. B. Blakie, Phys. Rev. A **78**, 013627 (2008).

[91] C. Lannert, T.-C. Wei, and S. Vishveshwara, Phys. Rev. A **75**, 013611 (2007).

[92] A. M. Clogston, Phys. Rev. Lett. **9**, 266 (1962).

[93] B. S. Chandrasekhar, Appl. Phys. Lett. **1**, 7 (1962).

[94] P. Fulde and R.A. Ferrell, Phys. Rev. **135**, A550 (1964).

[95] A. I. Larkin and Yu.N. Ovchinnikov, Zh. Eksp. Teor. Fiz **47**, 1136 (1964).

[96] C. Chin, R. Grimm, P. Julienne, and E. Tiesinga, Rev. Mod. Phys. **82**, 1225 (2010).

[97] S. Giorgini, L.P. Pitaevskii, and S. Stringari, Rev. Mod. Phys. **80**, 1215 (2008).

[98] D. E. Sheehy and L. Radzihovsky, Phys. Rev. Lett. **96**, 060401 (2006).

[99] D. E. Sheehy and L. Radzihovsky, Ann. of Phys. **322**, 1790 (2007).

[100] L. Radzihovsky and D. E. Sheehy, Rep. Prog. Phys. **73**, 076501 (2010).

[101] M. W. Zwierlein, A. Schirotzek, C. H. Schunck, and W. Ketterle, Science **311**, 492 (2006).

[102] G. B. Partridge, W. Li, R. I. Kamar, Y.-A. Liao, and R. G. Hulet, Science **311**, 503 (2006).

[103] Y. Shin, M. W. Zwierlein, C. H. Schunck, A. Schirotzek, and W. Ketterle, Phys. Rev. Lett. **97**, 030401 (2006).

[104] G. B. Partridge, W. Li, Y. A. Liao, and R. G. Hulet, Phys. Rev. Lett. **97**, 190407 (2006).

[105] T. Mizushima, K. Machida, and M. Ichioka, Phys. Rev. Lett. **94**, 060404 (2005).

[106] J. Kinnunen, L.M. Jensen, and P. Törmä, Phys. Rev. Lett. **96**, 110403 (2006).

[107] N. Yoshida and S.-K. Yip, Phys. Rev. A **75**, 063601 (2007).

[108] K. Yang, Phys. Rev. B **63**, 140511(R) (2001).

[109] G. Orso, Phys. Rev. Lett. **98**, 070402 (2007).

[110] H. Hu, X.-J. Liu, and P.D. Drummond, Phys. Rev. Lett. **98**, 070403 (2007).

[111] A.E. Feiguin and F. Heidrich-Meisner, Phys. Rev. B **76**, 220508(R) (2007).

[112] X. W. Guan, M. T. Batchelor, C. Lee, and M. Bortz, Phys. Rev. B **76**, 085120 (2007).

[113] X.-J. Liu, H. Hu, and P. D. Drummond, Phys. Rev. A **76**, 043605 (2007).

[114] G. G. Batrouni, M. H. Huntley, V. G. Rousseau, and R. T. Scalettar, Phys. Rev. Lett. **100**, 116405 (2008).

[115] M. Casula, D. M. Ceperley, and E. J. Mueller, Phys. Rev. A **78**, 033607 (2008).

[116] E. Zhao and W. V. Liu, Phys. Rev. A **78**, 063605 (2008).

[117] P. Kakashvili and C. J. Bolech, Phys. Rev. A **79**, 041603(R) (2009).

[118] H. Moritz, T. Stöferle, K. Günter, M. Köhl, and T. Esslinger, Phys. Rev. Lett. **94**, 210401 (2005).

[119] Y. Liao, A. S. C. Rittner, T. Paprotta, W. Li, G. B. Partrige, R. G. Hulet, S. K. Baur, and E. J. Mueller, preprint arXiv:0912.0092 (2009).

[120] J. Catani, G. Barontini, G. Lamporesi, F. Rabatti, G. Thalhammer, F. Minardi, S. Stringari, and M. Inguscio, Phys. Rev. Lett. **103**, 140401 (2009);

[121] D. M. Weld, P. Medley, H. Miyake, D. Hucul, D. E. Pritchard, and W. Ketterle, Phys. Rev. Lett. **103**, 245301 (2009).

[122] D. McKay and B. DeMarco, New J. Phys. **12**, 055013 (2010).

[123] G. Breit and I. I. Rabi, Phys. Rev. **38**, 2082 (1931).

[124] M. Olshanii, Phys. Rev. Lett. **81**, 938 (1998).

[125] P. G. De Gennes, *Superconductivity of Metals and Alloys* (Addison-Wesley, Reading, MA, 1989).

[126] R. A. Riedel, L.-F. Chang, and P. F. Bagwell, Phys. Rev. B **54**, 16082 (1996).

[127] C. A. Regal, M. Greiner, and D. S. Jin, Phys. Rev. Lett. **92**, 040403 (2004).

[128] E. Altman and A. Vishwanath, Phys. Rev. Lett. **95**, 110404 (2005).

[129] G. E. Blonder, M. Tinkham, and T. M. Klapwijk, Phys. Rev. B **25**, 4515 (1982).

[130] A.F. Andreev, Zh. Eksp. Teor. Fiz. **46**, 1823 (1964)[Sov. Phys. JETP **19**, 1228 (1964); **49**, 655 (1966) [**22**, 455 (1966)].

[131] A. Furusaki and M. Tsukada, Phys. Rev. B **43**, 10164 (1991).

[132] A. Furusaki, H. Takayanagi, and M. Tsukada, Phys. Rev. B **45**, 10563 (1992).

[133] P. F. Bagwell, Phys. Rev. B **46**, 12573 (1992).

[134] R. A. Riedel and P. F. Bagwell, Phys. Rev. B **48**, 15198 (1993).

[135] P. F. Bagwell, Phys. Rev. B **49**, 6841 (1994).

[136] M. Hurd, S. Datta, and P. F. Bagwell, Phys. Rev. B **54**, 6557 (1996).

[137] R. A. Riedel, L.-F. Chang, and P. F. Bagwell, Phys. Rev. B **54**, 16082 (1996).

[138] J. M. Byers and M. E. Flatté, Phys. Rev. Lett. **74**, 306(1995).

[139] G. Deutscher and D. Feinberg, Appl. Phys. Lett. **76**, 487 (2000).

[140] P. Recher, E. V. Sukhorukov, and D. Loss, Phys. Rev. B **63**, 165314 (2001).

[141] D. Beckmann, H. B. Weber, and H. v. LLohneysen, Phys. Rev. Lett. **93**, 197003 (2004).

[142] S. Russo, M. Kroug, T. M. Klapwijk, and A. F. Morpurgo, Phys. Rev. Lett. 95, 027002 (2005).

[143] A. Kleine, A. Baumgartner, J. Trbovic, and C. Schnenberger, Europhys. Lett. **87**, 27011 (2009).

[144] P. S. Luo, T. Crozes, B. Gilles, S. Rajauria, B. Pannetier, and H. Courtois, Phys. Rev. B **79**, 140508(R) (2009).

[145] M. C. O'Hara, Ph.D. thesis, U. of Illinois at Urbana-Champaign (2010); M. C. O'Hara and D. J. Van Harlingen, *Cooper Pair Splitting in Double Ferromagnet-Superconductor Junctions*, in preparation.

[146] W. Belzig, A. Brataas, Y. V. Nazarov, and G. E. W. Bauer, Phys. Rev. B **62**, 9726 (2000).

[147] M. Fogelström, Phys. Rev. B **62**, 11812 (2000).

[148] Y. S. Barash and I. V. Bobkova, Phys. Rev. B **65**, 144502 (2002).

[149] A. Cottet and W. Belzig, Phys. Rev. B **72**, 180503(R) (2005).

[150] B. Kastening, D. K. Morr, L. Alff, and K. Bennemann, Phys. Rev. B **79**, 144508 (2009).

[151] J. N. Kupferschmidt and P. W. Brouwer, preprint arXiv:1009.3163 (2010).

[152] T. Yamashita, S. Takahashi, and S. Meakawa, Phys. Rev. B **68**, 174504 (2003).

Author's Biography

Kuei Sun was born on January 22, 1979 in Pingtong, Taiwan. He started his study as a physics major at National Taiwan University in 1997. After having received B.S. in physics in 2001, he took the compulsory military service until 2003. He pursued graduate study in 2004 in Department of Physics at University of Illinois at Urbana-Champaign and became a member of Professor Smitha Vishveshwara's research group in 2005.